



# Kent Academic Repository

**Dorrington, Hal (2019) *Full-field Swept Source Optical Coherence Tomography using a compact probe head*. Master of Science by Research (MScRes) thesis, University of Kent,.**

## Downloaded from

<https://kar.kent.ac.uk/83351/> The University of Kent's Academic Repository KAR

## The version of record is available from

## This document version

UNSPECIFIED

## DOI for this version

## Licence for this version

CC BY (Attribution)

## Additional information

## Versions of research works

### Versions of Record

If this version is the version of record, it is the same as the published version available on the publisher's web site. Cite as the published version.

### Author Accepted Manuscripts

If this document is identified as the Author Accepted Manuscript it is the version after peer review but before type setting, copy editing or publisher branding. Cite as Surname, Initial. (Year) 'Title of article'. To be published in *Title of Journal*, Volume and issue numbers [peer-reviewed accepted version]. Available at: DOI or URL (Accessed: date).

## Enquiries

If you have questions about this document contact [ResearchSupport@kent.ac.uk](mailto:ResearchSupport@kent.ac.uk). Please include the URL of the record in KAR. If you believe that your, or a third party's rights have been compromised through this document please see our [Take Down policy](https://www.kent.ac.uk/guides/kar-the-kent-academic-repository#policies) (available from <https://www.kent.ac.uk/guides/kar-the-kent-academic-repository#policies>).

# University of Kent

## **Full-field Swept Source Optical Coherence Tomography using a compact probe head.**

by Hal Dorrington

*In Fulfillment of the Requirements for the Degree of Masters of Science, MSc  
Supervised by Professor Adrian Podoleanu*

**School of Physical Sciences**  
Applied Optics Group  
*September 2019*



## Abstract

The presented thesis is an exploration of compact imaging devices, which operate using the method of Full Field Swept Source Optical Coherence Tomography, (FF-SS-OCT). Particularly, the potential for a Compact probe head, (CPH), to be used as a remote imaging device is explored, which could have many potential applications, such as in endoscopy and in optical biopsy.

A novel design for an off-axis interferometer has been developed, which is encased within the presented CPH to form one part of the FF-SS-OCT system. The other part of the system is referred to as the operations part, which is grouped together with the CPH to form the complete system. This is referred to as the bulk version and has been constructed and analysed. A capability of the bulk system of imaging a quasi-specular 5p coin has been demonstrated and A-scan, B-Scan and Fixed wavelength (FW) images are presented.

In theory, the CPH could be separated from the operations part by a Coherent Fibre Bundle, (CFB), transforming the CPH into a remote imaging device. This is then referred to as the bundle version of the system. However, attempts at demonstrating the bundle version experimentally were unsuccessful. Reasons for this failure are suggested and some ideas for future work are presented.

In terms of the bulk version, a variation and general broadening of axial resolution versus Optical Path Difference, (OPD), was measured, which Master-Slave (MS) processing was found to reduce. The axial resolutions of Fast Fourier Transform, (FFT), and MS processing methods at  $OPD = 0$  respectively were found to be;  $lc_{FFT} = 15.29\mu m$  and  $lc_{MS} = 15.20\mu m$ , however, the axial resolutions of the two methods were found to diverge from each other with greater OPD, with MS processing securing a better axial resolution throughout the entire axial range.

The Signal-to-Noise Ratio, (SNR), of the system, at a scanning speed of 1  $Hz$ , was

found to be 30.015  $dB$ , much lower than that of commercial grade FF-SS-OCT systems. The low SNR was a consequence of the dimensions of the probe, which meant only a tiny fraction,  $< 0.3\%$ , of backscattered light from a scattering object placed in front of the probe was collected and relayed to the detector. Furthermore, the common path design of the interferometer meant that it was impossible to perform a balanced detection, which would have otherwise significantly improved SNR.

A set of experiments were conducted to analyse the SNR vs OPD, performance of the system at different values of number of spectral frames,  $M$ . In the first set of experiments the  $fps$  rate of the camera was varied to increase  $M$  and in the second set  $\Delta T$  was varied to increase  $M$ . In both sets of results a non linear proportionality between SNR performance and  $M$  was obtained, when the expected result was a linear proportionality. The SNR as a function of exposure time,  $\tau$ , was also obtained, which demonstrated a general increase in SNR with larger  $\tau$  as expected.

## **Acknowledgements**

I am very thankful to Prof. Adrian Podoleanu and Dr. Michael Hughes for their supervision and expert advice, and most of all for their inspiration. I am also very grateful to Dr. Manuel Marques, who has a contagious enthusiasm for the subject and who has always been willing to help.

### **Disclaimer**

I acknowledge Dr. Adrian Bradu as the author of the Master Slave processing Lab-View code, and do not claim to have had any part in writing it.

## TABLE OF CONTENTS

<b>List of Figures</b> . . . . .	xiii
<b>List of Tables</b> . . . . .	xvi
<b>List of Acronyms</b> . . . . .	xvii
<b>Chapter 1: Introduction</b> . . . . .	1
1.1 Imaging tissue with OCT . . . . .	1
1.1.1 Optical Biopsy with FF-OCT . . . . .	2
1.2 Principles of OCT . . . . .	5
1.2.1 Interferometry . . . . .	6
1.2.2 Axial ranging . . . . .	11
1.2.3 Sensitivity . . . . .	11
1.2.4 Axial resolution . . . . .	12
<b>Chapter 2: Fundamentals of the FF-SS-OCT system</b> . . . . .	14
2.1 Swept Source A-Scan . . . . .	14
2.1.1 Overview . . . . .	14
2.1.2 Broadband Sampling . . . . .	15
2.1.3 Source Sweeping . . . . .	17

2.1.4	Interference current . . . . .	20
2.1.5	Detector sampling . . . . .	21
2.1.6	Fourier Transform Processing . . . . .	22
2.1.7	Master-Slave Processing . . . . .	27
2.2	A-scan Characteristics . . . . .	29
2.2.1	Signal to Noise Ratio . . . . .	29
2.2.2	Depth dependent sensitivity . . . . .	32
2.3	FF-SS-OCT . . . . .	33
2.3.1	Overview . . . . .	33
2.3.2	Data acquisition . . . . .	35
2.3.3	Lateral resolution . . . . .	36
2.3.4	Features . . . . .	37
2.3.5	Fixed wavelength . . . . .	38
 <b>Chapter 3: The Potential use of the CFB for remote FF-SS-OCT probe heads</b>		<b>39</b>
3.1	Background . . . . .	39
3.1.1	Single fibre OCT systems for optical biopsy . . . . .	39
3.1.2	Motivation for CFB OCT systems . . . . .	41
3.2	Coherent Fibre Bundle . . . . .	42
3.2.1	Lateral Scanning versus Full-field . . . . .	43
3.2.2	Features . . . . .	45
3.3	OCT . . . . .	45
3.3.1	Common path design . . . . .	46



3.3.2	Multimoding . . . . .	47
3.3.3	Cross-coupling . . . . .	48
3.3.4	FF-OCT . . . . .	49
3.4	FF-SS-OCT . . . . .	50
3.4.1	Justification for SS-OCT . . . . .	50
3.4.2	Effects of the CFB . . . . .	50
3.4.3	Advancements in miniaturization . . . . .	51
<b>Chapter 4: Proposed System Design and Technical details . . . . .</b>		<b>52</b>
4.1	Probe head overview . . . . .	52
4.1.1	Optical path of Launching fibres . . . . .	54
4.1.2	Lens configuration . . . . .	57
4.1.3	Specifications . . . . .	59
4.1.4	Divergence of beams . . . . .	60
4.2	Off-axis Interferometer Design . . . . .	61
4.2.1	Lateral OPL matching . . . . .	62
4.2.2	Off axis interference . . . . .	64
4.2.3	Limited FOV . . . . .	65
4.3	System Operation . . . . .	68
4.3.1	Bulk and Bundle versions . . . . .	68
4.3.2	Swept-Source Block . . . . .	70
4.3.3	Detection and Processing Block . . . . .	73
4.3.4	Processing method . . . . .	76

<b>Chapter 5: Results</b>	78
5.1 Axial resolution	78
5.1.1 FWHM versus OPD	79
5.2 SNR	81
5.2.1 Sensitivity	81
5.3 Sensitivity versus OPD	84
5.3.1 CMOS Shutter Speed, <i>fps</i>	84
5.3.2 Sweeping Speed, $\Delta T$	93
5.3.3 Discussion	96
5.3.4 SNR versus $\tau$	97
5.3.5 Summary	99
5.4 5p Coin Images	100
5.4.1 Fixed wavelength	100
5.4.2 A-scan	102
5.4.3 B-scan	104
<b>Chapter 6: Conclusion and Future Work</b>	107
6.1 Summary	107
6.2 Future Research and Development	109
6.2.1 CFB Incorporation	109
6.2.2 Miniaturization	109
6.2.3 D.C. removal by off-axis incidence of reference arm	111
6.2.4 Mirror Terms	113

**References . . . . . 117**

## LIST OF FIGURES

1.1	Schematic Michelson Interferometer OCT system. BS: Beam Splitter, $r_R z_R$ : Reference Mirror, $r_O z_O$ : Single Object Reflector. . . . .	7
1.2	Graphical illustration of the two components of $i_D(k, z)$ . Red: $i_{D.C.}(k)$ , Gold: $i_{A.C.}(k, z)$ . . . . .	10
1.3	Graphical Illustration of $i_D(k, z)$ . . . . .	10
2.1	An example object reflectivity profile, $r_O(z_O)$ , (2.1) . . . . .	15
2.2	Graphical representation of $S(k)$ (red), and the filtered $S_{\delta k}(k)$ (blue), at three different spectral points, $k_0, k_1$ and $k_2$ . . . . .	16
2.3	Schematic function of an <i>AOTF</i> . . . . .	18
2.4	Schematic Michelson interferometer SS-OCT system. SS: Swept Source. RM: Reference Mirror, BS: Beam Splitter, O: Object, D: Detector. . . . .	19
2.5	Illustration of the real space FT for a single object reflector of reflectivity $R_m$ and axial position $z_m$ , with signal (red) and $lc_{\Delta k}$ (gold). . . . .	23
2.6	Illustration of an A-Scan, $A(z)$ , for an object with $M = 4$ reflectors, with signal (red) and $lc_{\Delta k}$ (gold). . . . .	24
2.7	Acquisition of Masks, $\mathbf{Q}$ , using a Full-field Swept Source OCT system. Swept Source (SS), Reference Mirror (RM) CMOS Camera (CMOS). . . . .	27
2.8	Schematic FF-SS-OCT system with Michelson Interferometer. SS: Swept Source, BS: Beam Splitter, O: Object, RM: Reference Mirror, CMOS camera. . . . .	34
2.9	Volume acquisition of a FF-SS-OCT system. A series of spectral frames, $k(x, y)_n$ , are obtained in depth, $z$ . . . . .	35

3.1	Example schematic fibre based OCT system. LCS: Low Coherence Source, PhD: Photo-detector, DC: Directional Coupler, O: Object, RM: Reference Mirror, CG: Coherence Gate. . . . .	39
3.2	Illustration of an end face of a CFB. . . . .	42
3.3	CFB incorporated into a forward facing line scanning probe. LCS: Low Coherence Source, BS: Beam Splitter, SM: Galvanometer Scanning Mirror. $L_0$ : Objective lens, LS: laterally scanning, CMOS camera. . . . .	44
3.4	CFB incorporated into a forward facing Full-field probe. LCS: Low Coherence Source, BS: Beam Splitter, $L_0$ : Objective lens, CMOS camera. . . . .	44
4.1	Illustration of the operation of the Compact probe head. $L_O$ : Objective lens, $L_I$ : Imaging lens, OI: Object Interval/Coherence Gate, IP: Imaging/Interference Plane, Red line: Object launching fibre, Brown line: Reference launching fibre, Blue line: Coherent Fibre Bundle, (CFB). . . . .	52
4.2	Optical path of launching fibres. SS: Swept Source, FB: Feeding fibre, DC: Directional Coupler, TS: Translation Stage, C: Collimator, FS: Free Space Section, OA: Optical Attenuator, FL: Focusing Lens, PC: Polarisation Controller, CPH: Compact Probe Head. . . . .	54
4.3	Diagram of ray traces through the probes telescope. OP: Object plane, IP: Imaging Plane, $L_O$ and $L_I$ : Object and Imaging Lens of equal focal, $f$ . . . . .	57
4.4	Illustration of chromatic aberration through a single lens. . . . .	58
4.5	Illustration of Beam Divergence from an optical fibre. . . . .	60
4.6	Optical path of Object and reference beams through the interferometer. OLF: Object Launching Fibre, RLF: Reference Launching fibre, O: Object, IP: Interference Plane, $\theta_i$ : Launching Fibre inclination, (a,b,c): Extremity ray traces of divergent beams, (P1,P2,P3): Vertical points of IP. . . . .	61
4.7	FOV from a SM800 single fibre at distance $d$ , for constant $\lambda = 850nm$ . Blue: Experimental, Red: Theoretical. . . . .	65
4.8	Operation and probe parts schematic. FG: Function Generator, AOTF: Acousto-optic tuneable filter, SLD: Superluminescent diode, DC: Directional coupler, CPH: Compact probe head, OUI: Object under investigation, CFB: Coherent Fibre Bundle, CMOS camera, DAQ: Digital Acquisition Device, CPU: Computer Processing Unit. . . . .	69

5.1	Axial resolution dependence on OPD of FFT (red) and MS (blue) processing methods, and ideal (gold). . . . .	79
5.2	Signal amplitude roll off with OPD for $fps = 2000s^{-1}$ , $M = 1000$ . Red dashed: Experimental, Red solid: Theoretical. . . . .	86
5.3	Signal amplitude roll off with OPD for $fps = 2500s^{-1}$ , $M = 1250$ . . . . .	88
5.4	Normalised Signal Amplitude versus OPD. . . . .	90
5.5	SNR versus OPD. . . . .	92
5.6	SNR versus OPD for $\Delta T = 0.25 s$ , $M = 500$ , with interpolant (solid red), and linear (dashed orange) fits. . . . .	94
5.7	SNR versus OPD for $\Delta T = 0.5s$ , $M = 800$ , with interpolant (solid red), and linear (dashed orange) fits. . . . .	95
5.8	SNR as a function of exposure time $\tau$ at $OPD = 1mm$ . Obtained with two sweeping periods, $\Delta T = 0.5s$ and $\Delta T = 1s$ . . . . .	98
5.9	FW image of surface of a 5p coin. . . . .	100
5.10	Another FW image of surface of 5p coin. . . . .	101
5.11	A-scans taken from the 5p coin at two different lateral co-ordinates; (100,101) and (109,132). . . . .	102
5.12	Demonstration of the ROI selection for a B-scan. . . . .	104
5.13	B-scan of the ROI from Fig 5.13. Amplitude of each pixel (White-Blue-Black) is plotted as a function of lateral co-ordinate (x-axis) and spectral component/depth (y axis) . . . . .	105
6.1	Illustration of the divergence from a conventional flat faced fibre (top) and ball end shaped fibre (bottom) . . . . .	110
6.2	Illustration of mirror terms. Top: No overlap of object through $OPD_0$ , therefore no mirror terms in FT. Bottom: Overlap of object through $OPD_0$ , therefore mirror terms in FT . . . . .	113

## LIST OF TABLES

4.1	$L_O$ and $L_I$ lens specifications. . . . .	59
4.2	SM800 fibre specifications. . . . .	59
4.3	Schott Leached imaging Bundle dimensions. . . . .	68
4.4	Performance features of the BroadSweeper-840 . . . . .	72
4.5	Performance features of the Mikrotron EoSens CL Full . . . . .	73
4.6	Set of combined values of Active area and $fps$ achieved by the Mikrotron EoSens CL Full . . . . .	74
5.1	Bandwidths for different $fps$ and $M$ values . . . . .	84
5.2	Theoretical axial range for different values of $M$ . . . . .	84
5.3	$\Delta T$ - Depth sensitivity experiment acquisition parameters. . . . .	93
5.4	$\Delta T$ and $fps$ values and corresponding permissible $\tau$ ranges. . . . .	97

## LIST OF FIGURES



## LIST OF ACRONYMS

<b>FF-SS-OCT</b> - Full-field Swept Source OCT	<b>CMOS</b> - Complementary metal-oxide-semiconductor
<b>CPH</b> - Compact probe head	<b>DC</b> - Directional Controller
<b>FW</b> - Fixed wavelength	<b>GRIN</b> - Gradient Index Lens
<b>CFB</b> - Coherent Fibre Bundle	<b>CG</b> - Coherence Gate
<b>OPD</b> - Optical Path Difference	<b>MEMS</b> - Micro-Electro-Mechanical Systems
<b>MS</b> - Master Slave	<b>SD-OCT</b> - Spectral Domain OCT
<b>FFT</b> - Fast Fourier Transform	<b>IP</b> - Imaging/Interference Plane
<b>SNR</b> - Signal-to-Noise ratio	<b>OI</b> - Objective Interval
<b>OCT</b> - Optical Coherence Tomography	<b>OLF</b> - Object launching fibre
<b>NA</b> - Numerical Aperture	<b>RLF</b> - Reference launching fibre
<b>FD-OCT</b> - Fourier Domain OCT	<b>PC</b> - Polarisation Controller
<b>SS-OCT</b> - Swept Source OCT	<b>OA</b> - Optical Attenuator
<b>FF-OCT</b> - Full-field OCT	<b>NIR</b> - Near-Infrared region
<b>OPL</b> - Optical Path Length	<b>SM800</b> - Single Mode fibre (800nm)
<b>LCR</b> - Low Coherence Reflectometry	<b>FG</b> - Function Generator
<b>PS-OCT</b> - Point Scanning OCT	<b>CCD</b> - Charge-coupled device
<b>LS-OCT</b> - Line Scanning OCT	<b>TTL</b> - Transistor-transistor logic
<b>FOV</b> - Field of View	<b>CPU</b> - Computer Processing Unit
<b>FT</b> - Fourier Transform	<b>DAQ</b> - Digital Acquisition Device
<b>FWHM</b> - Full Width Half Maximum	<b>LabVIEW</b> - Laboratory Virtual Instrument Engineering Workbench
<b>SLD</b> - Superluminescent Diode	<b>ROI</b> - Region of Interest
<b>AOTF</b> - Acousto-Optic Tuneable Filter	<b>RMS</b> - Root mean square
<b>TD-OCT</b> - Time Domain OCT	

## Introduction

### 1.1 Imaging tissue with OCT

For imaging tissue, we would like to acquire high resolution sub surface images, without causing harm or disturbance to the tissue. Imaging methods involving ionizing radiation penetrate through the entire body, though offer poor spatial resolution and come with the cost of delivering harmful radiation. Optical imaging modalities exhibit the opposite features, providing no more than  $mm$ 's of depth penetration, yet producing images at much greater spatial resolution, whilst also being non invasive, meaning no harm is caused to the tissue.

Optical Coherence Tomography, (OCT), is a modern optical imaging modality capable of obtaining images of  $\mu m$  order resolution at up to  $2mm - 3mm$ 's in depth, using the principle of interferometry. It is unique amongst other optical imaging modalities in that the axial resolution is determined by the coherence length of the light source, and not by the Numerical aperture (NA) of the systems lenses.

A significant development for imaging tissue has been the invention of Fourier Domain-OCT (FD-OCT), which is capable of imaging structures at a significantly enhanced Signal-to-Noise Ratio (SNR), enabling finer layers of tissue to be resolved. FD-OCT is widely applied in ophthalmology, where it is used to image the many fine layers of the foveola of the retina. Speed is also an important parameter for *in vivo* imaging, as a system must be fast enough to avoid generating motion artefacts. Swept Source OCT, (SS-OCT), is a particular method of FD-OCT that provides extremely fast acquisition speeds, in the order of hundreds of  $kHz$ , [1].

### 1.1.1 *Optical Biopsy with FF-OCT*

Optical Biopsy is the name given to the minimally invasive process of using light to probe tissue *in vivo*, as opposed to conventional biopsy in which the tissue is physically excised. This is executed by passing a miniaturised probe through either an orifice or a surgical opening of a patient. Surgical techniques employing endoscopy, such as laparoscopic surgery, have become an integrated part of medical procedures, [5].

Conventionally, endoscopic OCT is conducted using single fibre systems, which employ a method of mechanical scanning to laterally translate a beam emitted from a single fibre across an object. Such probes are non passive and complicated in design, requiring a component to perform lateral scanning.

An attractive probe for optical biopsy would be completely passive, simple in its design and fast in its operation. An obvious method of meeting these demands is to remove the process of lateral scanning, which requires employing a Full-field OCT, (FF-OCT), scheme. However, this is not possible using a single fibre system, as only a negligible region of the object backscattered light can be collected by a single fibre.

### *CFB for FF-SS-OCT*

A probe head employing an FF-OCT scheme could potentially be realised with the use of a Coherent Fibre Bundle (CFB), enabling a Full-field probe head to be separated from the bulk parts of a system. The CFB is essentially a thin flexible imaging conduit formed from a bundle of single fibres, with each single fibre representing a single pixel.

There are a few reports of FF-OCT being conducted through CFB's, the first with a tuneable swept source coming in 2009 from Helen D. Ford and Ralph P Tatam, [2]. In almost all cases a 'common path' interferometer had been reported, which has been necessary for conserving the degree of coherence between the two arms of the interferometer, and consequently in preserving SNR. There are few exceptions to the design, [3].

In a common path interferometer, both object and reference arms share the same path Optical Path Length, (OPL), through a solitary CFB. Reported systems have typically either encompassed a forward facing Fizeau based interferometer at the probe end the CFB, [4, 5], or a side viewing Michelson like interferometer [2, 6], both of which have their limitations.

In the Fizeau based interferometer the Optical Path Difference, (OPD), of the interferometer is necessarily dependent on the position of the probe relative to the object, which limits its functionality. Furthermore, to the best of my knowledge, there are no reports of forward facing Fizeau interferometers operating with a tuneable swept source. The Michelson like interferometer, though reported with tuneable swept sources, has the limitation of requiring a larger volume probe head, as an entire Michelson interferometer, including perpendicular arms, a central beam splitter and a reference mirror, must all be contained within the probe head.

### *Proposed Solution*

The proposed probe encompasses a common-path off-axis Fizeau-like interferometer, which facilitates the oblique projection of object and reference arms onto the input face of a CFB, where they interfere and generate an interference signal.

An attractive feature of the presented probe design is its compactness. This comes from the design of the interferometer, which is not limited in its compactness by the configuration of its optical arms. Instead, the minimum size of the probe is only limited by the properties of the lenses and the optical fibres used within the interferometer. Theoretically, the proposed probe could be reduced in size until it is not appreciatively different in its cross-sectional area to that of a CFB, presenting the potential for a minimally invasive system well suited for optical biopsy.

## 1.2 Principles of OCT

### *Overview*

OCT is essentially an application of optical homodyne detection, using interference of two beams from the same source to generate volumes of an object, in real time and with highly discriminating resolution in depth. It is typically used for non invasive *in vivo* imaging of biological tissue, though is not limited to biomedical applications, and is useful for any scenario in which high resolution and non invasive depth sectioning of an object is desired. One such example is in art conservation, [7].

OCT can also be considered as the tomographic extension of Low Coherence Reflectometry, (LCR), extending the functionality of LCR from depth profiling into volume imaging. LCR creates depth profiles of an object, referred to as Amplitude scans, (A-Scans), which are essentially 1-Dimensional graphs representing the reflectivity profile of the object along the axial scanning direction. A number of A-scans can be collected along a lateral line to generate a cross-section through the object, referred to as a B-scan, while collecting A-Scans across a lateral plane generates a volume.

There are two possible volume acquisition schemes in OCT, those involving lateral scanning, such as Point-Scanning OCT, (PS-OCT), and Line Scanning OCT, (LS-OCT), and those without, such as Full-field OCT, (FF-OCT). In PS-OCT a convergent beam is scanned laterally across a Field of View, (FOV), of an object, and a set of parallel A-scans are obtained sequentially. The A-scans are then rapidly stitched together in post processing to generate a volume. In FF-OCT a wide-field beam is projected over a constant object FOV, and there is a simultaneous acquisition of parallel A-scans using a 2-Dimensional detector.

### 1.2.1 Interferometry

We assume the simplest case; a system employing a bulk Michelson free space interferometer, in which a beam splitter is used to derive two beams from the same broadband source. The two beams, the *reference beam* and the *object beam*, are guided through free space by a microscopy interface and are reflected from a reference mirror and an object under investigation respectively. They are then superimposed and relayed to the systems detector, where the electric field of the superimposed beam is detected as an irradiance and converted into an electrical current. When there is interference of the two beams, the detected electrical current,  $i_D$ , is not equal to the sum of currents detected by the two beams individually.

A schematic of an OCT system employing a bulk Michelson free space interferometer is given in *Fig. 1.1*, in which the reflectivity and axial position of the reference mirror and single object reflector respectively are given by  $r_R z_R$  and  $r_O z_O$ .

To find an expression for the detected current we first consider a monochromatic source, emitting light travelling in one direction,  $z$ , which for the purpose of OCT is the axial direction along the depth profile of the object. The plane wave equation used to express the electric field emitted from the source can then be given as,

$$\vec{E}_S = E_S(k, \omega) \cdot e^{i[kz - \omega t]}. \quad (1.1)$$

$E_S(k, \omega)$  is the electric field amplitude of the light emitted from the source, which is dependent on its waveumber,  $k$ , and its angular temporal frequency,  $\omega$ . The wavenumber is the spatial frequency of the light and is related to the spatial periodicity, else known as the wavelength or colour,  $\lambda$ , by,  $k = 2\pi/\lambda$ . The phase of the electric field at axial position,  $z$ , and at time,  $t$  is given by  $[kz - \omega t]$ .

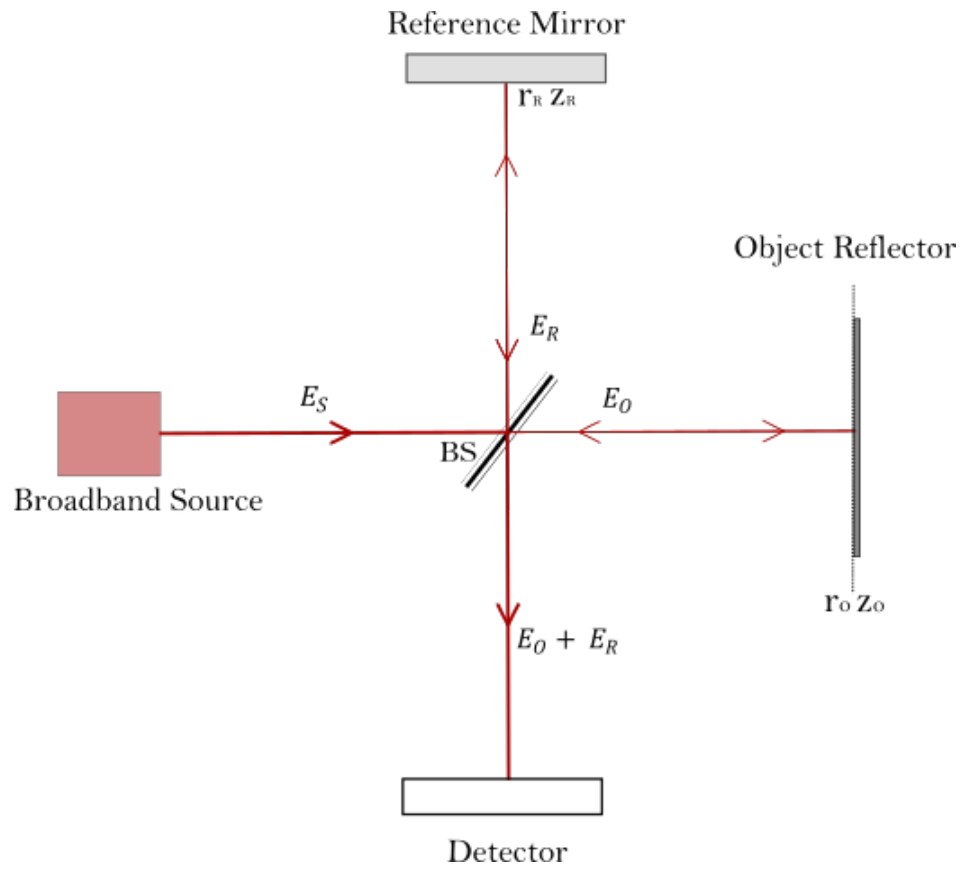


Figure 1.1: Schematic Michelson Interferometer OCT system. BS: Beam Splitter,  $r_R z_R$ : Reference Mirror,  $r_O z_O$ : Single Object Reflector.



If we first consider an object that is a single reflector, and assume that the beam splitter is achromatic and with a lossless 50/50 splitting ratio, then the electric fields returning from the object and the reference mirror respectively are, [8];

$$\vec{E}_O = \frac{1}{\sqrt{2}} \cdot E_S(k, \omega) \cdot r_O \cdot \exp(i[2kz_O - \omega t]), \quad (1.2)$$

$$\vec{E}_R = \frac{1}{\sqrt{2}} \cdot E_S(k, \omega) \cdot r_R \cdot \exp(i[2kz_R - \omega t])$$

In (1.2),  $r_O$  and  $r_R$  are the reflectivities of the object reflector and the reference reflector respectively, and  $z_O$  and  $z_R$  their axial positions relative to the beam splitter at the origin of the interferometer.

The irradiance of the superimposed electric field is given by

$$I = \frac{1}{2} \left\langle (E_O + E_R) \cdot ((E_O + E_R)^*) \right\rangle_{\tau}, \quad (1.3)$$

where  $(E_O + E_R)^*$  is the complex conjugate of the superimposed beam, and  $\langle \rangle_{\tau}$  denotes time averaging over an integration time,  $\tau$ . If we consider an array of pixels as the detector, then the integration time is the duration of exposure onto the pixels. Considering only one pixel, the induced photocurrent,  $i_D$ , is the product of the pixel responsivity,  $\rho$ , with the detected irradiance,  $I$ . Using (1.3) we obtain,

$$i_D(k, z) = \frac{\rho}{4} \cdot \langle E_S(k)^2 \rangle_{\tau} \cdot [r_O^2 + r_R^2 + 2 \cdot r_O r_R \cdot \cos(2k(z_O - z_R))] \quad (1.4)$$

We can re-write (1.4) in terms of optical power, using the power spectrum of the source,  $S(k)$ , and the power reflectivity of the object and reference reflectors respectively,  $R_O$  and  $R_R$ . Here we have made the approximation that  $\sqrt{R} = r$ , which is valid for normal incidence. The power spectrum is related to the source electric field by  $S(k) = \langle |E_s(k)|^2 \rangle_\tau$ , [8]. The detected current in terms of optical power is then,

$$i_D(k, z) = \frac{\rho}{4} S(k) \cdot [R_O + R_R + 2 \cdot \sqrt{R_O} \sqrt{R_R} \cdot \cos(2k(\Delta z))]. \quad (1.5)$$

The oscillating sinusoidal term is the phase dependent interference signal, an alternating current,  $i_{A.C.}$ , which modulates the phase independent direct current,  $i_{D.C.}$ . The axial displacement between the object reflector and the reference mirror is given by  $\Delta z = z_O - z_R$ . It is seen from (1.5) how  $k$  and  $\Delta z$  both affect the periodicity of the interference signal.

The monochromatic source can be replaced with a broadband source and (1.5) will remain true. Graphical illustrations of the two distinct photocurrents are shown in *Fig. 1.2* and *Fig. 1.3*, in which  $S(k)$  is a broadband source emitting a Gaussian shaped power spectrum. Shown is an  $i_{A.C.}$  received from a single object reflector positioned at some displacement  $\Delta z$ , where  $0 < 2\Delta z < l_c$ , such that  $i_{A.C.}$  has many peaks.

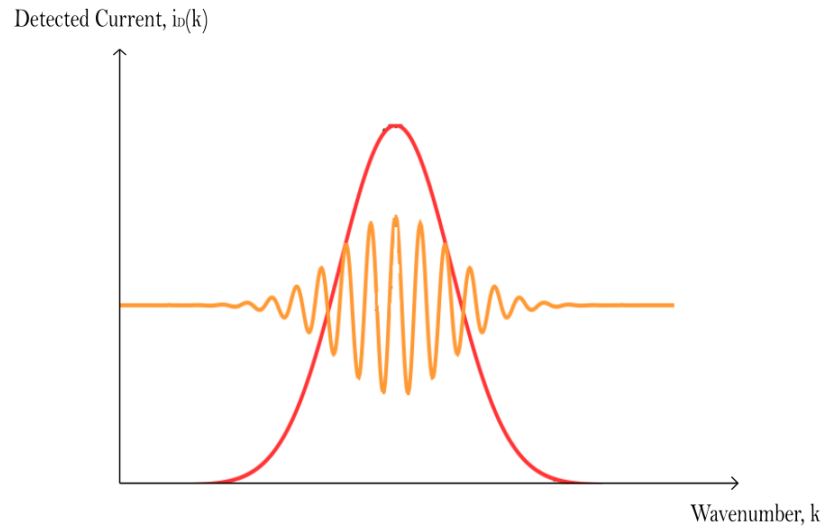


Figure 1.2: Graphical illustration of the two components of  $i_D(k, z)$ . Red:  $i_{D.C.}(k)$ , Gold:  $i_{A.C.}(k, z)$ .

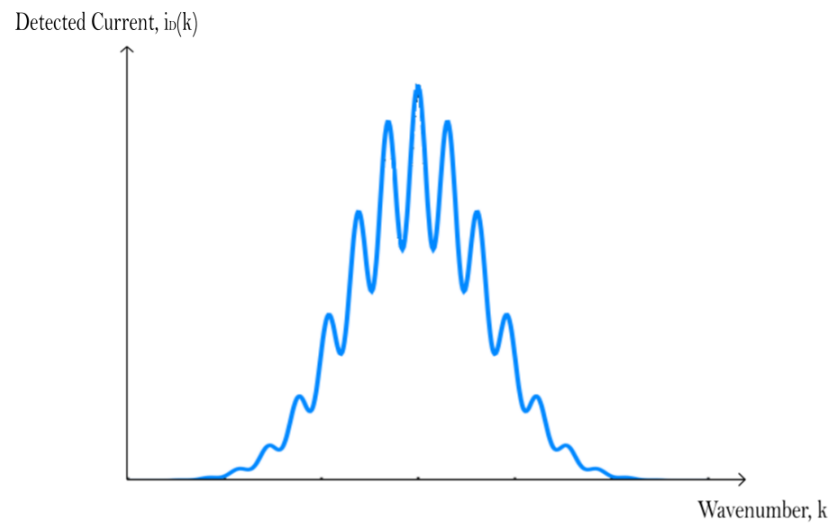


Figure 1.3: Graphical Illustration of  $i_D(k, z)$ .

### 1.2.2 Axial ranging

From (1.5) we see that the periodicity of the interference signal is given by  $2k(\Delta z)$ , and hence, the axial position of the object reflector at any given moment can be determined from the periodicity of the modulated power spectrum.

The relationship between the modulation periodicity, object reflector OPD and wavenumber is the basis of depth ranging in OCT. This is discussed further in Chapter 2 using the specific method of SS-OCT.

### 1.2.3 Sensitivity

The sensitivity of an OCT system,  $R_{min}$  is the minimum reflectivity that can be detected, and is given by the inverse of SNR, [9],

$$R_{min} = \frac{1}{SNR} \quad (1.6)$$

We see from (1.5) that the amplitude of the interference signal is determined by the product  $\sqrt{R_O}\sqrt{R_R}$ , which is a result of optical homodyne detection.  $\sqrt{R_O}$  is attenuated with depth, due to the high possibility of scattering and absorption of optical light in tissue, whereas there is no loss in  $\sqrt{R_R}$ , as it passes through no scattering media.

Hence, the signal amplitude and hence SNR and sensitivity is greater for OCT than for conventional optical imaging modalities, such as reflectance microscopy, in which the signal strength is solely dependent on  $\sqrt{R_O}$ .

### 1.2.4 Axial resolution

The degree of correlation in phase between the two arms of the interferometer is given by the coherence function,  $\gamma = \gamma(\Delta k, z)$ , which is the Fourier Transform (FT) pair of  $S(k)$ , and is valued between  $0 \leq 1$

The magnitude of  $\gamma$  is determined by the displacement of the arms from  $\Delta z = 0$ , with  $\gamma$  having a maximum at  $\Delta z = 0$ , and decreasing in magnitude with  $\Delta z > 0$ . The coherence length,  $l_c$ , is the  $\Delta z$  at which  $\gamma$  is half its maximum amplitude, i.e. the Full-Width Half Maximum, (FWHM).

$$\gamma(\Delta k, l_c)_{FWHM} = l_c \quad (1.7)$$

Considering that  $\gamma$  is the Fourier Transform pair of  $S(k)$ , the axial spread of the two functions are inversely related. The light emitted from a broadband source is in the form of a Bessel beam, which has a power spectrum given by a Bessel function of the first kind. This can be approximated by a Gaussian function, which is given in (1.8) its normalized form, [8], where  $k_0$  is the central wavenumber of the spectrum and  $\Delta k$  is the spectrum's bandwidth,

$$S(k) = \frac{1}{\Delta k \sqrt{\pi}} \cdot e^{-\left[\frac{k - k_0}{\Delta k}\right]^2} \quad (1.8)$$

From (1.8) we see that the spectral bandwidth of  $S(k)$  is equal to the standard deviation  $S(k)$ . The coherence function is obtained from taking an FT, which gives, [8],

$$\gamma(\Delta k, z) = e^{-(z)^2 \Delta k^2} \quad (1.9)$$

The FWHM of (1.9), and therefore the axial resolution of OCT, in air, is then,

$$\gamma(\Delta k, z)_{FWHM} = l_c = \frac{2\sqrt{\ln(2)}}{\Delta k} \quad (1.10)$$

For measurements of any real object the coherence length must be divided by the refractive index of the object to obtain the correct axial resolution. Written in terms of optical bandwidth,  $\Delta\lambda$ , and central wavelength,  $\lambda_0$ , the  $l_c$  in air is;

$$l_c = \frac{4\ln(2)}{\pi} \cdot \frac{\lambda_0^2}{\Delta\lambda} \quad (1.11)$$

We require a source that emits light over as broad a bandwidth as possible to obtain the best axial resolution. Typical broadband sources used in OCT are capable of emitting light with an optical bandwidth of tens to hundreds of  $\mu m$  in order. An example, [10], is an optical source of 150  $nm$  bandwidth, operating at a central wavelength of 890  $nm$ , which corresponds to a coherence length and hence axial resolution of approximately 3 $\mu m$ .

## CHAPTER 2

# Fundamentals of the FF-SS-OCT system

## 2.1 Swept Source A-Scan

### 2.1.1 Overview

We now consider a case in which the object under investigation is a real object with many reflecting layers, each of the many fine layers of the object representing an optical boundary with a given reflectivity. For an object with  $N$  reflecting boundaries, the object reflectivity profile,  $r_O(z_O)$ , is given by the sum of object reflectivities. Each reflecting boundary is described as a Dirac delta function,  $\delta[z - z_n]$ , at a given axial depth,  $z_n$ , and with a magnitude given by its reflectivity,  $r_n$ .

$$r_O(z_O) = \sum_{n=1}^N r_n \delta[z - z_n] \quad (2.1)$$

A graph of an example reflectivity profile is given in *Fig 2.1*.

When the interferometry procedure outlined in Chapter 1 is repeated using a multilayered object in the object arm, a superposition of interference terms are detected, with modulations of greater frequency representing interference signals obtained from deeper layers of the object. The detected interference current for a multilayered object is given in (2.2), where  $OPD_n = 2(z_n - z_0)$ , is the OPD of the  $n$ 'th layer of the object.

$$i_D(k, z) = S(k) \cdot \sum_{n=1}^N 2\sqrt{R_R R_n} \cos(k \cdot OPD_n), \quad (2.2)$$

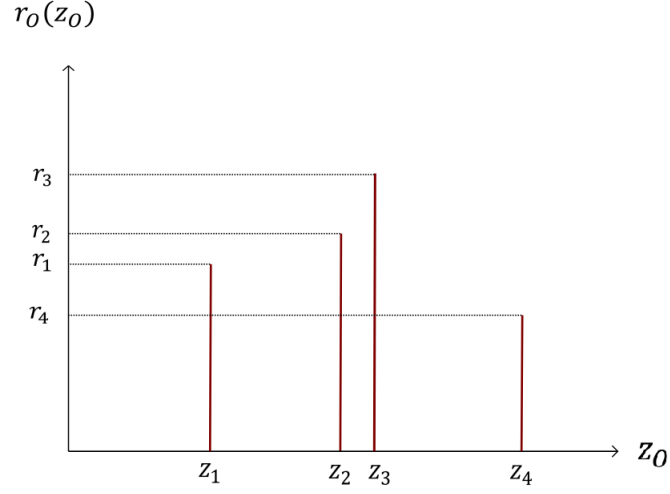


Figure 2.1: An example object reflectivity profile,  $r_O(z_O)$ , (2.1)

In SS-OCT the depth dependent modulations of (2.2) are resolved from each other in time. This is achieved using a 'Swept Source' which, in a given sweeping time, 'sweeps' over a broadband power spectrum. A detector is exposed to the detected photocurrent at regularly spaced intervals of time, sequentially capturing depth resolved spectral points.

### 2.1.2 Broadband Sampling

A broadband Gaussian power spectrum,  $S(k)$ , is sampled at the source into a series of linewidth spectral channels,  $S_{\delta k}(k)$ , using a Gaussian shaped filter of spectral bandwidth  $\delta k$ . An illustration of  $S(k)$  and  $S_{\delta k}(k)$  are given in Fig. 2.2

As  $S_{\delta k}(k)$  is another Gaussian shaped power spectrum, with spectral bandwidth  $\delta k$ , its expression can be obtained from (1.8), by replacing  $\Delta k$  with  $\delta k$ ,

$$S_{\delta k}(k) = \frac{1}{\delta k \sqrt{\pi}} \cdot e^{-\frac{k - k_0^2}{\delta k}} \quad (2.3)$$

Similarly, the corresponding linewidth coherence length  $l_{c_{\delta k}}$  is obtained from  $l_c$ ,



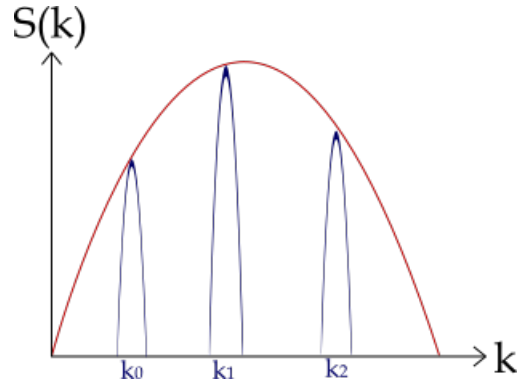


Figure 2.2: Graphical representation of  $S(k)$  (red), and the filtered  $S_{\delta k}(k)$  (blue), at three different spectral points,  $k_0$ ,  $k_1$  and  $k_2$ .

(1.10), by replacing  $\Delta k$  with  $\delta k$ ,

$$l_{C_{\delta k}} = \frac{2\sqrt{\ln(2)}}{\delta k}, \quad (2.4)$$

This is referred to as the instantaneous coherence length, which in terms of the optical bandwidth of the spectral channel,  $\delta\lambda$ , is given by,

$$l_{C_{\delta\lambda}} = \frac{4\ln(2)}{\pi} \cdot \frac{\lambda_0^2}{\delta\lambda}. \quad (2.5)$$

### 2.1.3 Source Sweeping

To obtain the spectral components from within  $l_{c\delta\lambda}$ , we must scan  $S_{\delta k}(k)$  across  $S(k)$ , by tuning  $k$ . The principle of tuning  $k$  to obtain the components of the interfering backscattered light is referred to as Swept Source Interferometry, and was first demonstrated by scientists at UCL in 1989, two years before OCT had been invented. In 1997, J. G. Fujimoto et. al, [11, 12], later demonstrated the application of spectral tuning to OCT.

An example of a source that can be used to generate  $S(k)$  is a Superluminescent Diode, (SLD), and an example of a tuneable filter that can be applied to  $S(k)$  to filter it into its constituent spectral channels is an Acoustical Optical Tuneable Filter, (AOTF).

An AOTF is formed from an Acousto-optic birefringent crystal, which is perturbed into a periodic fluctuation of refractive indices when applied with an acoustic wave, forming a phonon diffraction grating, [13]. A fraction of the power input into the AOTF is diffracted by the phonon grating and emitted into a spectral channel  $S_{\delta k}(k)$ , which has a narrow optical bandwidth,  $\delta\lambda$ , and a corresponding narrow spectral bandwidth,  $\delta k$ , related to each other by, [8],

$$\delta k = \frac{\pi}{\sqrt{\ln(2)}} \frac{\delta\lambda}{\lambda_0^2} \quad (2.6)$$

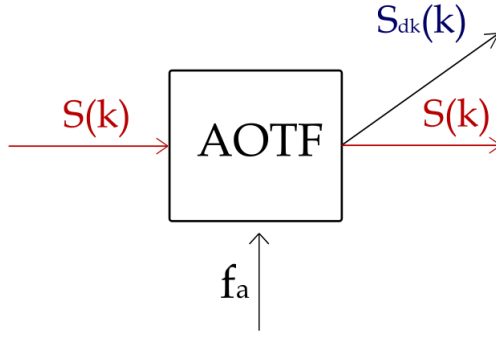


Figure 2.3: Schematic function of an *AOTF*.

Tuning can be achieved because the central wavelength of the diffracted beam,  $\lambda_0$ , is inversely proportional to the frequency of the applied acoustic wave,  $f_a$ . The relationship, [14], is given below, where  $v_a$  is the velocity of the acoustic wave and  $\Delta n$  is the birefringence of the Acousto-optic crystal. Spectral tuning is hence achieved by increasing  $f_a$  with respect to time.

$$\lambda_0 = \frac{v \cdot \Delta n}{f_a} \quad (2.7)$$

A negative consequence of broadband sampling is that optical power is lost from  $S(k)$  to  $S_{\delta k}(k)$ , the magnitude of loss being dependent on the reduction in bandwidth from  $\Delta k$  to  $\delta k$ , although some power is lost even if the entire bandwidth is passed through. For a filtering with no reduction in bandwidth, the loss in optical power is typically 3-4dB, [15].

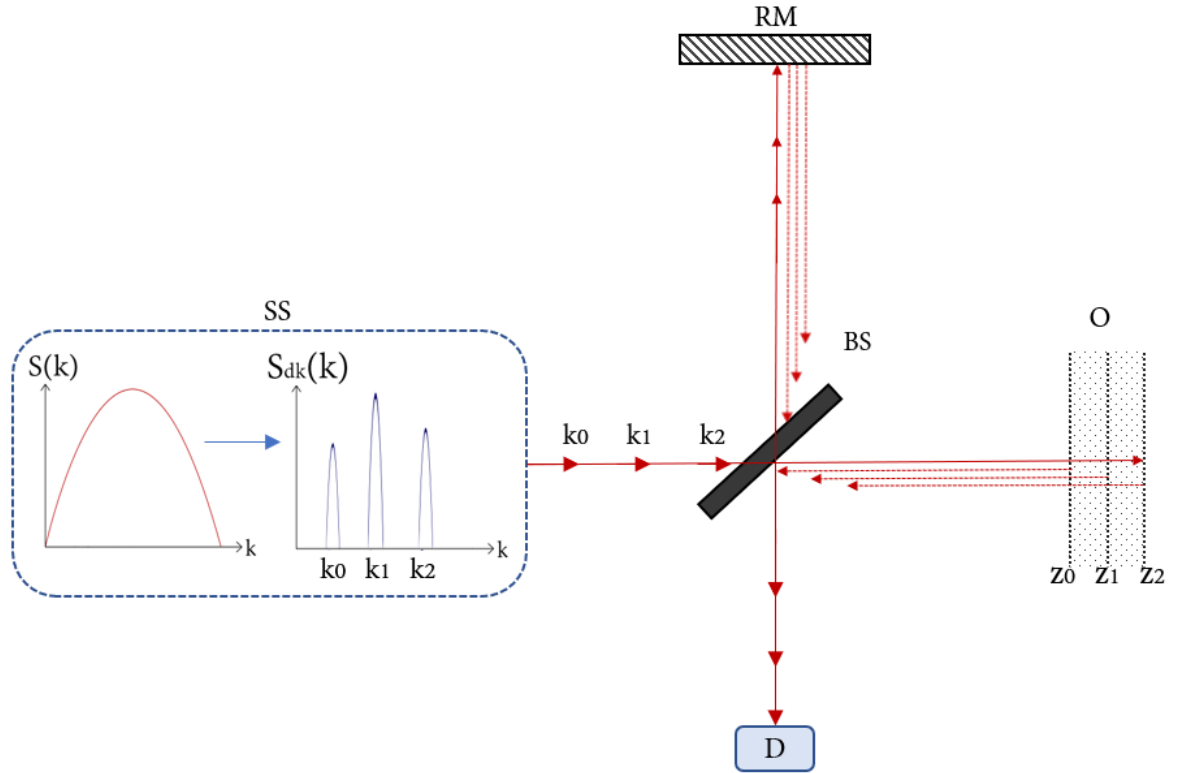


Figure 2.4: Schematic Michelson interferometer SS-OCT system. SS: Swept Source. RM: Reference Mirror, BS: Beam Splitter, O: Object, D: Detector.

An illustration of an SS-OCT system using a Michelson interferometer is given in Fig. 2.4. Three spectral channels,  $S_{dk}(k_0)$ ,  $S_{dk}(k_1)$  and  $S_{dk}(k_2)$ , with central wavenumber  $k_0$ ,  $k_1$  and  $k_2$  respectively, are sequentially emitted from a swept source and input into a Michelson free space interferometer. Interference of the backscattered light from the three separate beams occurs from the object layers at corresponding axial positions of  $z_0$ ,  $z_1$  and  $z_2$ .

### 2.1.4 Interference current

To find an expression for the interference current of SS-OCT we consider an initial wavenumber,  $k_i$ , which is swept over a spectral bandwidth,  $\Delta k$ , in a given sweeping time,  $\Delta T$ . Assuming a linear increase in wavenumber with respect to time,  $k(t)$  through a single sweep may be expressed as,

$$k(t) = k_i + \frac{\Delta k}{\Delta T} \cdot t \quad (2.8)$$

Substituting  $k(t)$  for  $k$  into (2.2) converts the detected photocurrent from a function of wavenumber and OPD into a function of time and OPD. Considering only the cosinusoidal component of the detected current,  $\cos(k, z)$ , we obtain

$$\cos(k, z) = \cos(t, z) = \cos\left(\frac{\Delta k}{\Delta T} t \cdot OPD\right). \quad (2.9)$$

The interference current detected at the output of the interferometer as a function of time is the instantaneous power spectrum, (2.3), modulated by (2.9). For an object with  $N$  reflecting layers this gives,

$$i_D(t, z) = \frac{\rho}{4} S_{\delta k}(k) \cdot \left[ \sum_{n=1}^N 2\sqrt{R_n R_R} \cdot \cos\left(\frac{\Delta k}{\Delta T} t \cdot \Delta z\right) \right] \quad (2.10)$$

We obtain an expression for the detected current by re-introducing the D.C. current into (2.10), giving,

$$i_D(t, z) = \frac{\rho}{4} S_{\delta k}(k) \cdot \sum_{n=1}^N \left[ R_n + R_R + 2\sqrt{R_n R_R} \cdot \cos\left(\frac{\Delta k}{\Delta T} t \cdot \Delta z\right) \right] \quad (2.11)$$

### *Auto-correlation current*

It should be noted that any interference signal will modulate the detected current. For a typical swept source the instantaneous coherence length is of  $cm$  order, and so any optics within either arm, introducing an OPD of  $cm$  order or less, will result in interference and further modulation of the detected current. This is referred to as the Auto-correlation current,  $i_{AC}$ .

If we consider the Auto-correlation current from the object arm alone, from  $p$  reflecting boundaries within the object, each at an axial distance of  $\Delta z_p = z_p - z_n$  from  $n$ 'th object reflecting boundaries, where  $\Delta z_p < lc_{\delta k}$ , then we can express  $i_{AC}$  as,

$$i_{AC}(t, z) = \frac{\rho}{4} S_{\delta k}(k) \cdot \left[ \sum_{n \neq p=1}^N \sqrt{R_n R_p} \cdot \cos \left[ \frac{\Delta k}{\Delta T} \cdot t \cdot (z_p - z_n) \right] \right] \quad (2.12)$$

#### *2.1.5 Detector sampling*

The time dependent detected current, (2.11), is sampled at a number of intervals in time, using a detector which is exposed to the superimposed beam at regular time intervals. This captures a series of spectral points. The maximum number of spectral points that can be sampled,  $M$ , is given by the ratio,

$$M = \frac{\Delta k}{\delta k} \quad (2.13)$$

Each exposure measures the intensity of the detected current at the  $m$ 'th point,  $i_{D,m}$ , and in one sweep a 1-Dimensional array of detected currents,  $\mathbf{M}$ , is formed,

$$\mathbf{M} = (i_{D,m}) = \sum_{m=1}^{M-1} i_{D,m} \quad (2.14)$$

### 2.1.6 Fourier Transform Processing

A method of processing  $\mathbf{M}$  is to take its discrete inverse FT, which maps the set of discrete values from the Fourier domain,  $i_{D,m}$ , into a set of discrete points,  $z_m$ , in real space. An array  $\mathbf{M}$  with  $M$  spectral points generates an A-scan array,  $\mathbf{A}$ , with  $\frac{M}{2}$  axial pixels.

$\mathbf{M}$  is processed into  $\mathbf{A}$  by a Fast Fourier Transform (FFT), [16], given by (2.15),

$$A_m(z_m) = \sum_{m=1}^{M-1} i_{D,m} \cdot e^{i \frac{k_m z_m}{M}} = \mathbf{A} \quad (2.15)$$

#### *Axial Resolution*

By taking an FFT of the discrete current, in time co-ordinates over a sweeping period,  $\Delta T$ , we are effectively taking an FFT in spectral co-ordinates, over a sweeping bandwidth,  $\Delta k$ . The coherence function is hence the FT pair of the tuning power spectrum,

$$\mathcal{F}^{-1}[S_{\Delta k}(k)] = \gamma(z)_{\Delta z} = e^{-(z)^2 \Delta k^2} \quad (2.16)$$

Which has a FWHM and hence axial resolution of

$$l_c = \frac{2\sqrt{\ln(2)}}{\Delta k} = \frac{4\ln(2)}{\pi} \cdot \frac{\lambda_0^2}{\Delta \lambda} \quad (2.17)$$

### Cross-correlation signal

The interference current representing the object reflectivity, (2.10), is referred to as the cross-correlation signal,  $A_{CC}$ . We find the FT of the cross-correlation using the convolution property on its two components,  $S_k(k)$  and  $\cos(k, z)$ ,

$$\mathcal{F}^{-1} \left[ \frac{\rho}{4} S_{\Delta k}(k) \right] \otimes \mathcal{F}^{-1} \left[ \sum_{n=1}^N 2\sqrt{R_n R_R} \cdot \cos\left(\frac{\Delta k}{\Delta T} t \cdot \Delta z\right) \right] \quad (2.18)$$

If we consider a single object reflector, with power reflectivity  $R_m$  at position  $z_m$ , then (2.18) is given by the convolution of given a tuning coherence function with a pair of Dirac delta functions.

$$\gamma(z)_{\Delta z} \otimes \sqrt{R_m R_R} \cdot \left( \delta[z + z_m] + \delta[z - z_m] \right) \quad (2.19)$$

An illustration of the cross-correlation signal and its conjugate pair, for a single object reflector with power reflectivity  $R_m$ , at positions  $z_m$  and  $-z_m$  respectively, is given in Fig. 2.5.

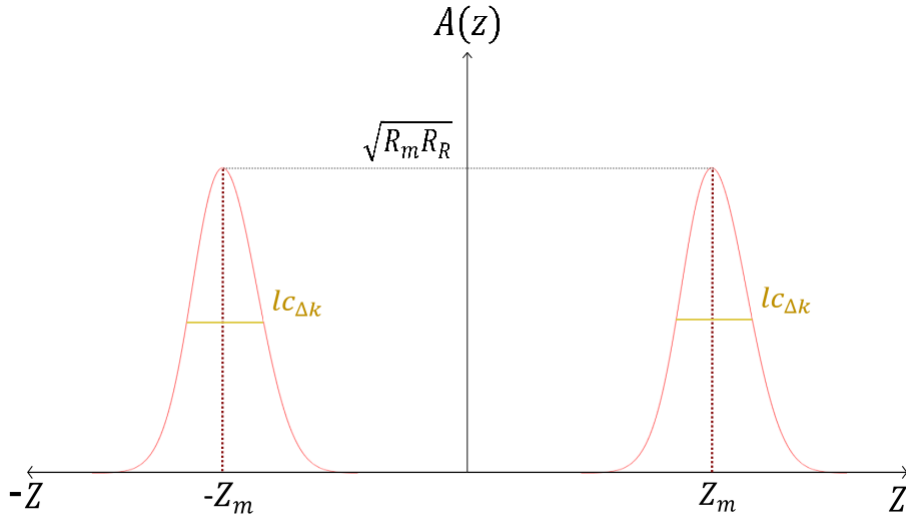


Figure 2.5: Illustration of the real space FT for a single object reflector of reflectivity  $R_m$  and axial position  $z_m$ , with signal (red) and  $l_{C_{\Delta k}}$  (gold).



Repeating the process for an object with  $M > 1$  reflecting boundaries, and ignoring the negative conjugate component we obtain,

$$A(z)_{CC} = \frac{\rho}{4} \cdot \sum_{m=0}^M \sqrt{R_m R_R} (\gamma_{\Delta k}[z - z_m]), \quad (2.20)$$

Notice the Dirac delta functions are now replaced with the tuning coherence function as a result of the convolution operation. An illustration of (2.20), for an object with  $M = 4$  axially separated object reflectors is given in Fig 2.6.

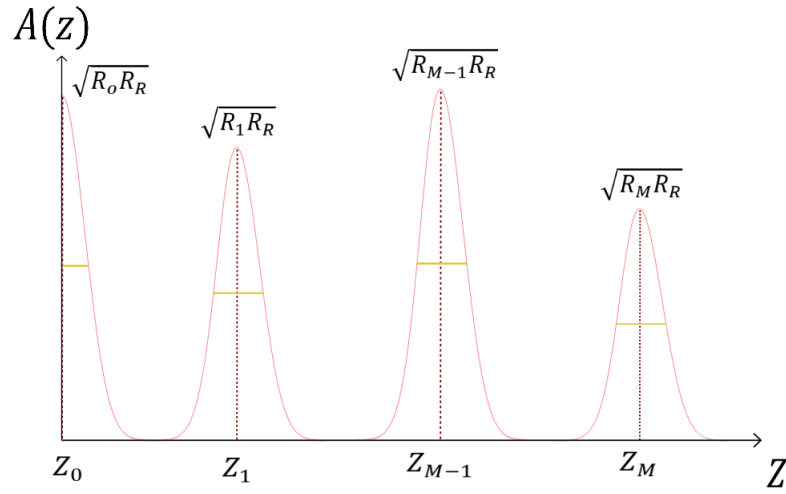


Figure 2.6: Illustration of an A-Scan,  $A(z)$ , for an object with  $M = 4$  reflectors, with signal (red) and  $l_{C_{\Delta k}}$  (gold).

### *The complete A-scan*

The D.C. and Auto-correlation signals may be similarly inferred to produce an expression for the complete A-Scan,

$$A(z) = A(z)_{DC} + A(z)_{CC} + A(z)_{AC} \quad (2.21)$$

$A(z)_{DC}$  is a Gaussian peak of shape given by the tuning coherence function, which is positioned at  $z = 0$ , and which has an amplitude proportional to the sum of reference and object power reflectivities.

$$A(z)_{D.C.} = \frac{\rho \cdot \gamma(z)_{\Delta k}}{8} \left[ R_R + \sum_n^N R_n \right] \quad (2.22)$$

$A(z)_{AC}$  is the Auto-correlation signal from the  $p$  reflecting boundaries, of either object or reference arm, which are not equal in position to the  $m$  axial positions of the cross-correlation signal.

$$A(z)_{AC} = \frac{\rho}{8} \cdot \sum_{p \neq m=0}^P \sqrt{R_p R_R} \left( \gamma_{\Delta k}[z - z_p] \right) \quad (2.23)$$

### *Non linearity*

We have assumed that  $k(t)$  is linear, though this is only an approximation and tunable sources will exhibit some divergence from linearity. This is because the source is tuned in terms of optical wavelength, and linear tuning in optical wavelength does not correspond to a linear tuning in wavenumber. Non linearity results in a non linear sampling of  $i_D(t, z)$ , causing a depth dependent variation and general broadening of axial resolution, [17].

Non linearity also results from dispersion introduced by the material of optical elements within the paths of light. Dispersion causes the OPD between the arms to vary with wavelength, causing a non linear dependence of  $k(t)$  on OPD.

One conventional solution to non linearity is to use a processing unit that will continuously re-calibrate the output of the swept source to make  $k(t)$  linear, [17]. However, this adds complexity to the system and so simpler solutions are preferable.

2.1.7 Master-Slave Processing

An attractive method of compensating for non linearity is to process the detected current using Master Slave processing, (MS). In this approach, the  $M$  channeled spectrum of the Fourier Transform method are referred to as slave spectra,  $S$ . The array of slave spectra,  $S$ , is identical to the array  $M$ , with both acquired in the exact same way, the difference between them only coming later in how they are processed to generate an A-scan.

Instead of taking a single FT over the entire set of slave spectrum, we instead take the cross-correlation of each member of  $S$  with each member of an array of Masks,  $Q$ , which are prerecorded channeled spectrum obtained from a reference mirror positioned in place of the object at a range of depth intervals.

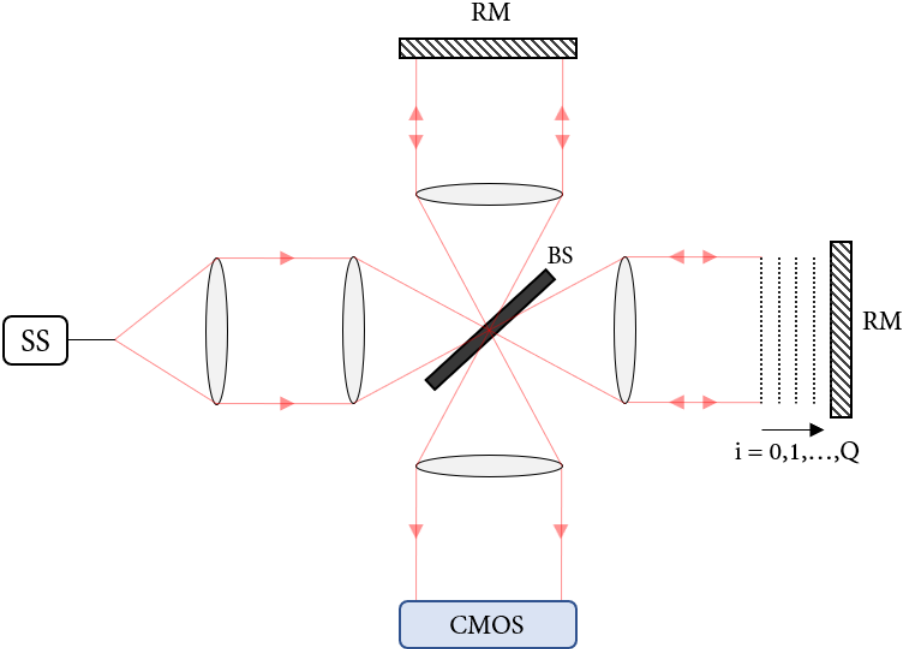


Figure 2.7: Acquisition of Masks,  $Q$ , using a Full-field Swept Source OCT system. Swept Source (SS), Reference Mirror (RM) CMOS Camera (CMOS).

The process of obtaining  $\mathbf{Q}$  using a FF-SS-OCT system is illustrated in Fig 2.7. A reference mirror is placed at a range of OPD positions,  $i = 0, 1, \dots$  etc., and the detected channeled spectrum at each OPD position is detected and saved as a mask.

$\mathbf{Q}$  and  $\mathbf{S}$  are given by (2.24), where the number of elements in each set,  $N$ , is equal and is given by the ratio  $N = \frac{\Delta k}{\delta k}$ .

$$S(i) = \sum_{i=1}^N M_i, \quad Q(i) = \sum_{i=1}^N Q_i \quad (2.24)$$

A cross-correlation of phase is taken between  $S(i)$  and  $Q(i)$  to obtain an MS A-scan,  $C(j)$ , [18], where  $j$  are the discrete axial positions of the A-scan.  $C(j)$  is computed, [19], by,

$$C(j) = (S * Q)[j] = \sum_{i=0}^{N-1} S(i)M(i + j) \quad (2.25)$$

## 2.2 A-scan Characteristics

### 2.2.1 Signal to Noise Ratio

An important performance metric for any imaging system is the SNR, which serves as a metric of image contrast, and is defined as the power ratio of the detected signal to the detected noise,

$$SNR = \frac{P_{Signal}}{P_{Noise}} = \frac{\langle i_D \rangle^2}{\sigma^2} \quad (2.26)$$

The SNR can be expressed in terms of the amplitude of the signal,  $A_{Signal}$ , and the amplitude of the noise,  $A_{Noise}$ , of the A-scan.

$$SNR = \left[ \frac{A_{Signal}}{A_{Noise}} \right]^2 \quad (2.27)$$

It is common practice to measure SNR on a logarithmic scale in units of  $dB$ , which is calculated from SNR by

$$SNR_{dB} = 20 \log_{10} \left[ \frac{A_{Signal}}{A_{Noise}} \right] \quad (2.28)$$

One of the characteristic features of SS-OCT is its ability, in principle, to achieve a far greater SNR than conventional Time Domain OCT (TD-OCT). This advantage was first shown mathematically by Mitsui in 1999, [20], and later verified experimentally by A. Izatt et. al. in 2003, [21].

### Signal

The signal is evaluated at  $OPD = 0$  to generate the largest possible SNR, considering the loss in signal amplitude at  $OPD > 0$ . If we consider a single object reflector at  $OPD = 0$ , then the cosinusoidal factor of the cross-correlation current is unity, and so the current is simplified to,

$$i_D(t, 0) = \frac{\rho}{2} \cdot S(k)_{\delta k} \cdot \sqrt{R_0 R_R} \quad (2.29)$$

We obtain the signal amplitude at  $z = 0$  by taking an FFT of  $i_D(t, 0)$ , using an exponent of  $z = 0$  in the FT to represent  $OPD = 0$ , giving,

$$A_{Signal}(0) = \frac{\rho}{2} \cdot S(k)_{\delta k} \cdot \sqrt{R_0 R_R} \cdot M \quad (2.30)$$

### Noise

Noise is dependent on the electrical bandwidth of the detector,  $B$ , which is determined by the lower frequency limit of analog-to-digital sampling,  $f_s$ . For  $M$  spectral points, sampled over a sweeping time,  $\Delta T$ , the sampling frequency,  $f_s$ , is given by  $f_s = \frac{2M}{\Delta T}$ . Substituting  $M = \frac{\Delta k}{\delta k}$  into  $f_s$ , we obtain,

$$f_s = \frac{2\Delta k}{\delta k} \frac{1}{\Delta T} \quad (2.31)$$

The electrical bandwidth is approximately double the sampling frequency, [22],

$$B = \frac{4\Delta k}{\delta k} \frac{1}{\Delta T} \quad (2.32)$$

If we assume shot noise limited detection, then the expression for the square of the detected noise,  $\sigma^2$ , can be given by (2.33), [8], where  $e$  is the fundamental electronic

charge.

$$\sigma^2 = e\rho \cdot S_{\delta k}(k_m) \cdot B \cdot R_R R_O \quad (2.33)$$

We take the FFT of (2.33) to obtain an expression for the A-scan noise amplitude,  $A(z)_{\sigma^2}$ , which generates,

$$A(z)_{\sigma^2} = \sigma^2 \quad (2.34)$$

The maximum obtainable SNR of a SS-OCT A-scan is then given by the ratio of the square of (2.30) to (2.34),

$$SNR_{Max} = \frac{\rho \cdot S_{\delta k}(k_m) \cdot M}{2eB} = \frac{\rho S_{\delta k}(k_m) \delta k \Delta T \cdot M}{4e\Delta k} \quad (2.35)$$

The theory suggests that  $SNR \propto M$ . Many factors are also seen to affect SNR, some of which present difficulties. Using a source with a larger tuning bandwidth to improve axial resolution, and increasing speed by reducing  $\Delta T$ , are both expected to reduce SNR.



### 2.2.2 Depth dependent sensitivity

The A-scan has a depth dependent sensitivity, determined by the instantaneous coherence function,  $\gamma(z)_{\delta z}$ . Intuitively, we understand that  $\gamma(z)_{\delta z}$  will attenuate the A-scan amplitude as OPD is increased from  $OPD = 0$ .

The effect of sampling  $S(k)$  with a filter of spectral bandwidth  $\delta k$  can be modelled by convolving the detected photocurrent with the window function of the sampling filter,  $W(k, \delta k)$ , [8],

$$W(k, \delta k) = \exp\left[-\frac{4\ln(2)k^2}{\delta k^2}\right] \quad (2.36)$$

From the convolution theorem,  $A(z)$  is multiplied by the FT of  $W(k, \delta k)$ , which is an exponential function referred to as a sensitivity roll-off function.  $A(z)$  is then given by,

$$A(z) = A(0) \cdot \exp\left[-\frac{z^2 \cdot \delta k^2}{4\ln(2)}\right] \quad (2.37)$$

The depth dependent sensitivity can be quantified by measuring the FWHM of the sensitivity function, i.e. the OPD at which  $A(z) = \frac{A(0)}{2}$ . On a logarithmic scale this is the OPD at which the signal is attenuated by  $6dB$ , and is given, [8], as,

$$OPD_{-6dB} = \frac{2\ln(2)}{\delta k} = \frac{2\ln(2)}{\pi} \frac{\lambda_0^2}{\delta \lambda} \quad (2.38)$$

## 2.3 FF-SS-OCT

### 2.3.1 Overview

One approach to producing volumes is to flood an object with a wide field beam of light and to collect multiple A-scans across a FOV using a 2-Dimensional detector. This is typically achieved using a digital camera with an active detection area, such as a Complementary metal-oxide-semiconductor, (CMOS), sensor. [23].

FF-OCT is typically facilitated using a microscopy interface, which projects collimated wide field beams onto an object and a reference mirror. An example schematic of an FF-SS-OCT system formed from a Michelson free space interferometer is shown in *Fig. 2.8*. Light from a Swept Source, (SS), is formed into two orthogonal wide-field beams, which are reflected off a Reference Mirror, (RM), and an Object, (O), respectively. The two reflected beams are superimposed at a central Beam Splitter (BS) and reflected towards a Full-field detector, which in the given example is a CMOS camera.

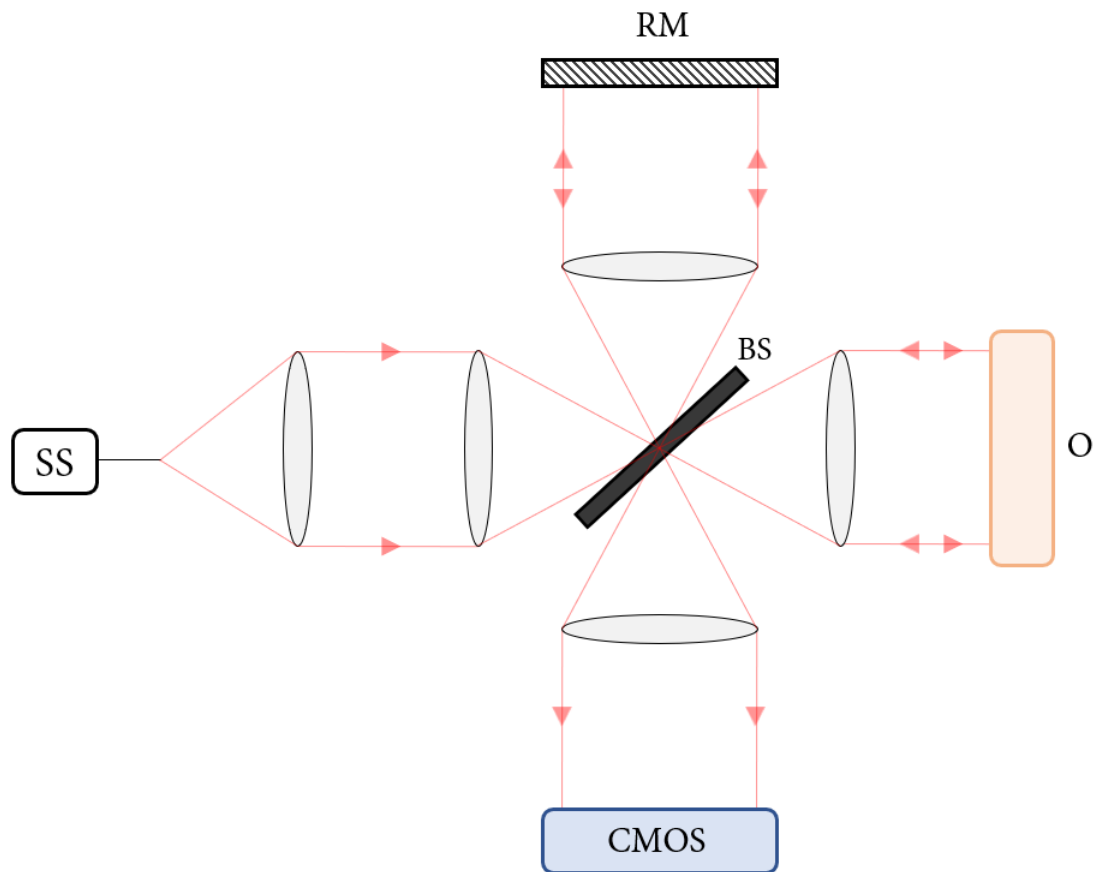


Figure 2.8: Schematic FF-SS-OCT system with Michelson Interferometer. SS: Swept Source, BS: Beam Splitter, O: Object, RM: Reference Mirror, CMOS camera.

### 2.3.2 Data acquisition

Using a Full-field scheme changes the  $M$  spectral points of the A-scan into  $M$  spectral frames, where the  $x$  and  $y$  co-ordinates of each spectral frame are determined by the active  $x$  and  $y$  pixel co-ordinates of the CMOS sensor array. In one spectral sweep of the source we therefore obtain an array  $\mathbf{M}$ , where.

$$\mathbf{M} = \left( \sum_{m=1}^{M-1} i_{D,m}(x), \sum_{m=1}^{M-1} i_{D,m}(y) \right) \quad (2.39)$$

The number of spectral frames is determined by the cameras frame repetition rate and the sweeping period of the source. If  $\Delta T$  is the sweeping period and  $f_{ps}$  the frequency of the detector in frames per second, then  $M$  is given by,

$$M = f_{ps} \cdot \Delta T \quad (2.40)$$

This determines that a B-scan or a volume will be formed from a number of  $\frac{M}{2}$  axial pixels. The  $x$ ,  $y$  and  $z$  co-ordinates of the spectral frames are illustrated in Fig. 2.9.

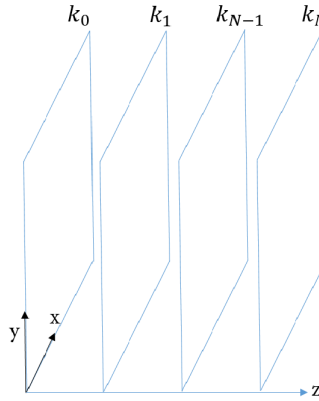


Figure 2.9: Volume acquisition of a FF-SS-OCT system. A series of spectral frames,  $k(x, y)_n$ , are obtained in depth,  $z$ .

### 2.3.3 Lateral resolution

The two determining factors on lateral resolution are the focusing capabilities of the objective lens and the pixel separation of the camera.

#### *Objective Lens*

The ideal lateral resolution of a lens can be determined by applying the Rayleigh criterion to the focused airy disc, which is given by (2.41), where  $f$  and  $D$  are the focal length and diameter of the objective lens respectively.

$$\Delta xy_{,Rayleigh} \approx 0.61 \cdot \frac{\lambda f}{D} \quad (2.41)$$

#### *Camera*

The resolution of the camera is determined from its pixel separation,  $\Delta d$ . If the object FOV is magnified, then  $\Delta d$  is divided by the magnification factor,  $M$ , to obtain a lateral resolution, (2.42).

$$\Delta xy_{,Camera} = \frac{\Delta d}{M} \quad (2.42)$$

#### 2.3.4 Features

##### *Speed*

There is no requirement for lateral scanning, meaning that the speed of volume acquisition is identical to the speed of A-scan acquisition.

##### *FOV*

The FOV may be manipulated in real time to control the lateral dimension of each image, by digitally controlling the active region of the CMOS sensor.

##### *Cross-Talk*

Using a highly spatially coherent source means that interference between laterally separated pixels may be detected, which are the result of interference from light emitted by scattering points along the lateral direction of the planes orthogonal to the direction of travel of the collimated wide field beams.

The modulations induced onto the detected current from Cross-talk are mistaken for objects at certain axial positions along the A-scan. There are methods by which the effects of Cross-talk can be removed, [24], though any such implementation into the proposed systems is left for future work.

### 2.3.5 *Fixed wavelength*

The FF-OCT system shown in *Fig. 2.7* offers a fixed wavelength (FW) mode of operation. In this mode the reference arm serves no function and a BS may be selected that transmits all of the incident light through to the object arm. The swept source is fixed in wavelength and light of a narrow optical linewidth is directed towards an object. Backscattered light collected from within the depth of focus interval of the objective lens is detected by the camera. Each pixel of the camera measures a value of intensity, from which a grayscale intensity image of the surface of the object is formed.

## The Potential use of the CFB for remote FF-SS-OCT probe heads

### 3.1 Background

#### 3.1.1 Single fibre OCT systems for optical biopsy

There are many single fibre commercial endoscopic OCT systems available, [25], which are designed having an object arm fibre isolated from the rest of the system, typically by housing the fibre within a catheter probe. This gives the object arm access to internal regions of the body, whilst the bulk parts of the system; the source, the detector, and the reference arm fibre, are all located outside the body. A schematic for an example fibre based OCT system is shown in *Fig. 3.1*, where the blue dashed line is shown to indicate the depth position inside the object selected by the coherence gate.

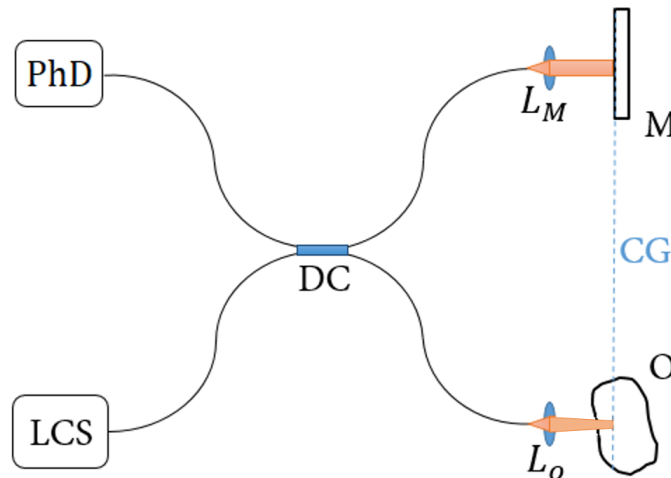


Figure 3.1: Example schematic fibre based OCT system. LCS: Low Coherence Source, PhD: Photo-detector, DC: Directional Coupler, O: Object, RM: Reference Mirror, CG: Coherence Gate.



In *Fig. 3.1*, broadband light is emitted from a low coherence source and injected directly into a single mode optical fibre, the feeding fibre, which feeds the injected light into a Directional Coupler, (DC). The DC replaces the beam splitter of the Michelson free space system, functioning to split the power incident from the feeding fibre into two fibres, the object and reference arm fibres.

An objective lens,  $L_O$  is used to converge the beam emitted from the end of the object arm fibre and to focus it into an axial line scan through the object.  $L_O$  is typically a miniaturized Gradient Index lens, (GRIN). These are cylindrical solid glass lenses with a gradient of refractive index along their lateral direction. They provide the same function as a conventional lens but with a much smaller diameter, allowing for narrow rod shaped probe heads of just a couple of *mm* in diameter to be made, [26]. The Coherence Gate, (CG), is scanned axially through the object along the focused line beam to form the A-scan. This can be achieved in the spectral domain, such as through spectral tuning as described in Chapter 2, or in the time domain, by translating the reference mirror. The schematic shown in *Fig. 3.1* is sufficient for attaining an A-scan. However, complexity must be added in order to laterally scan the convergent beam in conjunction with axial ranging to generate a volume.

#### *Methods of volume scanning*

Many approaches to volume scanning have been demonstrated in single fibre based systems, all of which require moving parts. One method is radial scanning, which is utilized by side viewing probes. These probes are pulled through some lumen of the body, such as the respiratory tracts, and light is scanned radially in a circumferential pattern by a rotating micro-prism at the end of the probe, [27]. Alternatively, there are forward facing probes, in which volumes are generated by raster scanning the convergent beam along the FOV of an object, [28].

Irrespective of the lateral scanning method, probe heads will typically require Micro-Electro-Mechanical Systems, (MEMS), to facilitate scanning. Probe designs incorporating MEMS require a driving power source and so in addition to requiring moving parts are also non-passive.

### 3.1.2 *Motivation for CFB OCT systems*

Having only a single depth scan through the object at any given time imposes limitations on the operation of single fibre OCT systems. Lateral scanning probes require precise alignment of components, [29], making them difficult to construct. Furthermore, lateral scanning schemes introduce another considering factor for the speed of volume acquisition, which must be considered for *in-vivo* applications.

If the single fibre of the object arm were replaced with a CFB, then an appreciable area of the object backscattered light could be collected in an instance, such that a FF-OCT scheme with a meaningful FOV could be employed. Multiple adjacent A-scans would be collected by the adjacent fibres of the CFB.

Of the various probe head types, the CFB could potentially be incorporated into the forward facing design, potentially making for a simple and passive OCT capable probe.

### 3.2 Coherent Fibre Bundle

The CFB is an imaging conduit that takes the shape of a thin and highly flexible cord. It is formed from an array of several thousand individual multimode fibres, which are each of  $\mu m$  scale diameter and are wound or leached together to produce a bundle. Thinner CFB varieties, such as the leached bundle, can have an external diameter within the range of  $0.45mm - 1.2mm$ , [30]. An illustration of an end face of a bundle is given in *Fig. 3.2*, which illustrates the close packing of adjacent fibres.

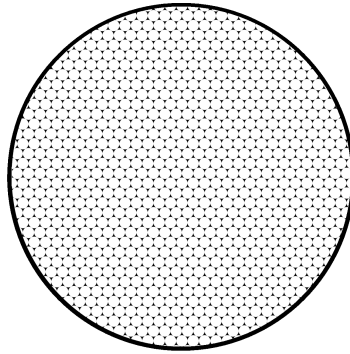


Figure 3.2: Illustration of an end face of a CFB.

The lateral configuration of fibres is fixed throughout the complete length of the bundle, meaning light projected onto one end is transmitted through the array of fibres, and a replicated but pixelated image output at the bundle's opposite end.

### 3.2.1 *Lateral Scanning versus Full-field*

There are two ways a CFB can be incorporated as an imaging conduit between the bulk parts and the of the probe end of an OCT system, which are with lateral scanning, such as in PS-OCT or with full field illumination, as in FF-OCT.

Within an PS-OCT system, each of the pixels are injected with light in turn, by scanning a focused beam along the bulk end of a CFB. An objective lens at the probe end of the CFB focuses the beam emitted from any single fibre at any given time onto a focused spot on the object. Injecting light into each fibre in turn at the bulk end results in laterally scanning the focused spot along the object. The backscattered light from the object is collected by the same objective lens and relayed back through the same CFB, after which a beam splitter is positioned to reflect the returning light towards the systems detector.

An example incorporating a CFB into a forward facing point scanning probe is shown in *Fig. 3.3*. Each CFB fibre is sequentially addressed by laterally scanning the object beam using a Galvanometer Scanning Mirror (SM). The object beam is focused onto the object with an Objective lens, ( $L_0$ ), and is then laterally scanned (LS) across the object.

In an FF-OCT system, the entire face of the CFB at the bulk end is illuminated in an instance, with light injected into all fibres at the same time. The lens at the bulk end of the CFB functions to collimate a divergent beam from a single fibre into a Full-field beam, which is then injected into the CFB. An objective lens at the opposite end of the CFB is used to form a conjugate imaging pair between the end face of the CFB and the FOV of the object under investigation. An example of a Full-field incorporation of a CFB is shown in *Fig. 3.4*,

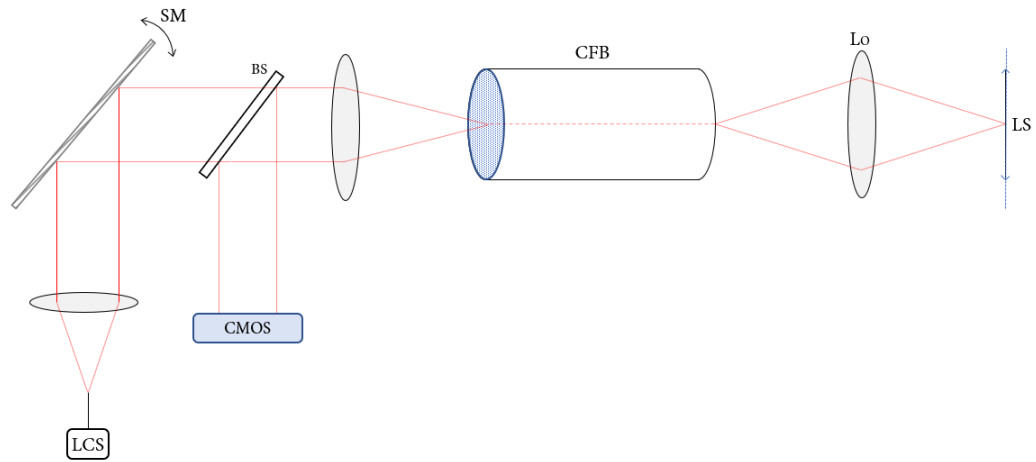


Figure 3.3: CFB incorporated into a forward facing line scanning probe. LCS: Low Coherence Source, BS: Beam Splitter, SM: Galvanometer Scanning Mirror.  $L_0$ : Objective lens, LS: laterally scanning, CMOS camera.

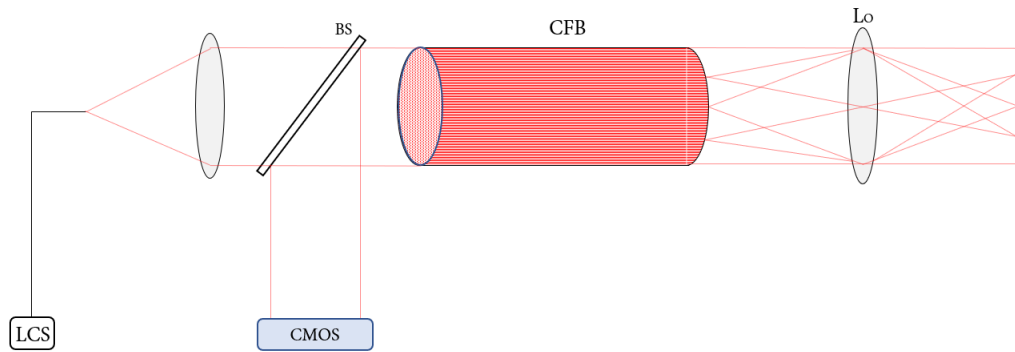


Figure 3.4: CFB incorporated into a forward facing Full-field probe. LCS: Low Coherence Source, BS: Beam Splitter,  $L_0$ : Objective lens, CMOS camera.

### 3.2.2 Features

#### *Pixelation effect*

An effect present in the images generated by both PS-OCT and FF-OCT uses of a CFB is the pixelation effect, which results from the bundles discrete arrangement of fibres. The spacing of the individual fibres sets limitations on the attainable lateral resolution,  $\Delta XY_{CFB}$ , which is given by the distance between the centre of adjacent fibres,  $\Delta d$ , and the magnification of the objective lens,  $M_{Objective}$ ,

$$\Delta XY_{CFB} = \frac{\Delta d}{M_{Objective}} \quad (3.1)$$

For applications in which an objective lens is not used,  $\Delta XY_{CFB}$  is simply given by the inter core spacing,  $\Delta d$ , provided the bundle is pressed sufficiently close to the object.

#### *Reflection power losses*

Another aspect to be considered is the loss of power due to the back reflections at the ends of each of the individual fibres. However, as with single fibre systems, this can be reduced by angle polishing the fibre ends or by using fibres with anti-reflection coatings.

## 3.3 OCT

CFB's are widely used in endoscopic microscopy, however, their application in OCT is novel. The feature of the CFB that enables them to be used in OCT is that all fibres have an equal OPL. The OPD between adjacent pixels is therefore maintained and so the spectral frames of FF-SS-OCT are preserved through the bundle.

### 3.3.1 *Common path design*

An apparent progression from a single fibre PS-OCT system to a CFB based FF-OCT system would be to replace both the object and reference arm single mode fibres with two CFB's of equal length. The object under investigation could then be probed with the object arm CFB, and the OPD of all lateral pixels across the object CFB then matched with the corresponding fibres of equal OPL from the reference arm CFB. Aligning the two CFB's would be difficult in practice, though this would in principle enable FF-OCT use.

However, mechanical stress can be induced onto the object arm CFB from surrounding tissue, and these stresses are not induced onto the reference arm CFB. This causes discrepancies in the state of polarization between the interferometric arms which degrades the fringe contrast, resulting in a loss of SNR in the transmitted image, [31].

It is practically impossible to artificially induce the exact same stress onto the reference arm CFB. Instead a solution is to incorporate a common path interferometer, [32], in which both the object and reference arms follow a common path through a shared bundle, and hence no discrepancies are introduced in the state of polarization between the arms.

A common path CFB can facilitate both the transmission of light from the bulk part of the system to the object, and the collection and re-transmission of the backscattered light from the object to the detector.

#### *Unbalanced Detection*

A consequence of the common path design is that is impossible to perform balanced detection, which would significantly decrease the amplitude of detected noise.

### 3.3.2 Multimoding

To incorporate CFBs into OCT the multimoding behavior of the constituent fibres must be considered. This is the phenomenon by which multiple modes are transmitted through the many fibres, in addition to their fundamental mode. When the light output from the CFB is detected and an FT taken to generate an image, the higher modes act as higher frequency modulations of the detected current, and so result in artefacts in the FT image at given depths. These have no correspondence to real object reflectors and are often referred to in literature as 'ghost artifacts'.

The number of modes that can be supported by each constituent fibre is given by the normalized wave number,  $V$ , which is wavelength dependent and determined by the numerical aperture,  $NA$ , and core diameter,  $d$ , of the constituent fibres.

$$V = \frac{\pi \cdot d \cdot NA}{\lambda} \quad (3.2)$$

The OPD discrepancy introduced between the desired fundamental mode and the higher mode artifacts is proportional to the length of the bundle and it has been shown that for lengths exceeding 90 *cm*, that the artifact image is translated sufficiently far in depth as to clear the 2.8 *mm* typical axial range of conventional OCT, [29]. Hence, a solution to removing ghost effects is to have a sufficiently long CFB. However, this comes with the compromise of increased transmission losses and a more elegant solution is desired, especially in FF-OCT, where there are greater transmission losses than for PS-OCT, considering that there are additional transmission losses due to light lost in the regions between fibres.

Another solution, which is a direct consequence of (3.2), is to use a CFB with individual fibres of smaller  $d$ . However, decreasing  $d$  comes with the compromise of a lower pixel fill factor, increasing transmission losses. CFB's constructed with smaller core diameters to reduce multimoding are made available by the manufacturer 'Schott



*North America*'.

### 3.3.3 *Cross-coupling*

The CFB is subject to multimoding in an effort to suppress the effects of cross-coupling, the phenomenon by which light projected onto one fibre is coupled into adjacent fibres, [33]. Light projected into one fibre will emerge from several adjacent fibres at the opposite end of the bundle, therefore leading to a blurring of the transmitted image.

The constituent fibres must be formed with thin external claddings in order to give the CFB a thin diameter, resulting in increased cross-coupling. The fibres are therefore made with a higher  $NA$  than conventional single mode fibres to reduce the effect of cross-coupling. This successfully reduces the affect of cross-coupling, but by (3.2), also results in increased multimoding. The effect of multimoding is generally overlooked by manufactures in preference of reduced cross-coupling, considering that CFBs are designed mainly for use in microscopy.

### 3.3.4 FF-OCT

In Full-field illumination light is lost through the regions of the CFB in which there is inter fibre spacing, [33], resulting in transmission losses in power. The power losses are wavelength dependent, and bundles are typically designed to minimise transmission losses in the visible wavelength range, [34].

The loss of light through inter fibre spacing is characterized by the bundle packing fraction, which is the fraction of the bundle face through which light can be transmitted, and is essentially the ratio of fibre area to inter-fibre area. The bundle packing fraction is typically  $< 40\%$ , [34].

#### *Types of CFB*

There are three types of CFB commercially available, which are referred to as *Fused*, *Wound* and *Leached*.

*Fused* bundles offer the smallest core diameters and therefore induce the least multimoding. However, they are not suitable for applications in any form of endoscopy, due to their large minimum bending radius of several *cm*'s, [34].

*Wound* bundles are formed by winding a number of sub-bundles into a CFB, where each sub-bundle consists of a fixed square matrix of single fibres. Wound bundles are successfully used in microendoscopy and could potentially be incorporated into an endoscopic OCT system.

*Leached* bundles are the optimal choice for use in endoscopic OCT, having been shown to exhibit less cross-coupling than wound bundles at the near infra red wavelengths used in optical biopsy, [2]. Leached bundles are particularly favourable for FF-OCT as they have the greatest bundle packing fraction, and therefore the least transmission losses with Full-field illumination.

### 3.4 FF-SS-OCT

#### 3.4.1 *Justification for SS-OCT*

When coupled with a FF-OCT scheme, both of the FD-OCT methods, Spectral Domain, (SD-OCT), and Swept Source, (SS-OCT), would be capable of acquiring an entire volume in one acquisition. Both are more suitable for performing endoscopic OCT than conventional TD-OCT due to their capability of fast acquisition and high sensitivity.

Although both SD-OCT and SS-OCT may be used for single fibre endoscopic OCT systems, only SS-OCT is suitable for OCT systems incorporating CFBs. This is because in SS-OCT the spectral frames are encoded in time, in contrast to SD-OCT, in which the spectral frames are instead spread within the spectral domain and must be spatially filtered using a spectrometer.

In SS-OCT the time encoded signal is generated at the source, such that the spectral frames are resolved in time before they are transmitted through the bundle, and hence each spectral frame can be delivered directly from the output of the CFB to a detector. On the contrary, a SD-OCT system would require spatially resolving the light emitted from each individual fibre, and hence would require precisely aligned diffraction gratings for each of the thousands of fibres at the detector end of the CFB.

#### 3.4.2 *Effects of the CFB*

A study conducted onto the effects of CFB's on FF-SS-OCT demonstrated there was little discrepancy in axial resolution between that of bulk system and that of a system incorporating a CFB, [35]. The system incorporating a CFB was found to have a marginally reduced depth range.

A side viewing PS-OCT system incorporating a CFB and a tuneable swept source for depth scanning has also been demonstrated, [36], and has been shown to successfully produce volumes from non-biological material, specifically a metallic duct. When com-

pared with a theoretical axial resolution given by the tuning bandwidth of the source, it was found that multimoding caused a variation and general broadening of axial resolution with increased OPD, [36]. It was found that multimoding caused a fluctuation in intensity at the detector, causing the tuning coherence power spectrum at detection to deviate from a Gaussian function. This resulted in a general broadening of the tuning coherence function with increased OPD, and hence a decrease in axial resolution with depth.

### 3.4.3 *Advancements in miniaturization*

There are novel methods being investigated for generic endoscope probes that could potentially be applied to a CFB incorporating FF-SS-OCT system. One possibility is to use a GRIN lens at the endoscopic probe head, which could then be directly fused to the input of a CFB. This has already been demonstrated on a probe head, [37], though not within an OCT system. An ultra-thin forward facing probe with a maximum diameter of just  $50\mu\text{m}$  was produced by the method of GRIN to CFB fusing, and was shown to successfully produce non interferometric images of biological tissue through white light transmission and fluorescence imaging. A similar incorporation of a GRIN lens into the proposed compact probe head design could be utilized in future work to construct an ultra-thin forward facing FF-SS-OCT probe head.

Another possibility is to remove the necessity for focusing optics at the probe head completely, by the method of holography. Such lensless endoscopic systems using a CFB and a tuneable swept source have been demonstrated for *in vivo* holographic imaging of skin, [38].

## CHAPTER 4

### Proposed System Design and Technical details

#### 4.1 Probe head overview

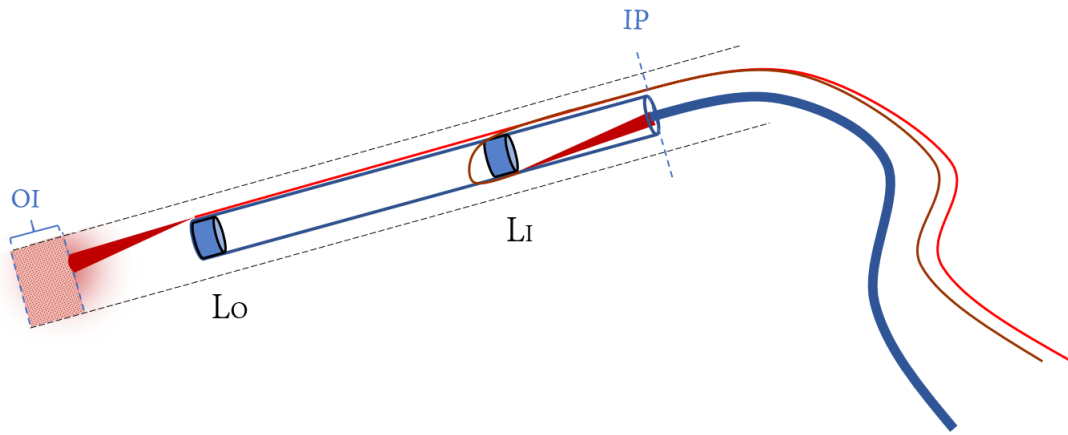


Figure 4.1: Illustration of the operation of the Compact probe head.  $L_O$ : Objective lens,  $L_I$ : Imaging lens, OI: Object Interval/Coherence Gate, IP: Imaging/Interference Plane, Red line: Object launching fibre, Brown line: Reference launching fibre, Blue line: Coherent Fibre Bundle, (CFB).

The design presented is a forward facing, Full-field probe, which is cylindrical in shape, with the axis of the cylinder serving as the probe's optical axis. Encompassed within the probe is a novel off-axis interferometer, which creates an interference pattern at the rear facet of the probe, at the interference plane (IP). The rear facet can be attached to a CFB to form a common path interferometer or it can be projected directly onto a camera.

Two lenses are placed within the probe to create a telescope: an objective lens,  $L_O$ , is positioned directly at the front face of the probe, and an imaging lens,  $L_I$ , is positioned a focal length away from the back face of the probe. An object launching fibre is routed into the probe on to the top of the  $L_O$ , where it launches a divergent light beam onto the object in front of the probe. Light is backscattered off the object and relayed to the IP by the two lenses, enabling the probe to fixed wavelength imaging.

### *OCT Operation*

The probe is transformed into an interferometer by the inclusion of a reference arm launching fibre, which is routed into the probe and terminates below  $L_I$ , launching a divergent beam of light directly onto the IP. At the IP the object and reference waves are superimposed and an interference signal is generated. The object volume occupied by the instantaneous coherence length, from which the backscattered light will interfere with the reference beam at IP, is referred to as the Object Interval (OI).

The interferometer has an intrinsic OPD between its arms, with the object arm covering a greater OPL than the reference arm. Therefore, the OPL of the reference launching fibre must be made longer than the object launching fibre by an additional length, to ensure that the instantaneous coherence gate of the interferometer and the object under investigation are aligned. A free space section has been introduced into the reference arm, enabling OPL to be accurately controlled.

### *Compactness*

Both of the arms of the interferometer are made to run along the same optical axis, giving the probe head a cylindrical geometry which could potentially be made extremely thin. This can be compared to a Michelson interferometer like probe, in which the direction of arms are orthogonal, making for a more difficult miniaturization.

The determining factors on the size of the probe head are the diameter and focal

length of the two lenses. The size of the probe is then ultimately determined by the dimension of the casing in which the lenses and launching fibres are housed.

4.1.1 *Optical path of Launching fibres*

A schematic diagram of the optical paths of the object launching fibre (OLF) and reference launching fibres (RLF) from the source output to probe head input, are given in Fig. 4.4, in which OLF is represented by the upper path and RLF the lower path. The light from a Swept Source is directly input into a feeding fibre (FF), which is then fed into a DC with a 50/50 splitting ratio, which splits the light into the object and reference arm launching fibres. The two launching fibres then launch divergent beams into the Compact probe head, (CPH), which interferes the two beams and transmits the interference signal to a detector, (D).

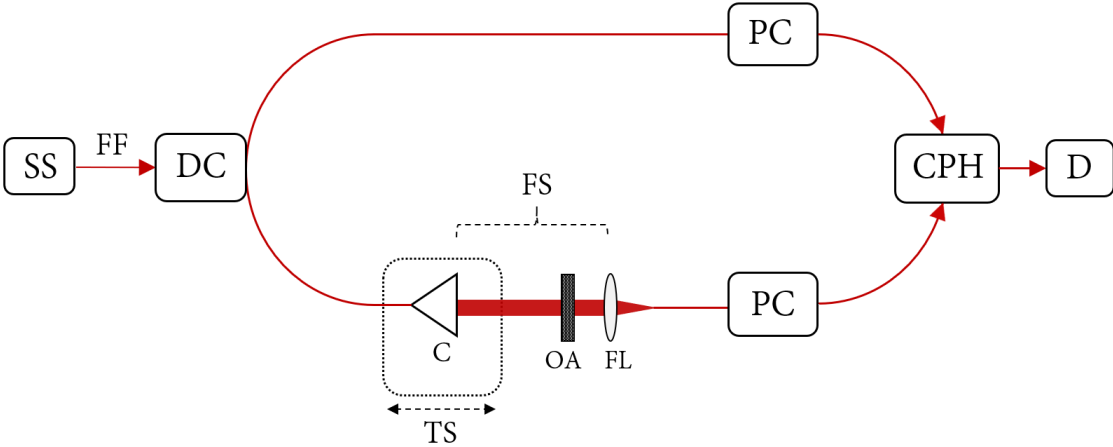


Figure 4.2: Optical path of launching fibres. SS: Swept Source, FB: Feeding fibre, DC: Directional Coupler, TS: Translation Stage, C: Collimator, FS: Free Space Section, OA: Optical Attenuator, FL: Focusing Lens, PC: Polarisation Controller, CPH: Compact Probe Head.

### *Object arm*

The object arm launching fibre is passed through a Polarisation Controller, (PC), which enables the net direction of polarisation of light passing through the fibre to be adjusted. The type of PC used was a 'Newport F-POL-IL', a compact device which applies pressure and torsion onto a fibre to adjust the direction of polarization of light within the fibre. The object arm launching fibre is output from the PC and input into the CPH.

The OPL of the object arm launching fibre is given by  $OPL = n \cdot l_O$ , where  $l_O$  is the length of the fibre and  $n$  is its refractive index.

### *Reference arm*

The reference arm fibre initially launches light through a collimator mounted on a translation stage, forming a collimated beam in free space. The collimated beam is passed through an optical attenuator, (OA), which can be controlled to reduce 0% – 100% of the beam's optical power, therefore enabling the power of the reference beam to be matched with that of the weaker backscattered object beam, which in turn can be used to improve SNR. The free space beam is re-injected into a reference arm launching fibre by a focusing lens (FL), and the launching fibre is then fed through a PC before being routed into the CPH.

The length of the reference arm, from the DC to the CPH can be given by  $OPL = (n \cdot l_R) + l_{FS}$ , where  $l_R$  is the collective length of reference arm fibre up to the CPH and  $l_{FS}$  is equal to the length of the reference arm free space section.



### *Polarisation control*

The amplitude of the coherence function of two interfering waves is dependent on the state of polarization of the two waves. PC's are used to affect the orientation of polarization of the two object and reference beams, in order to affect their mutual coherence function.

It was found by adjusting each PC in turn that the amplitude of the cross-correlation signal was dependent on the relative difference in orientation of polarisation between the object and reference beams, and hence the SNR was found to be dependent on their orientation of polarisation.

#### 4.1.2 Lens configuration

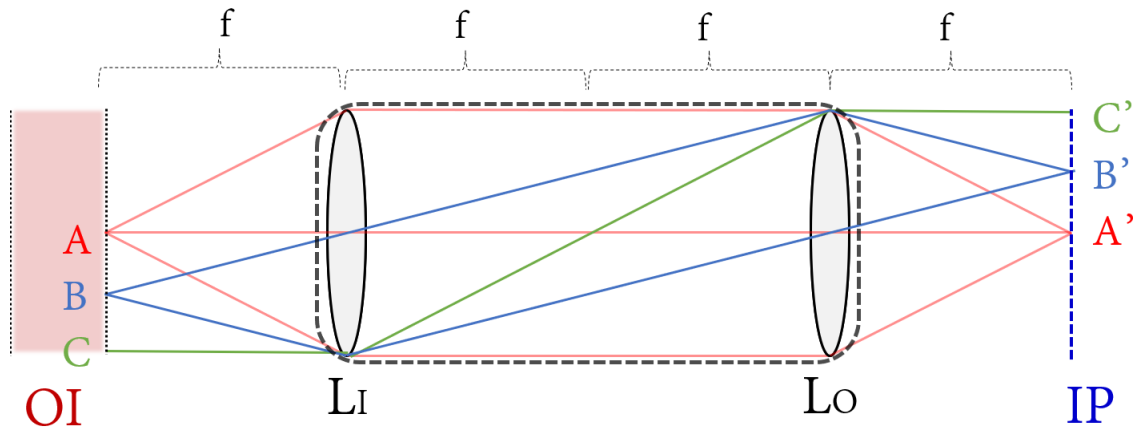


Figure 4.3: Diagram of ray traces through the probes telescope. OP: Object plane, IP: Imaging Plane,  $L_O$  and  $L_I$ : Object and Imaging Lens of equal focal,  $f$ .

*Fig. 4.3* illustrates the lens configuration within the probe and the ray traces taken by the backscattered light from the OI to the IP. The probe head is indicated by the bold dashed line and encompasses two identical lenses of focal length  $f$  at each of its ends. The lenses are positioned in a telescopic configuration, creating an imaging conduit between the depth plane of the OI selected by the swept source, and the Imaging plane, (IP), where any backscattered light emitted from any scattering point along OP is relayed through the probe head and replicated onto IP.

Illustrated in *Fig. 4.1* are the ray traces taken by three scattering points placed along the surface of the OI. Rays from A, B and C, reach their three corresponding positions in the IP, A', B' and C'.

### *Use of Achromatic lenses*

Chromatic aberration has the potential of introducing a dispersion mismatch between the two arms of the interferometer, considering that the object arm contains two lenses and the reference arm none. Chromatic aberration is a result of the wavelength dependence of refractive index, and causes a wavelength dependent axial translation of the focused beam about a lens's focal point. Hence, there will be a dispersion of the object arm about the lens's focal point, illustrated in *Fig. 4.4* by  $\Delta f$ .

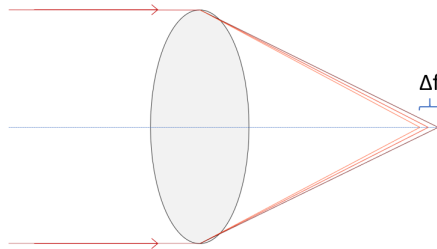


Figure 4.4: Illustration of chromatic aberration through a single lens.

The dispersion is reduced by using achromatic doublet lenses, which exhibit reduced chromatic aberration. These are formed of two lenses, a convex lens of positive dispersion, and a concave lens of negative dispersion, which combined converge the maximum and minimum wavelengths over a given range of light onto the same focal point, with the central wavelength slightly displaced from the focal point. The minimum and maximum wavelengths are given by the lens's  $\lambda$  range.

### 4.1.3 Specifications

#### Lenses

The lenses used were a pair of identical Achromatic doublets, [39], with the following specifications;

Focal length, $f$	40 $mm$
Diameter, $2r$	6.25 $mm$
$\lambda$ range	400 - 1000 $nm$

Table 4.1:  $L_O$  and  $L_I$  lens specifications.

The focal length of the lenses are given at a specified wavelength of  $\lambda = 587.6nm$ , which is different from the wavelength used. The tuning range of the FF-SS-OCT system is within the Near-Infrared region, (NIR),  $\lambda \approx 820 : 880nm$ , and hence there will be a slight difference between the specified focal length and the real focal length within the system.

#### Optical Fibres

Single mode optical fibre, with transmission wavelength maximum at 830nm, (SM800), is used for the feeding fibre, object fibre and reference fibre. SM800 fibre, [40], has the following specifications;

Operating $\lambda$	830 $nm$
$\lambda$ range	730:930 $nm$
Core index, $n$	$\approx 1.48$
NA	0.12
Core diameter	5.6 $\mu m$
Cladding diameter	125 $\mu m$

Table 4.2: SM800 fibre specifications.

#### 4.1.4 Divergence of beams

The beam divergence from a single launching fibre is illustrated in *Fig. 4.5*. Light is emitted from the fibre in a cone with a half acceptance angle given by  $\theta$ , where  $\theta$  is related to the NA of the fibre by  $NA = \sin\theta$ . Notice that the light is emitted in a cone, with a spherical shaped front.

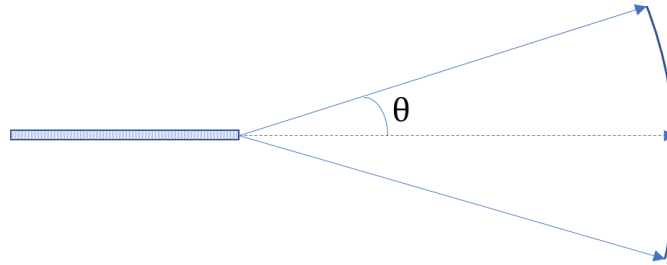


Figure 4.5: Illustration of Beam Divergence from an optical fibre.

### 4.2 Off-axis Interferometer Design

The optical path taken by the object and reference beams are given in the interferometer design, *Fig. 4.6*. Divergent light is launched from an object launching fibre, (OLF), onto an Object, (O) and the backscattered light is relayed by the probes lenses onto the IP. The OLF is inclined at an angle  $\theta_i$  to the optical axis of the interferometer. At the same time divergent light is launched from a reference launching fibre, (RLF), onto IP, at an equal and opposite inclination angle,  $\theta_i$ .

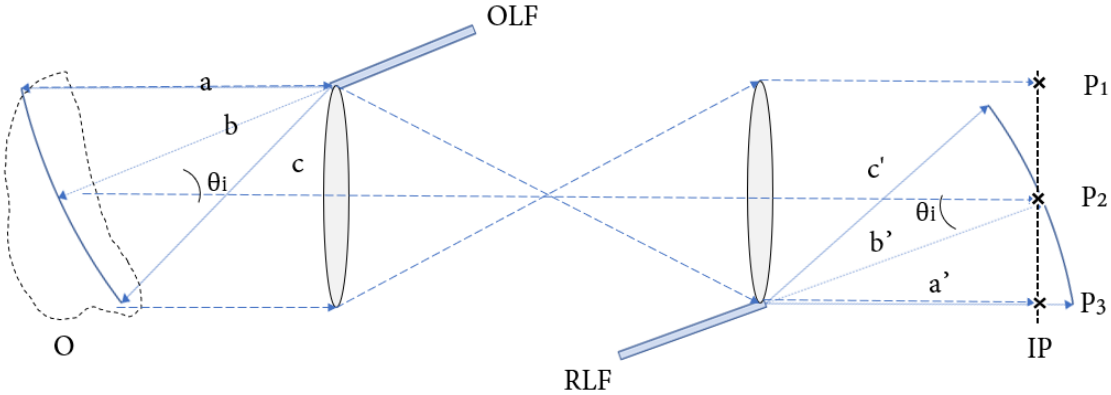


Figure 4.6: Optical path of Object and reference beams through the interferometer. OLF: Object Launching Fibre, RLF: Reference Launching fibre, O: Object, IP: Interference Plane,  $\theta_i$ : Launching Fibre inclination, (a,b,c): Extremity ray traces of divergent beams, (P1,P2,P3): Vertical points of IP.

It is seen from *Fig. 4.6*, that the the wavefront of the divergent object beam is not orthogonal in its incidence with the object, due its spherical wavefront and inclination with the optical axis. As a result, for a given lateral cross-section through the object, the OPL of points along the lateral direction of the beam are not equal. If we imagine a cross section through the object then at any given lateral plane, ray trace *a* will have travelled the longest OPL, and ray trace *c* the shortest.

It should be noted that if a specular surface, such as a mirror, is positioned in the OI instead of a scattering object, then the mirror must be tilted in the opposite direction to  $\theta_i$  to ensure that the reflected light is directed into the objective lens at the front of the probe.

#### 4.2.1 Lateral OPL matching

One of the principle features of the off-axis design is that the two launching fibres are inclined at equal and opposite angles to the optical axis of the probe. This has the effect of equating the OPL of both object and reference arms along all lateral positions of IP. In principle, the OPD of all pixels along IP are matched, enabling the spectral frames of FF-SS-OCT to be preserved.

#### *Analysis*

The two launching fibres are inclined within the vertical axis of the probe only. Hence there is no variation in OPD along the horizontal direction of IP, and it is valid to consider the OPD between the object and reference arms in the vertical direction of IP only. We can define the OPL of the extremities of ray traces taken by the object and reference arms and then calculate OPD of the ray traces at the IP. The extremities of ray traces from each divergent beam are illustrated in *Fig. 4.6.*,

If we select a given lateral plane of the OI, then all scattering points along the lateral plane will be detected at their corresponding positions at the IP having taken an equal OPL. This principle is true for any imaging conduit telescope, because the lateral variation in the thickness of the lenses introduces an extra OPL, which compensates for the shorter distance covered by the ray trace through the centre of the probe, compared to those that travel a greater distance at the extremities of possible paths. The OPD between the object and reference arms resulting solely from the journey of backscattered light from the object to the detector is approximately  $4f$ .

We need then only consider the OPD of positions  $P_1$ ,  $P_2$  and  $P_3$  in terms of the paths  $a$ ,  $b$ , and  $c$  and  $a'$ ,  $b'$ , and  $c'$ . The OPD at the positions  $P_1$ ,  $P_2$  and  $P_3$ , which are shown in Fig. 4.6. by the black crosses along IP, are given by;

$$\begin{aligned}
 OPD_{P_1} &= c - c' \\
 OPD_{P_2} &= b - b' \\
 OPD_{P_3} &= a - a'
 \end{aligned}
 \tag{4.1}$$

If both launching fibres are inclined to the optical axis of the probe at the same angle, and at the same distances from the object and the IP respectively, then the OPL taken by  $a$ ,  $b$ , and  $c$  are equal to the OPL taken by  $a'$ ,  $b'$ , and  $c'$ .

Hence, all lateral points along IP have an identical OPD, provided both launching fibres are inclined at the same angle to the optical axis from opposite ends of the probe, and that the free space section of the reference arm is made to be a length of  $4f$ . In this way the off-axis interferometer is similar to an on-axis Full-field Michelson interferometer, in that the OPD of every pixel on a given spectral frame is the same, irrespective of the pixels lateral position.



#### 4.2.2 *Off axis interference*

The object arm has normal incidence onto IP, as the telescopic lens configuration returns the object arm in a direction orthogonal the optical axis of the probe, however, the reference arm is incident onto the IP at an offset angle, given by the inclination angle of the reference arm launching fibre,  $\theta_i$ .

The effect of the off axis incidence of the two beams is to induce another interference pattern at the IP of the probe. The interference pattern oscillates in the lateral direction along each spectral frame, forming a pattern of concentric rings, which are centred at the position of contact between IP and the locus of the reference beam.

4.2.3 Limited FOV

The direct launching of the object beam from a single mode fibre imposes some imitations in respect of the area of the object that can be illuminated, and therefore the permissible FOV. The area illuminated is determined from the divergence of the SM800 fibre, and, the distance between the fibre and the object. The divergence is wavelength dependent, and at a constant wavelength is given by the fibre’s NA.

An experimental graph of FOV as a function of fibre object separation distance, for SM800 fibre at  $\lambda = 850 \text{ nm}$ , is given in Fig. 4.7.

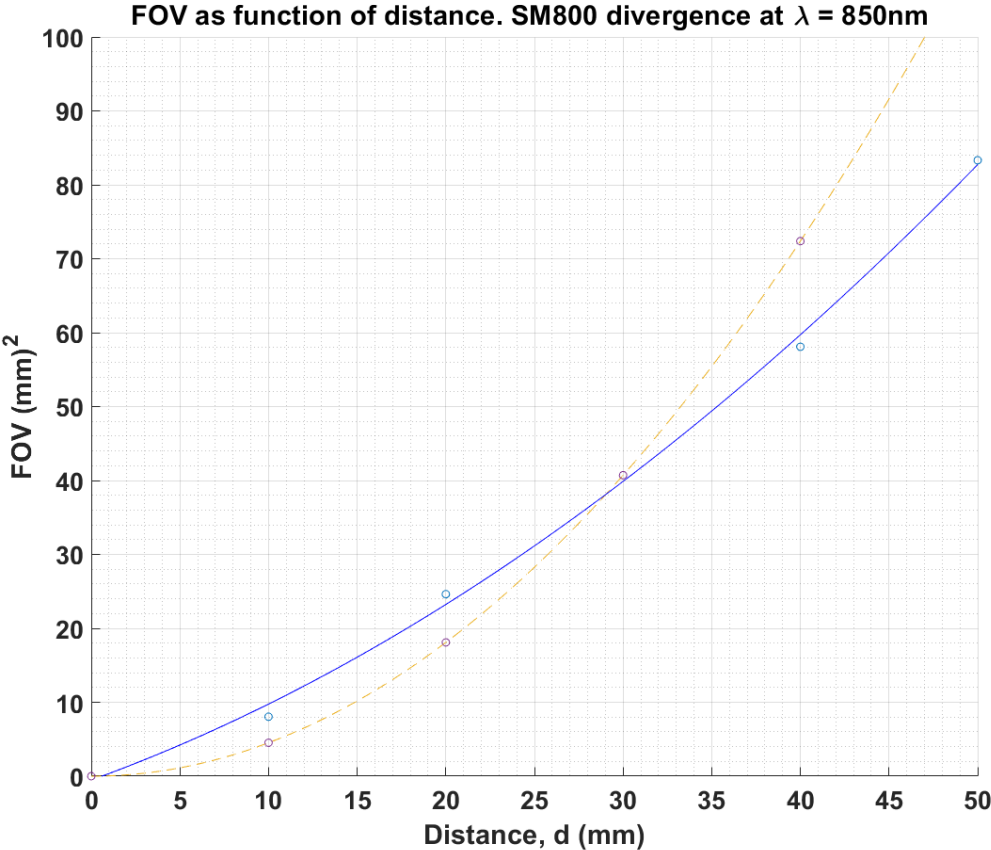


Figure 4.7: FOV from a SM800 single fibre at distance  $d$ , for constant  $\lambda = 850 \text{ nm}$ . Blue: Experimental, Red: Theoretical.

The experimental procedure for obtaining *Fig. 4.7* was as follows. Sweeping was stopped and a fixed wavelength with a narrow linewidth was emitted from the source. This was launched directly via a SM800 fibre onto a CMOS camera, and a measurement of the beam diameter performed for different values of distances between the fibre and the camera, starting from  $1\text{cm}$  in increments of  $1\text{cm}$ . For each increment the number of pixels illuminated on the CMOS camera was measured, from which the area illuminated was calculated using the known pixel density of the CMOS camera, [41].

The theoretical FOV values are calculated by (4.2), where NA represents the NA of the fibre and  $d$  is its distance from an object.

$$FOV = \pi \cdot (d \cdot NA)^2 \quad (4.2)$$

A quadratic curve was fit to the experimental and theoretical data sets to obtain the two curves seen in *Fig. 4.7*.

It is seen that a larger separation is required in order to raise the FOV towards the accessible FOV of the CMOS sensor, which for the camera used in the system was  $256.97\text{mm}^2$ , [41]. It should be noted that the FOV of the CMOS is also limited by the selected *fps*.

The FOV is also limited by the cross-sectional area of  $L_1$  and  $L_2$ , as this defines the area of the collimated Full-field object beam incident onto the CMOS sensor, provided there is no magnification introduced. With radii of  $3.175\text{mm}$ , the maximum FOV obtainable from  $L_1$  and  $L_2$  was  $30.68\text{mm}^2$ .

### *Analysis*

If we approximate the distance between the object arm launching fibre and the camera sensor as  $f$ , then we can infer from *Fig. 4.6* that the experimental FOV of the current system, at  $f = 40mm$  separation, is  $58.09mm^2$ . The cross sectional area of the objective lens is  $30.68mm^2$ , and hence at the current lens and fibre specifications, it is the lenses that impose a limit on the permissible FOV, and not the divergent beam. However, it is seen from *Fig. 4.6*, that maintaining the same lens diameter, and reducing  $f \leq 23.6mm$ , would mean the divergence from fibre becoming the limitation on the permissible FOV.

This presents an issue, as reducing  $f$  is desirable. The length of the probe is determined by  $f$ , and so reduction of  $f$  would reduce the size and hence invasiveness of the probe head. Reducing  $f$  also means that a greater fraction of backscattered light from the object would be captured by the objective lens, therefore increasing the power of the backscattered object arm. This would increase the systems SNR and sensitivity, enabling objects with less reflectivity to be detected.

Hence, a means of increasing the divergence of light from the launching fibres would need to be developed in order to maintain a viable FOV were the size of the probe to be reduced.

### 4.3 System Operation

The entire working system can be broken down into two principle parts; the operations part, at the distal end of the system, and the probe head part, at the proximal end of the system. The operations part is further divided into blocks, a Swept Source block, (SS Block), and a Detection and Processing block, (DP Block).

The two principle parts can be connected using a CFB and two single mode fibres. A schematic illustration of the two parts of the system, connected by CFB and two launching fibres, are given in *Fig. 4.13*.

#### 4.3.1 Bulk and Bundle versions

The entire system can be assembled in two possible versions, a bulk version and a bundle version.

In the bundle version, illustrated in *Fig 4.13*, the CFB functions to transmit the signal from the output of the probe head to the sensor of the CMOS camera. The CFB is a Schott Leached Imaging Bundle, [30], with dimensions given in *Tab. 4.3*.

Outer Diameter	1.65mm
Pixel Size	11.6 $\mu$ m
# Pixels	18000

Table 4.3: Schott Leached imaging Bundle dimensions.

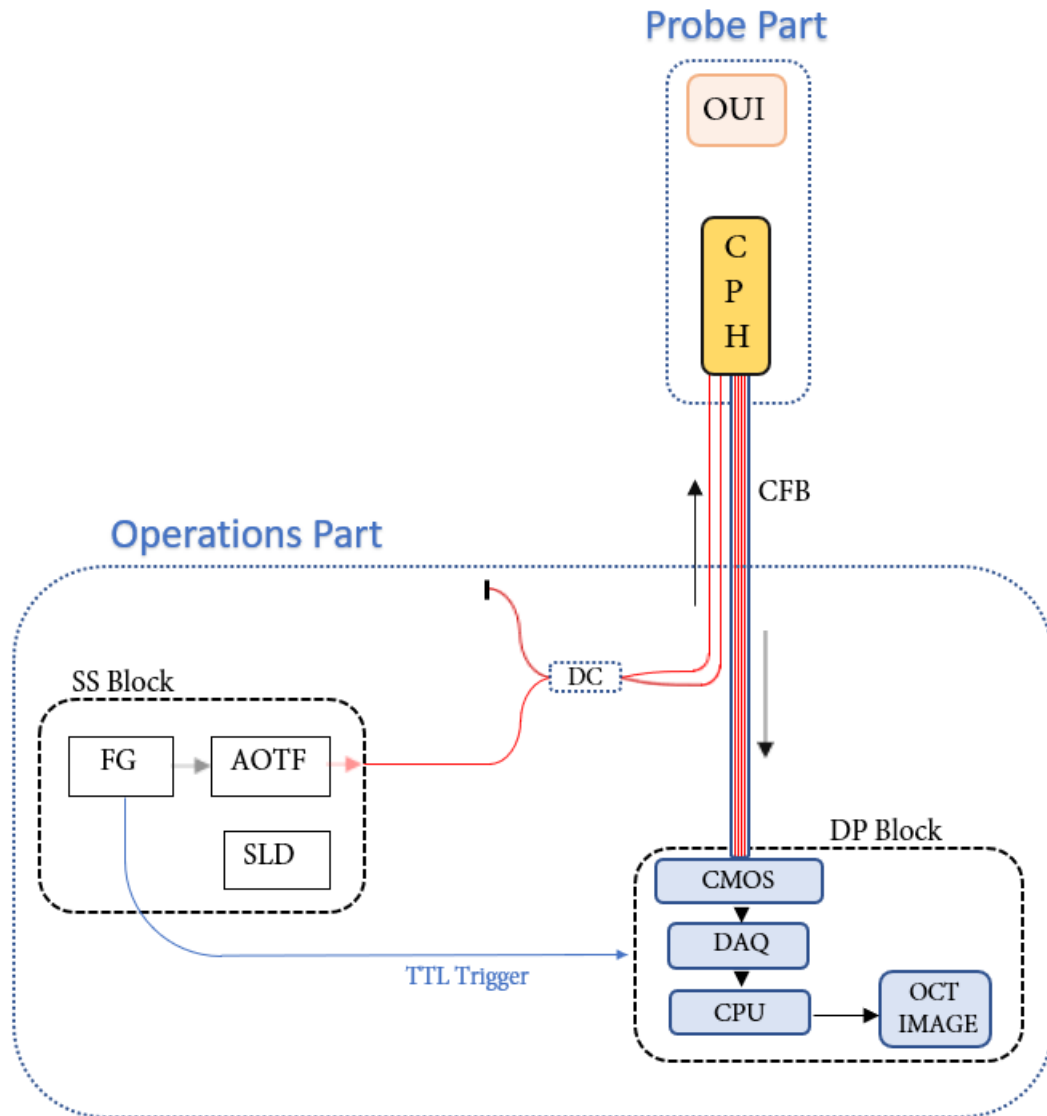


Figure 4.8: Operation and probe parts schematic. FG: Function Generator, AOTF: Acousto-optic tuneable filter, SLD: Superluminescent diode, DC: Directional coupler, CPH: Compact probe head, OUI: Object under investigation, CFB: Coherent Fibre Bundle, CMOS camera, DAQ: Digital Acquisition Device, CPU: Computer Processing Unit.

In the bulk version the CFB is removed and the two main parts, probe and operations, are grouped together. The probe head then functions as an interferometer within a bulk FF-SS-OCT system, with the interference signal output from the probe directly input onto the sensor of the CMOS camera.

#### 4.3.2 Swept-Source Block

The SS Block is comprised of three components; a SLD, an AOTF, and a Function Generator (FG).

##### *Function Generator*

The FG serves two purposes, to drive the tuning of the AOTF, and to trigger a set of exposures of the CMOS camera. To drive the AOTF the FG outputs an electrical signal with a sawtooth waveform. This is referred to as a driving voltage, and is transmitted along a co-axial cable and connected via BNC connectors to the input of an AOTF.

The driving voltage,  $V(t)$ , is given by,

$$V(t, \psi) = \frac{V_{pp}}{\Delta T} \cdot \left(t + \frac{2\pi}{\psi}\right) + v_o \quad (4.3)$$

The period,  $\Delta T$ , phase,  $\psi$ , and peak to peak voltage,  $V_{pp}$ , are all controlled by using the interface of the FG.

##### *AOTF and SLD*

The AOTF and the SLD are combined into one source, within a stand alone commercial unit called a 'Broadsweeper-840 (BS0002)'. The tuning equation of the Broadsweeper-840 is determined from  $V(t)$  by, [22],

$$\begin{aligned}\lambda(t) &= \lambda_0 - \lambda_V[V(t) - V_0] \\ &\approx 880nm - 60nm/V \cdot [V(t) - 3.5V]\end{aligned}\tag{4.4}$$

The tuning equation demonstrates that  $\lambda(t)$  is linearly decreased as  $V(t)$  is linearly increased, hence performing the required spectral tuning.  $V_{pp}$  must be no greater than the bias 3.5V, in order to limit  $\lambda(t)$  to within the optical tuning range.

The driving voltage output from the FG was input into an optical spectrum analyser to measure its peak to peak voltage. The measured  $V_{pp}$  was then adjusted to optimise the bandwidth of the tuning curve, without exceeding its limited range.

### *Output*

The output of the SS Block is a series of time encoded instantaneous power spectra, which are periodically tuned in optical wavelength by the tuning equation, (4.11). There are two stages to (4.11), a sweeping stage and a lag stage. In the sweeping stage there is a linear decrease in  $\lambda(t)$ , corresponding to an approximate linear increase in  $k(t)$ . The lag stage is then the period in-between the sweeping stage, in which  $k(t)$  returns to  $k(0)$ .

In real time imaging, in which multiple A-scans are repeatedly obtained, the time taken to complete each A-scan is given by the sum of both sweeping and lag intervals, which is referred to as the sweeping time,  $\Delta T$ . The speed of the system is then ultimately given by  $\frac{1}{\Delta T}$ .



### *Performance*

The BroadSweeper-840 has two power modes, high and low, for which the source emits  $P \leq 5mW$  and  $P \leq 1mW$  respectively. The low power mode was used for adjustments, while for imaging the high power was used to compensate for power losses in the system and to obtain a better SNR.

The performance features of BroadSweeper-840, when operating in either power mode is given in *Tab. 4.4*, [22]. It is seen from *Tab. 4.4* that using the higher power mode for imaging comes at a slightly reduced tuning bandwidth and hence a marginally worse axial resolution.

	<b>Low</b>	<b>High</b>
$\lambda_0$	850 nm	850 nm
$\Delta\lambda$	55 nm	47 nm
$lc_{\Delta\lambda}$	11.59 $\mu m$	13.57 $\mu m$
$\delta\lambda$	0.04 nm	0.04 nm
$lc_{\delta\lambda}$	1.594 cm	1.594 cm
$\Delta T_{fast} - \Delta T_{slow}$	5ms - 1s	5ms - 1s

Table 4.4: Performance features of the BroadSweeper-840

### 4.3.3 Detection and Processing Block

#### CMOS - Mikotron EoSens® CL Full

A CMOS camera was chosen over the alternative choice of a Charged-coupled Device, (CCD), as in general, CMOS cameras present more favourable features for FF-SS-OCT, operating at higher permissible *fps* and with a higher dynamic range, the latter meaning a greater SNR could potentially be detected by the camera.

The camera selected for the system was a Mikotron high-speed CMOS camera. The specific model was a 'Mikotron EoSens® CL Full', which had the following performance features, [41]:

Pixel size	14 x 14 ( $\mu m$ )
# Pixels	1280 x 1024
Pixel separation, $\Delta_{xy}$	14 $\mu m$
FOV	17.92 x 14.34 ( $mm$ ) = 256.97 ( $mm^2$ )
Fill Factor	40 %
Dynamic Range	90dB

Table 4.5: Performance features of the Mikotron EoSens CL Full

The permissible  $fps$  and Active pixel area of the CMOS camera are inversely related and so impose limitations on each other. The CMOS was set to operate at a 2x8 Tap-Bit mode, which determined a maximum  $fps$  value at a given FOV. A set of combined values of  $fps$  and active area in pixel number, are given in *Tab. 4.6*, [41], where the FOV and  $fps$  values are approximate and are given to three significant figures.

	Active area (#)	$\approx$ FOV ( $mm^2$ )	$\approx fps_{max}$
A- Scan	1 x 1	0.000014	15300
B- Scan	1 x 100	0.0196	15200
	1 x 400	0.0784	14800
	1 x 1024	0.201	14000
Volume Scan	100 x 100	1.960	3900
	200 x 200	7.840	1770
	400 x 400	31.40	662
	1024 x 1280	257.00	110

Table 4.6: Set of combined values of Active area and  $fps$  achieved by the Mikrotron EoSens CL Full

It is seen then from *Tab. 4.6* that  $fps$  is greatly diminished for larger FOV, and vice versa. We recall the maximum FOV of the current system, limited by the lens cross sectional area, was  $30.86mm^2$ . Obtaining the entire FOV would hence require limiting  $fps$  to  $\approx 660s^{-1}$ . If we were to acquire the maximum possible number of spectral frames, obtained operating in low power mode,  $M = \frac{55 \cdot 10^{-9}nm}{0.04 \cdot 10^{-9}nm} = 1375$ , then this would limit the speed of the system to  $\frac{1}{\Delta T} = \frac{660s^{-1}}{1375} = 0.48Hz$ , which is slower than desirable for *in vivo* imaging. The speed can be increased at the compromise of reducing FOV.

### *Triggering of exposure*

The second output of the FG is a transistor-transistor logic (TTL) signal, which is identical in periodicity to the driving signal input into the Browsersweeper. The TTL is input directly into a Computer Processing Unit, (CPU), and serves as a trigger for initiating a sequence of periodic exposures of the system's CMOS camera at a pre-specified *fps*. The triggering is activated through a Data acquisition processing card, (DAQ).

The phase of the driving signal, (4.10), must be adjusted in order to synchronise the triggering of exposure with the start of each sweeping stage of the Browsersweeper's tuning equation.

Each time a rising edge of the ramped TTL is detected by the CPU, the camera is re-triggered to initiate another round of periodic exposures. The camera is hence made to continuously detect sets of  $M$  spectral frames in synchronicity with source sweeping.

### *Determining fps*

The *fps* of the CMOS camera is matched with the desired number of spectral frames, in relation to  $\Delta T$ . For instance, if the source is set to a scanning frequency of  $2Hz$  ( $\Delta T = 0.5s$ ) and 1000 spectral frames are desired, then a *fps* of  $2000Hz$  is required.

### *Exposure time, $\tau$ .*

The maximum possible exposure time,  $\tau$ , for the pixels of the CMOS camera is then limited by the set *fps*, by the relation,  $\tau < \frac{1}{fps}$ . We recall that the SNR is proportional to the power of the detected beam, and so a larger  $\tau$  will secure a greater SNR, provided  $\tau$  is below the exposure level at which the cameras pixels will become saturated.

### *Conflicting acquisition parameters.*

We desire a large  $M$ , to obtain the best possible SNR and Signal amplitude roll off with OPD. We can obtain a greater  $M$  either by increasing  $fps$  or by increasing  $\Delta T$ . The former reduces the active area of the CMOS sensor, therefore reducing FOV, while the latter of course directly reduces the speed of the system.

### *DAQ - NI PCIe-1429*

The processing of the detected current is facilitated through a Native Instruments PCIe-1429 DAQ, which converts the electrical current incident onto each pixel into a digital signal. The intensity detected by each pixel is converted into a 16-bit integer number, which is stored as an array of unit16 (U16) data type.

#### *4.3.4 Processing method*

The processing of each array of detected current into an OCT image is completed during the lag stage of spectral tuning and is performed by a programme which operates using National Instrument's Laboratory Virtual Instrument Engineering Workbench, (LabVIEW). Several processing loops were developed to serve different purposes and a user interface was designed to give the user the choice of which processing loop to pass the arrays through.

#### *A-scan processing*

The simplest LabView processing loop enabled the user to select, in real time, an A-scan from any single pixel within a Region of Interest, (ROI). The ROI is controlled by the DAQ, and can take any position and size permissible by the available FOV. An A-scan along the axial dimension of the selected pixel is then output, which is continuously refreshed with each spectral sweep. The user is given the choice from either an FFT or an

MS cross correlation, the latter of which requires the user to have initially prerecorded a set of masks.

#### *B-scan processing*

The second LabView processing loop enabled the user to select any lateral B-Scan line across the ROI, again in real time and with the choice of either FT or MS processing. A B-scan along the selected lateral line is output from the processing loop, which again is refreshed with each spectral sweep.

#### *Averaging algorithm*

An algorithm was introduced into the A-Scan processing loop that enabled the user to input a number,  $n$ , of A-scans to be averaged. A simple processing loop was written to iterate through  $n$  arrays to generate an averaged array, which was then processed into an A-Scan by either an FFT or an MS cross-correlation. When the averaging algorithm is active, the output A-scan is not refreshed with each spectral sweep, but is instead updated after  $n$  spectral sweeps have been completed.

#### *DC Removal*

An algorithm was introduced into both A-scan and B-scan processing loops that enabled any given number of initial spectral channels from each given array to be set to zero in intensity. The modified array, with spectral components of the lowest frequency effectively removed, is then processed by an FFT or an MS cross-correlation.

Setting the initial spectral components to zero equates the initial real space OPD positions to zero, hence removing them from the A-scan. This can be used to remove the DC term of the detected photocurrent centred around the OPD= 0 position, however, at the cost of removing components of the object hidden within the D.C. term.

## CHAPTER 5

### Results

#### 5.1 Axial resolution

##### *Method*

A mirror was placed at the OI in front of the probe and the length of the reference arm was adjusted so that the cross-correlation peak of the mirror was shifted to  $OPD = 0.25 \text{ mm}$ . The OPD was then increased up to  $2.75 \text{ mm}$  in increments of  $0.5 \text{ mm}$  and at each interval an average of 50 A-scans was calculated from the central pixel of the FOV. A Gaussian function was then fit to the peaks of each average A-scan, from which their FWHM were then measured and plotted as a function of OPD.

The procedure was repeated to obtain two sets of results, one using FT processing and the other using MS processing. No method of wavenumber calibration was performed on either set of results.

### 5.1.1 FWHM versus OPD

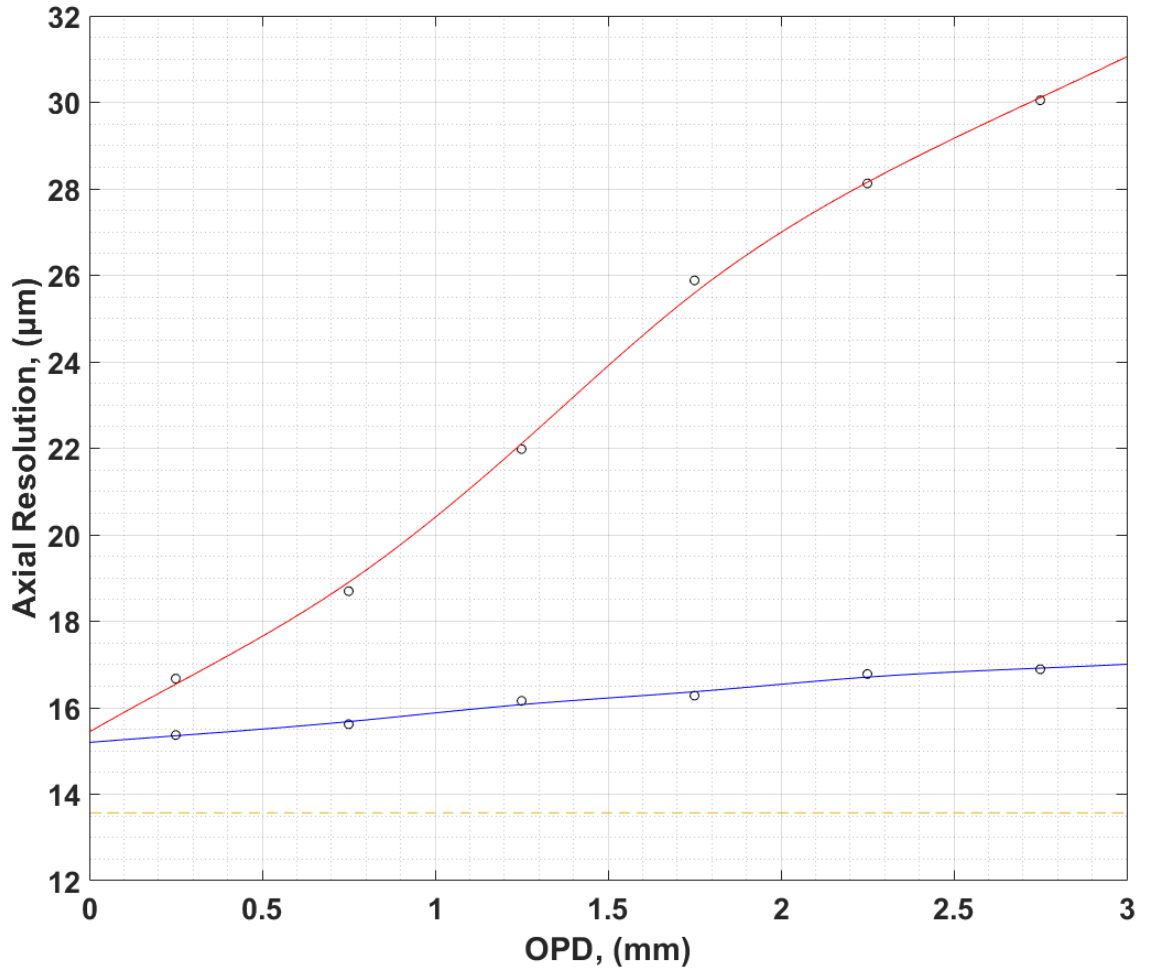


Figure 5.1: Axial resolution dependence on OPD of FFT (red) and MS (blue) processing methods, and ideal (gold).

The FFT curve of *Fig. 5.1* indicates that there is a significant non linearity within the system, which can be seen by the general broadening of FWHM with depth. It is probable that this non linearity is the result of the dispersion introduced by the glass material in the lenses of the probe. The tuning curve of the source is approximately linear, [22], and so would not induce the variation observed. Irrespective of the cause of variation, it seems reasonable to conclude that MS processing secures a better axial resolution throughout the axial range.



It should be noted that the standard practice for FFT processing is to perform a wavenumber calibration, which would likely have reduced the FWHM variation with OPD to the same order as that of MS processing, [19]. Therefore, *Fig. 5.1* is not a fair judgment of the limitations of FFT, rather it is a demonstration of the capability of the MS method.

### *Air Resolutions*

There is a general broadening of the FWHM with OPD for both methods, and therefore the best approximation of axial resolution is at  $OPD = 0$ . We have suggested that dispersion is the cause of variation and by selecting  $OPD = 0$  we evaluate the axial resolution at the OPD position where dispersion is at a minimum.

Measurements of axial resolution were taken with the Broadsweeper operating in high power mode, with a tuning bandwidth of  $\Delta\lambda = 47 \text{ nm}$ , which, assuming no dispersion, generates an ideal axial resolution in air, at  $OPD = 0$ , of  $l_c = 13.57 \mu\text{m}$ .

The experimental axial resolution for FFT and MS methods were found by extrapolating each respective curve to their  $OPD = 0$  value, and were found to be;

$$l_{FFT} = 15.29 \mu\text{m}, \tag{5.1}$$

$$l_{MS} = 15.20 \mu\text{m} .$$

It is possible that for both processing methods the discrepancy from the ideal axial resolution at  $OPD = 0$  is the result of uncompensated dispersion, induced from the material of the lenses and the optical fibre. However, the differences in resolution are little, as the measurements have been inferred from the position of minimum dispersion.

## 5.2 SNR

### 5.2.1 Sensitivity

In the first experiment the sensitivity of the system was obtained, using a window function with the narrowest permissible optical bandwidth of  $\Delta\lambda = 0.040 \text{ nm}$ . The sweeping and camera speeds were set to  $\frac{1}{\Delta T} = 1 \text{ Hz}$  and  $fps = 1175 \text{ Hz}$  respectively.  $\Delta T = 1 \text{ s}$  was chosen as a compromise value, being as large as possible as to increase SNR whilst not scanning at an excessively low speed. An  $fps = 1175 \text{ Hz}$  was chosen to produce the highest possible number of spectral points of  $M = 1175$ , and the maximum permissible exposure of  $\tau = 0.8 \text{ ms}$  was selected. The detected current was processed into an A-Scan by an FFT.

#### *Method*

A set of average A-scans were obtained from a mirror displaced at a range of OPD intervals. A Gaussian function was fit to each OPD peak, from which its amplitude was obtained. The OPD signal amplitudes were then plotted as a function of OPD and the intercept with  $OPD = 0$  was taken as the maximum signal.

A Root-Mean-Square (RMS) was then taken of the noise floor of each A-scan, which was taken from all spectral points excluding those in the regions occupied by the cross-correlation and DC signals. A mean was then taken of all RMS values to generate an approximation of the RMS noise at  $OPD = 0$ . Neither the signal amplitude or the RMS noise at  $OPD = 0$  could be directly measured, as they are both hidden by the D.C. term and so must be inferred.

The  $SNR_{max}$  was found to be given by the ratio;

$$SNR_{Max} = \frac{64876}{2048} = 30.015 \text{ dB} \quad (5.2)$$

Therefore giving a sensitivity of;

$$\frac{1}{R_{Min}} = 0.033 \text{ dB}^{-1} \quad (5.3)$$

This is significantly lower than potential SNR and sensitivity of SS-OCT, with commercial systems having a SNR in the excess of 100 dB, [21].

### *Improvement*

One approach to improving the SNR would be to collect more backscattered light, therefore increasing the detected power of the object beam. If we place a highly scattering object in front of the probe at the OI and approximate the backscattered light to be in the shape of a semi-sphere, then at a focal length  $f$ , the fraction of backscattered light collected by the objective lens may be approximated by (5.4), where  $A_L$  is the cross-sectional area of the objective lens.

$$\frac{A_l}{2\pi f^2} = \frac{30mm^2}{2\pi(40mm)^2} = 0.298 \% \quad (5.4)$$

If we make the assumption that all of the backscattered light collected by the objective lens is conveyed to the pixels of the detector, then the ratio of the backscattered light which is detected is given by (5.4). We can conclude that such a low fraction of  $< 0.3 \%$  is a cause for the low SNR and sensitivity. This meant that it was impossible to detect any backscattered signal when a scattering media, with reflectively lower than the sensitivity was positioned in the OI.

When a specular or quasi-specular object is positioned in the OI, the backscattered light is much more highly directional, and so a much greater fraction of backscattered light is collected and relayed to the detector and so it was possible to obtain images only from quasi-specular objects.

### 5.3 Sensitivity versus OPD

#### 5.3.1 CMOS Shutter Speed, $fps$

The depth sensitivity was first analysed in terms of the  $fps$  of the CMOS camera, keeping the sweeping period,  $\Delta T$ , constant. The detected current was processed by an FFT.

Using  $\Delta T = 0.5 s$ , two values of  $fps$  were selected, 2500  $fps$  and 2000  $fps$ , generating,  $M = 1250$  and  $M = 1000$  respectively. The frame exposure time for both sets of  $fps$  measurements was held constant at  $\tau = 0.45 ms$ . The bandwidths integrated by each frame for different  $fps$  values are given in *Tab. 5.1*.

$fps,$	$M$	$\delta\lambda_M$	$\delta k_M$
2500 $s^{-1}$	1250	0.040 $nm$	208.91 $m^{-1}$
2000 $s^{-1}$	1000	0.047 $nm$	245.47 $m^{-1}$

Table 5.1: Bandwidths for different  $fps$  and  $M$  values

The expected expected performance of the system at the chosen values of  $M$  are given in *Tab. 5.2*

$M$	OPD <sub>-6dB</sub>
1175	3.985 $mm$
1000	3.392 $mm$

Table 5.2: Theoretical axial range for different values of  $M$

### Signal roll off

For both set of  $fps$  values a mirror was placed at a range of OPD intervals, and at each OPD interval an average of 50 A-scans was calculated from the central pixel of the FOV. For both  $fps$  values the set of average A-scans were then plotted as a function of OPD to obtain a signal roll off.

### *Experimental roll off curve*

A Gaussian function was fit to the cross-correlation peak of each average A-scan and the amplitude of each peak was measured to represent the signal amplitude at each given OPD. An experimental signal roll off, representing the envelope of the instantaneous coherence function, was then found by plotting the signal amplitudes as a function of OPD and fitting a Gaussian function to the set of signal amplitudes. The curve was then used to find the experimental  $OPD$  at which signal amplitude had halved.

### *Theoretical roll off curve*

To obtain theoretical curves, the experimental curve is extrapolated to  $OPD = 0$  to obtain the maximum signal strength, i.e.  $A(0)$ . A theoretical signal roll off is then obtained by multiplying  $A(0)$  with the sensitivity function, as given by (2.37).

### *Maximum Sensitivity*

The sensitivity at  $OPD = 0$  was obtained from the SNR at  $OPD = 0$ , the latter calculated by taking the logarithmic ratio of  $A(0)$  to the RMS noise at  $OPD = 0$ , which is approximated by using the same method as in 5.2.1.

$$\underline{fps = 2000 \text{ s}^{-1}, M = 1000}$$

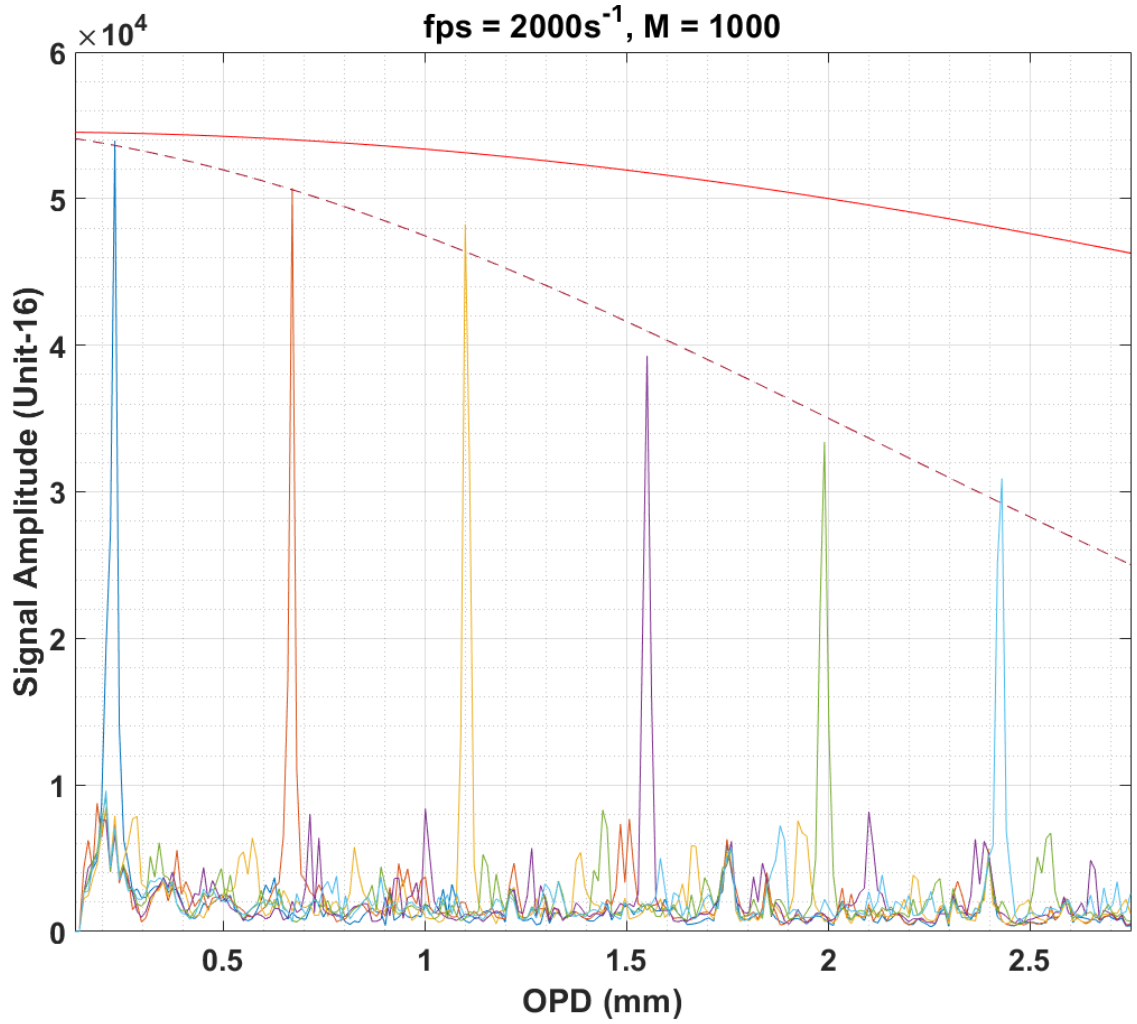


Figure 5.2: Signal amplitude roll off with OPD for  $fps = 2000s^{-1}$ ,  $M = 1000$ . Red dashed: Experimental, Red solid: Theoretical.

The OPD at which the experimental signal amplitude was found to have dropped by half was **OPD = 2.577 mm**.

Fig. 5.2 shows that many Auto-correlation signals are detected at various OPD positions, for example, at  $OPD \approx 1mm$ ,  $OPD \approx 1.5mm$  and at  $1.8mm < OPD < 2mm$ .

Considering that the amplitude of the Auto-correlation peaks are within the envelope of  $lc_{\delta k}$ , they are not diminished, and so have an approximately constant depth

dependent amplitude.

The sensitivity at  $OPD = 0$  is given by  $R_{Min} = \frac{1}{SNR_{Max}}$  where  $SNR_{Max} = 27.624$  **dB**.



$$\underline{fps = 2500 \text{ s}^{-1}, M = 1250}$$

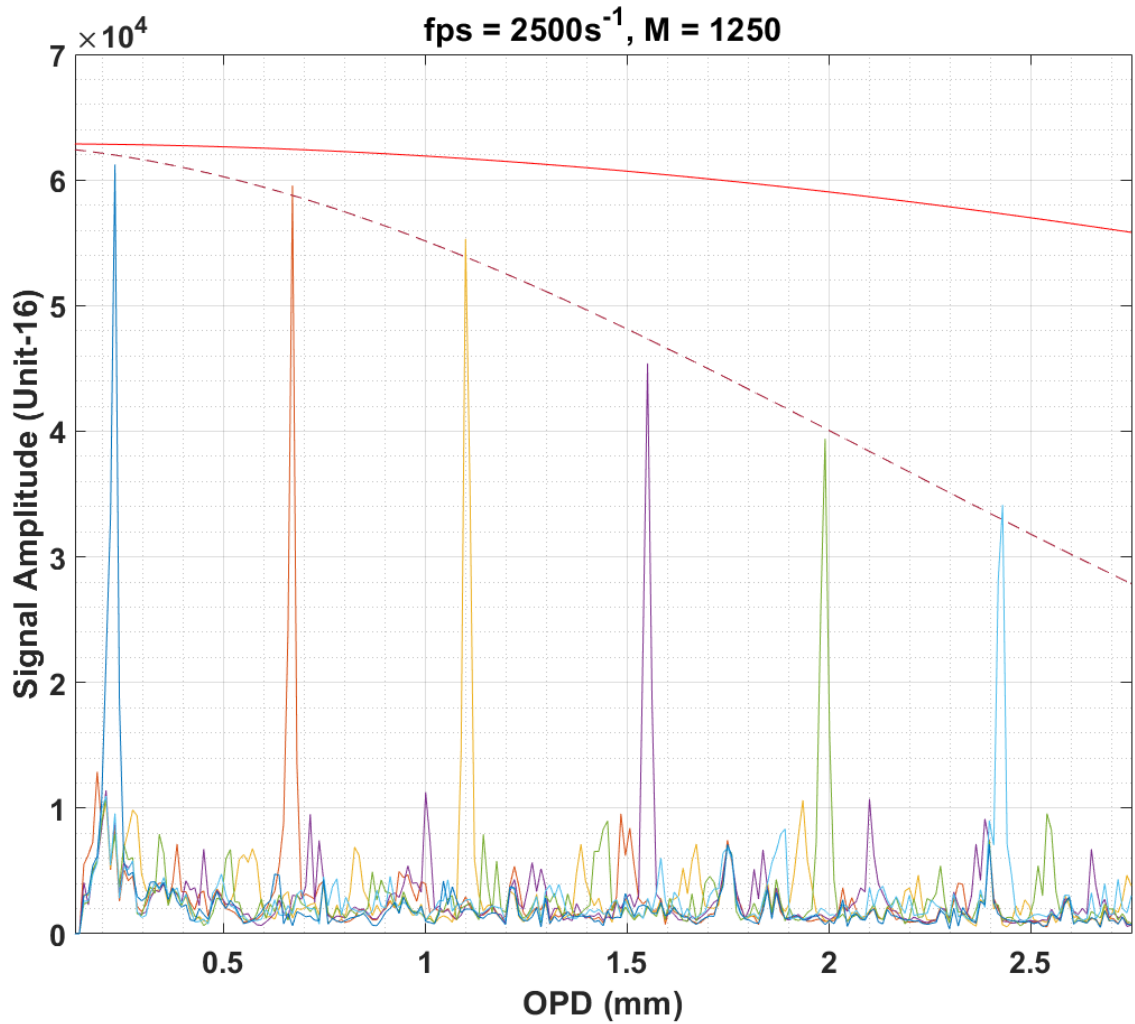


Figure 5.3: Signal amplitude roll off with OPD for  $fps = 2500s^{-1}$ ,  $M = 1250$

The OPD at which the experimental signal amplitude was found to have dropped by half was **OPD = 2.680 mm**, an improvement in depth range from  $fps = 2000 \text{ s}^{-1}$  to  $fps = 2500 \text{ s}^{-1}$  of 3.84 %, which is less than the expected increase of 14.88 %

The sensitivity at  $OPD = 0$  was found to be  $R_{Min} = \frac{1}{SNR_{Max}}$  where  $SNR_{Max} = 28.785 \text{ dB}$ .

### *Discussion*

In both *fps* sets, the most distinguishable Auto-correlation peaks are found at the same OPD positions,  $OPD \approx 1 \text{ mm}$ ,  $OPD \approx 1.5 \text{ mm}$  and at  $1.8 \text{ mm} < OPD < 2 \text{ mm}$ . To give these peaks a physical interpretation we consider the optical elements within object and reference arms.

The peak corresponding to the thinnest optical element,  $OPD \approx 1 \text{ mm}$ , has been interpreted as the interference of both arms passing through the thin glass covering of the CMOS sensor. The peaks within  $1.8 \text{ mm} < OPD < 2 \text{ mm}$  are interpreted to be interference due to the extra OPL introduced into the reference arm by the inclusion of the optical attenuator, which was measured to have a thickness within  $1.8 \text{ mm} < 2 \text{ mm}$ .

### Normalised Depth Profile

The two sets of signal amplitude drop offs were normalised with the maximum signal strength to analyse the drop off in sensitivity of the system versus OPD. A logarithmic ratio of the depth dependent signal amplitude,  $A(OPD)$ , to the signal amplitude at  $OPD = 0$ ,  $A(0)$ , was calculated, and the result plotted as a function of  $OPD$  to obtain a normalised depth profile of the signal amplitude, given in Fig. 5.4.

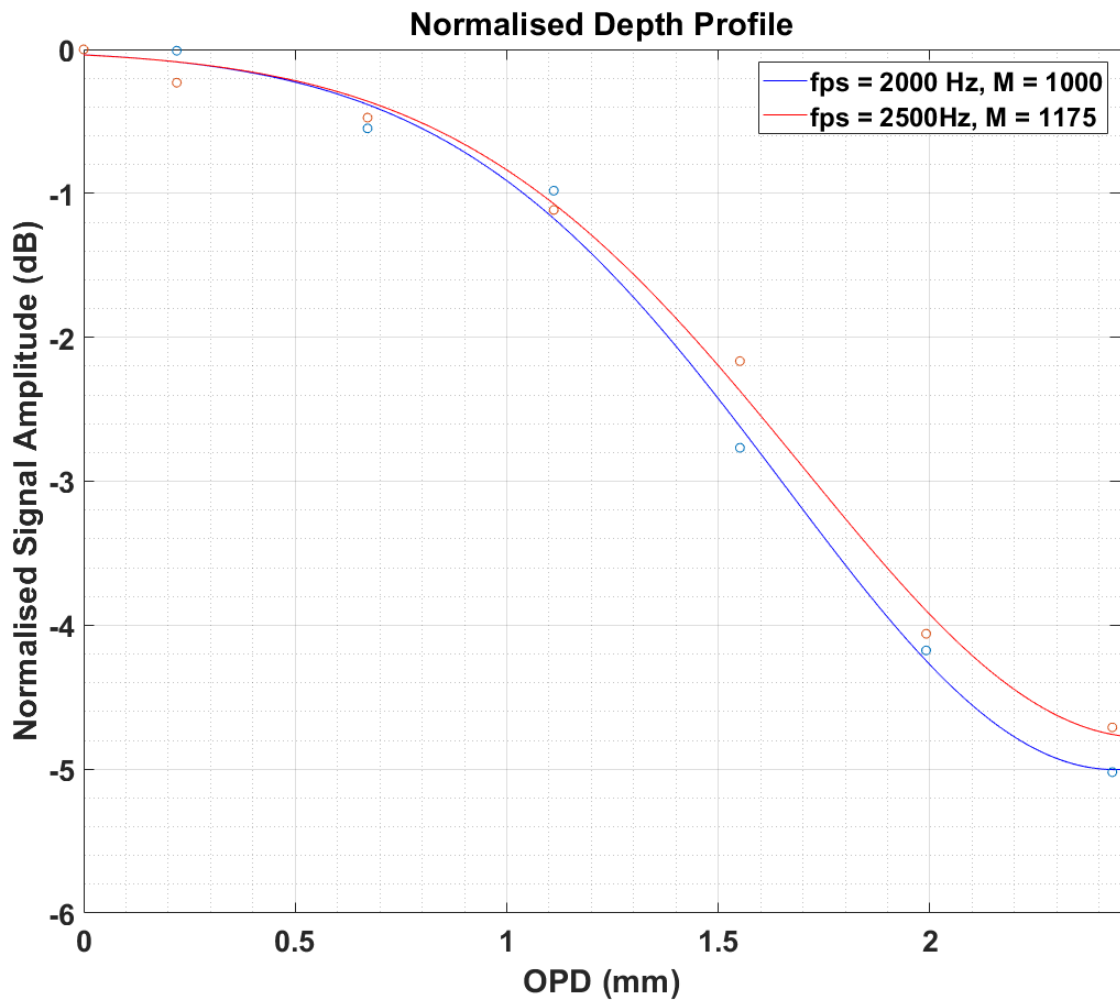


Figure 5.4: Normalised Signal Amplitude versus OPD.

### *SNR Depth Profile*

At each OPD increment another two sets of A-scans were also obtained, which were measured in order to calculate the depth dependent noise. At each OPD increment the object and reference arm beams were in turn blocked, and two separate object and reference A-scans were obtained at each depth. The RMS of the noise amplitude was taken of both object and reference beams, from which a total RMS noise at each depth was calculated, again using all pixels excluding those in the region of the cross correlation and D.C. signals. The SNR was then calculated at each OPD increment and then plotted as a function of OPD, as given in *Fig. 5.5*.

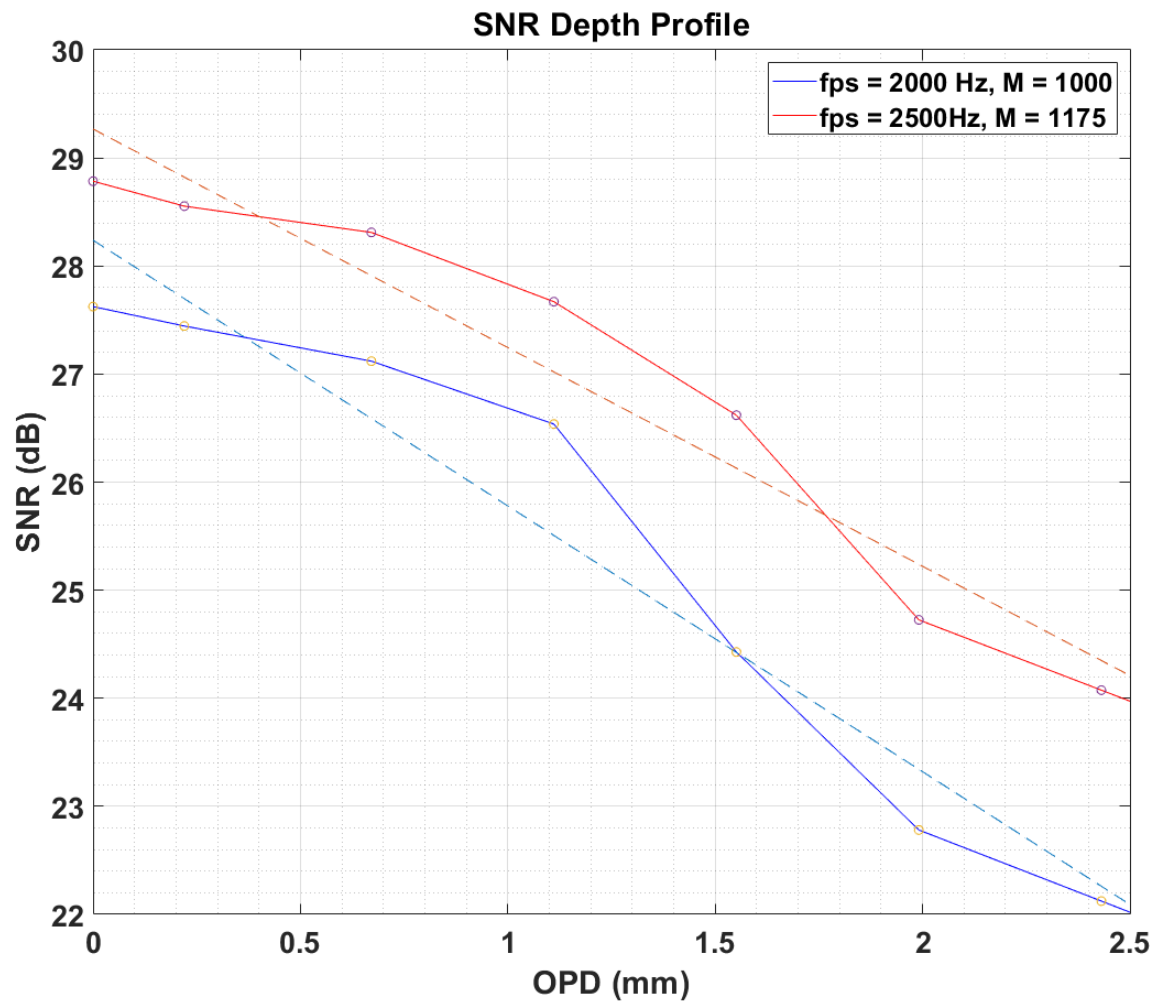


Figure 5.5: SNR versus OPD.

It is seen that both curves follow a similar trend, both having a similar variation of SNR with depth. This suggests that the variations in SNR with OPD are intrinsic to the optics of the system and not dependent on the source and camera sampling parameters of  $M$  and  $fps$ .

### 5.3.2 Sweeping Speed, $\Delta T$

Two sets of experiments were taken to assess the impact of by varying  $\Delta T$  to change  $M$ , one at  $\Delta T = 0.5 s$ ,  $fps = 1600 s^{-1}$ , and one at  $\Delta T = 0.25 s$ ,  $fps = 2000 s^{-1}$ , generating  $M = 800$  and  $M = 500$  respectively. The exposure of each frame was held constant at the maximum permissible value of  $\tau = 0.45 ms$ . The expected depth sensitivity for the two values of  $M$  is given in *Tab. 5.3*.

$M$	$OPD_{-6dB}$
800	3.08 mm
500	1.696 mm

Table 5.3:  $\Delta T$  - Depth sensitivity experiment acquisition parameters.

For each set of  $\Delta T$  the cross-correlation peak was translated in increments of  $OPD = 0.25 mm$ , from  $0.25 mm$  to  $2.75 mm$ , capturing a drop off profile of 11 averaged A-scans. A Gaussian function was fit to each cross-correlation peak to obtain its amplitude. The RMS noise method was repeated to find a value for noise at each OPD increment. The SNR was then calculated at each OPD interval and plotted as a function of OPD to obtain an experimental graph of SNR versus OPD.

An interpolant function is fit to the data points to represent the the experimental drop off profile, while a first order polynomial is fit to the data to represent the linear depth drop of in SNR when plotted on a logarithmic scale in  $dB$  units.

$$\Delta T = 0.25 \text{ s}$$

The experimental graph of SNR versus OPD, measured from the system operating in its bulk version, with  $\Delta T = 0.5 \text{ s}$ , is given in Fig. 5.6.

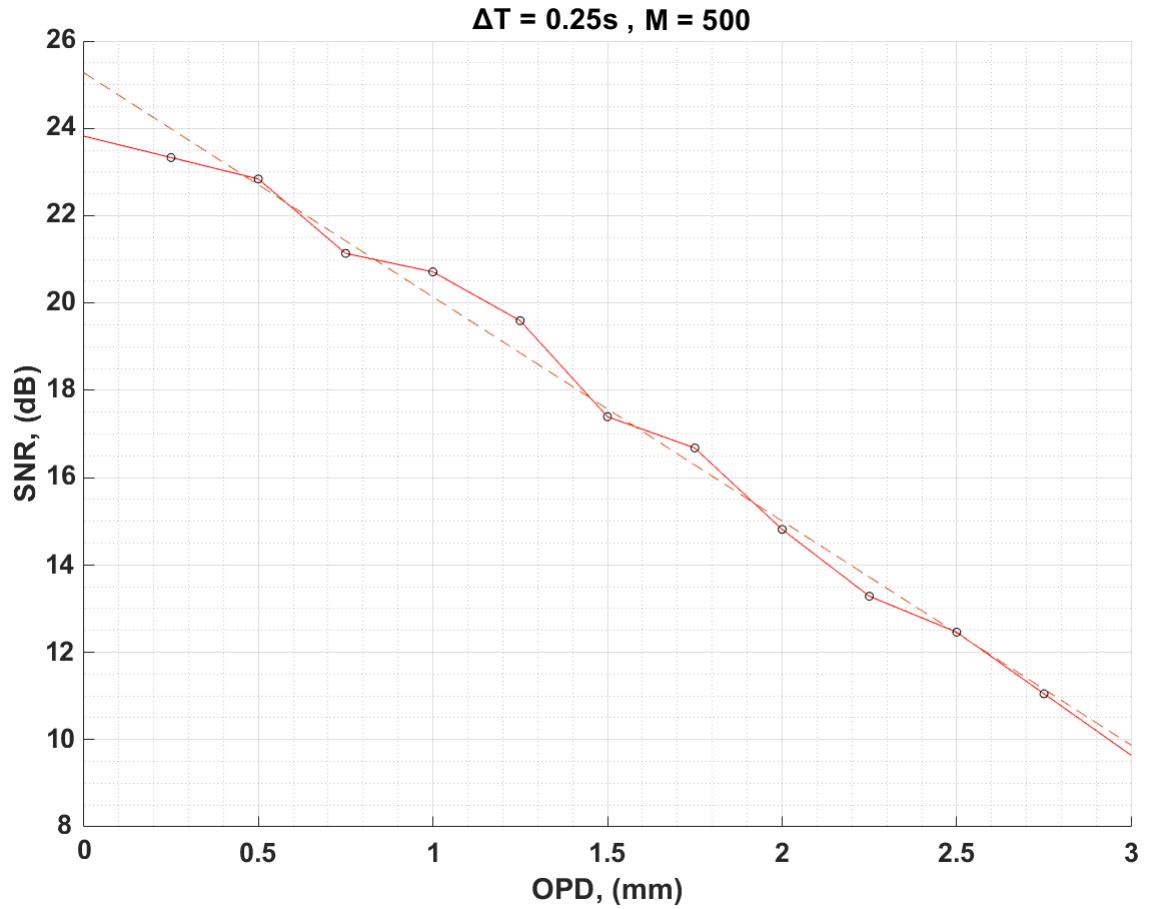


Figure 5.6: SNR versus OPD for  $\Delta T = 0.25 \text{ s}$ ,  $M = 500$ , with interpolant (solid red), and linear (dashed orange) fits.

The experimental -6dB OPD was found to be  $OPD_{-6dB} = 1.47 \text{ mm}$ , which is 13.33 % less than the expected value given in Tab. 5.3.

$$\underline{\Delta T = 0.5 s}$$

The experimental graph of SNR versus OPD, measured from the system operating in its bulk version, with  $\Delta T = 0.5 s$ , is given in Fig. 5.7.

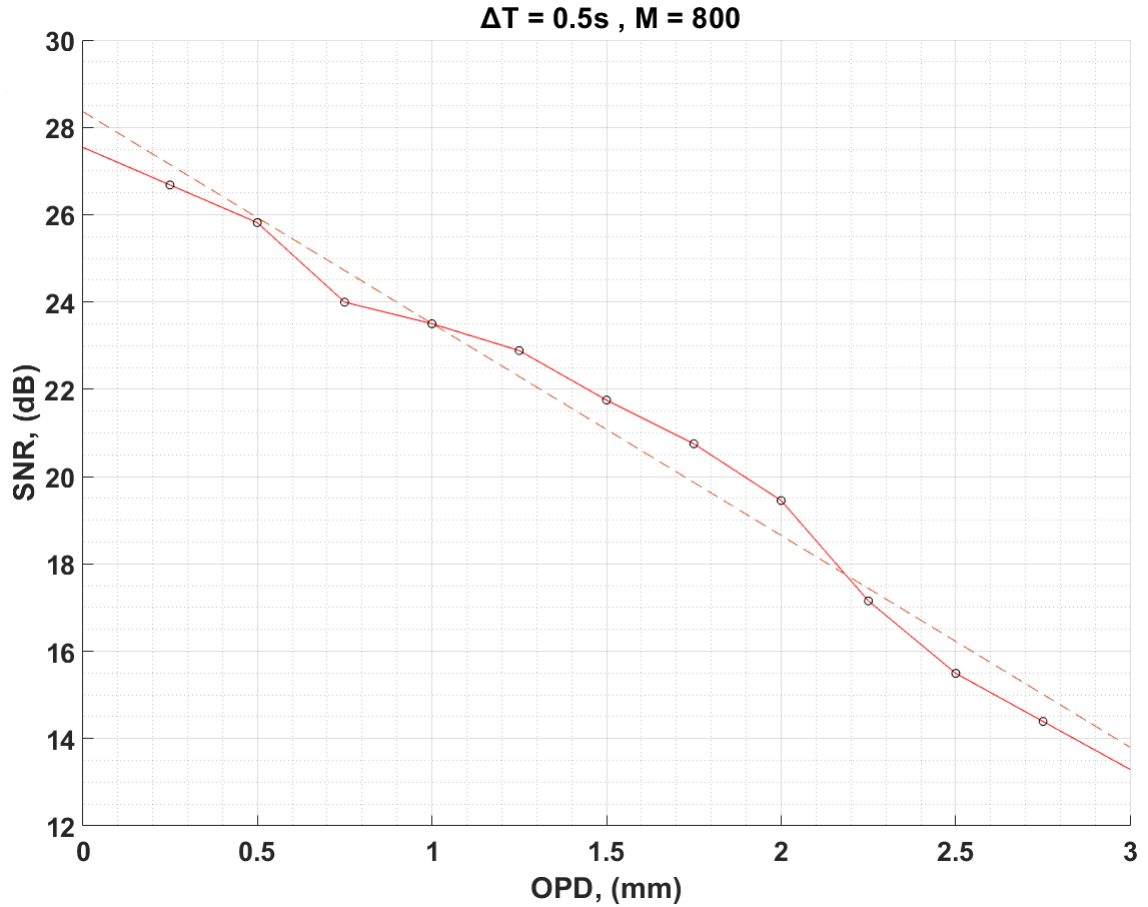


Figure 5.7: SNR versus OPD for  $\Delta T = 0.5s$ ,  $M = 800$ , with interpolant (solid red), and linear (dashed orange) fits.

The experimental -6dB depth OPD was found to be  $OPD_{-6dB} = 1.55 \text{ mm}$ , which was 49.5 % less than the expected value. The improvement in SNR from  $M = 500$  to  $M = 800$  across the axial range is significantly less than expected.



### 5.3.3 Discussion

It is seen that at  $\Delta T = 0.25$  s, the -6dB OPD is approximately equal to the theoretical value. However, as the sampling bandwidth is reduced, there is a diminishing return on the improvement of depth sensitivity. This was also observed in then experiments in which  $\Delta T$  was held constant and  $M$  was raised by increasing *fps*. The results suggest that the sensitivity of the system is better approximated for lower values of  $M$ . That is, a non linear proportionality between  $M$  and SNR is obtained through experimentation, when the theory suggests a linear proportionality, as demonstrated by (2.35).

Increasing  $\Delta T$  is not desirable as this may result in motion artefacts when applied to *in vivo* imaging. Increasing *fps* is therefore more desirable, however increasing *fps* also has its own implications, which are reducing FOV and reducing maximum permissible exposure time,  $\tau$ . We understand that increasing  $\tau$  improves *SNR* and so analysis of SNR as a function of exposure time is also important.

#### 5.3.4 SNR versus $\tau$

The SNR as a function of exposure was captured over a range of exposure times, at two sets of scanning periods,  $\Delta T = 0.5 s$  and  $\Delta T = 1 s$ . A mirror was translated to an OPD of  $1 mm$  and a series of average A-scans were obtained from the central pixel of the FOV. The signal amplitude was obtained by fitting a Gaussian function to the cross correlation peak at  $OPD = 1 mm$ . A single value of noise was obtained by removing the mirror and taking a measurement of the RMS noise at  $OPD = 1 mm$ , taking from a number of spectral points equal to width of the removed cross correlation peak.

The SNR at  $OPD = 1 mm$  was then plotted as a function of  $\tau$ , over the entire range of permissible  $fps$  values. For both sets of sweeping periods,  $M = 800$  spectral points were generated.

$\Delta T$	$fps$	$\tau$
0.5	$1600 s^{-1}$	$0 < 0.625ms$
1	$800 s^{-1}$	$0 < 1.25ms$

Table 5.4:  $\Delta T$  and  $fps$  values and corresponding permissible  $\tau$  ranges.

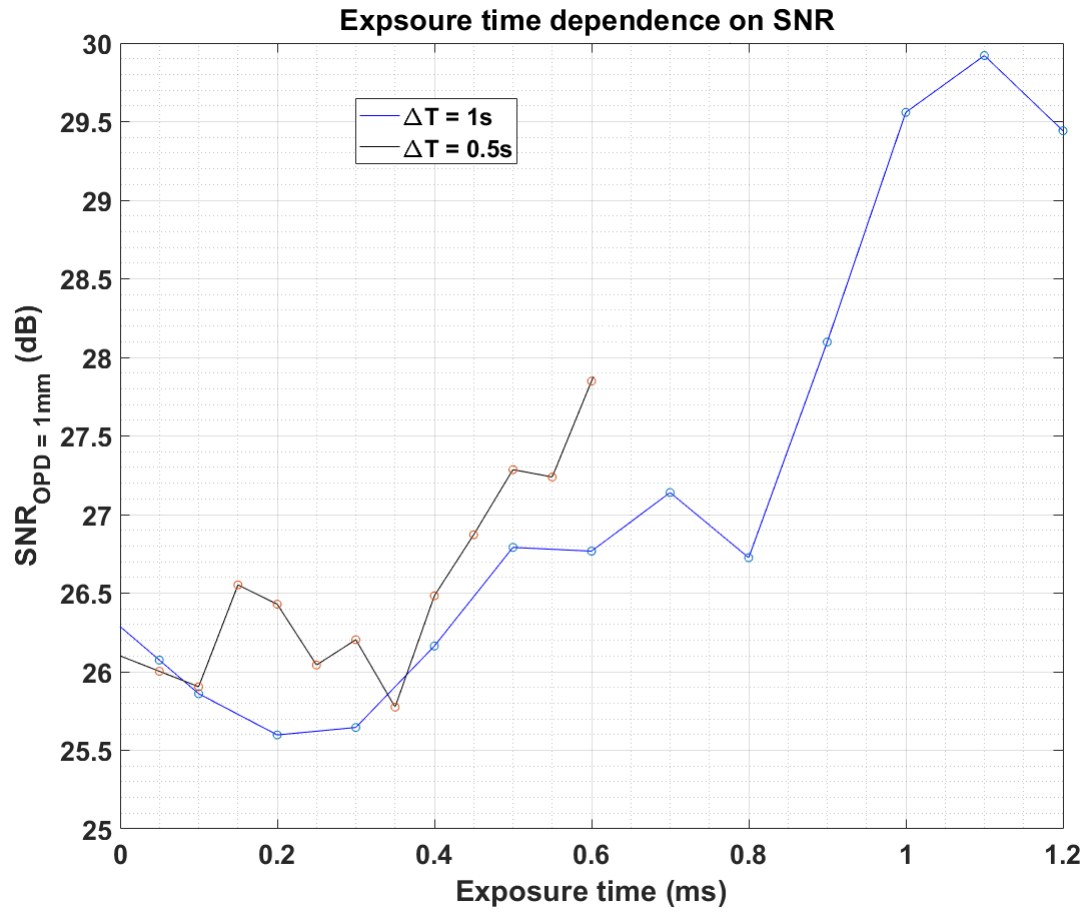


Figure 5.8: SNR as a function of exposure time  $\tau$  at  $OPD = 1mm$ . Obtained with two sweeping periods,  $\Delta T = 0.5s$  and  $\Delta T = 1s$ .

### 5.3.5 Summary

We can conclude from the series of experiments into sensitivity versus OPD that, in general, the expected trends are observed, however the measured performances were less than expected, particularly for higher levels of  $M$ .

The most significant finding is that the predicted improvements of sensitivity versus OPD expected at larger  $M$  have not been experimentally proved. This indicates that the experimental SNR may not perhaps not be proportional to  $M$ , suggesting that the relationship is non linear and that there are diminishing returns in the improvement of sensitivity as  $M$  is increased.

Hence, the optimum parameters of acquisition parameters are not necessarily to maximise  $M$ . Instead, it may be beneficial to slightly reduce  $M$ , therefore enabling for significant improvements in either speed, FOV or both, without sacrificing any significant improvements in sensitivity versus OPD.

## 5.4 5p Coin Images

### 5.4.1 Fixed wavelength

Two images of the lettering of a 5p coin are shown to demonstrate the systems fixed wavelength (FW) imaging capability. Observed in *Fig. 5.9* are the letters 'E' and 'L' of the embossed lettering on the face of a 5p coin.



Figure 5.9: FW image of surface of a 5p coin.

In Fig. 5.10 a fixed wavelength image of the embossed numbers '2' and '0' from the face of a 5p coin is shown.

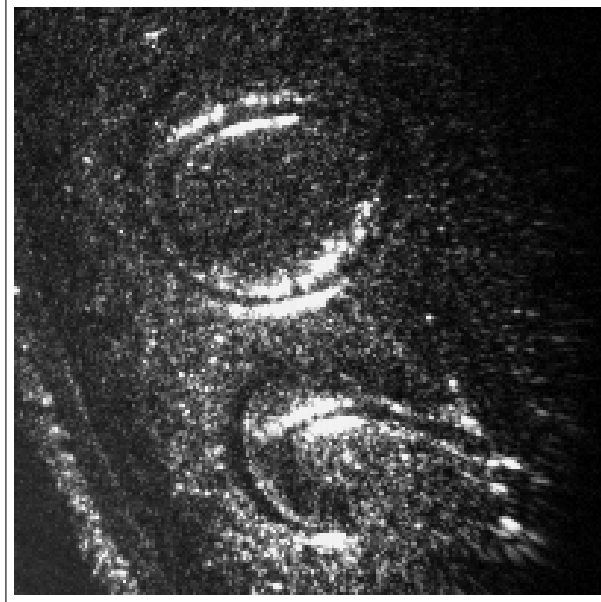


Figure 5.10: Another FW image of surface of 5p coin.

The lateral resolution of the constant wavelength images are inferred from the pixel separation of the CMOS camera, which gives lateral resolutions in the x and y directions of;

$$\Delta x = 14\mu m \quad , \quad \Delta y = 13.6\mu m \quad (5.5)$$

5.4.2 A-scan

Two laterally separated A-scans were taken from the FOV illustrated in Fig. 5.9 , from pixel numbers in x and y co-ordinates of; (100,101) and (109,132), which represented lateral positions that were off to the side of, and on top of the embossed lettering, respectively. The two A-scans are given between the OPD range of 0.55 mm to 0.85 mm in Fig. 5.11.

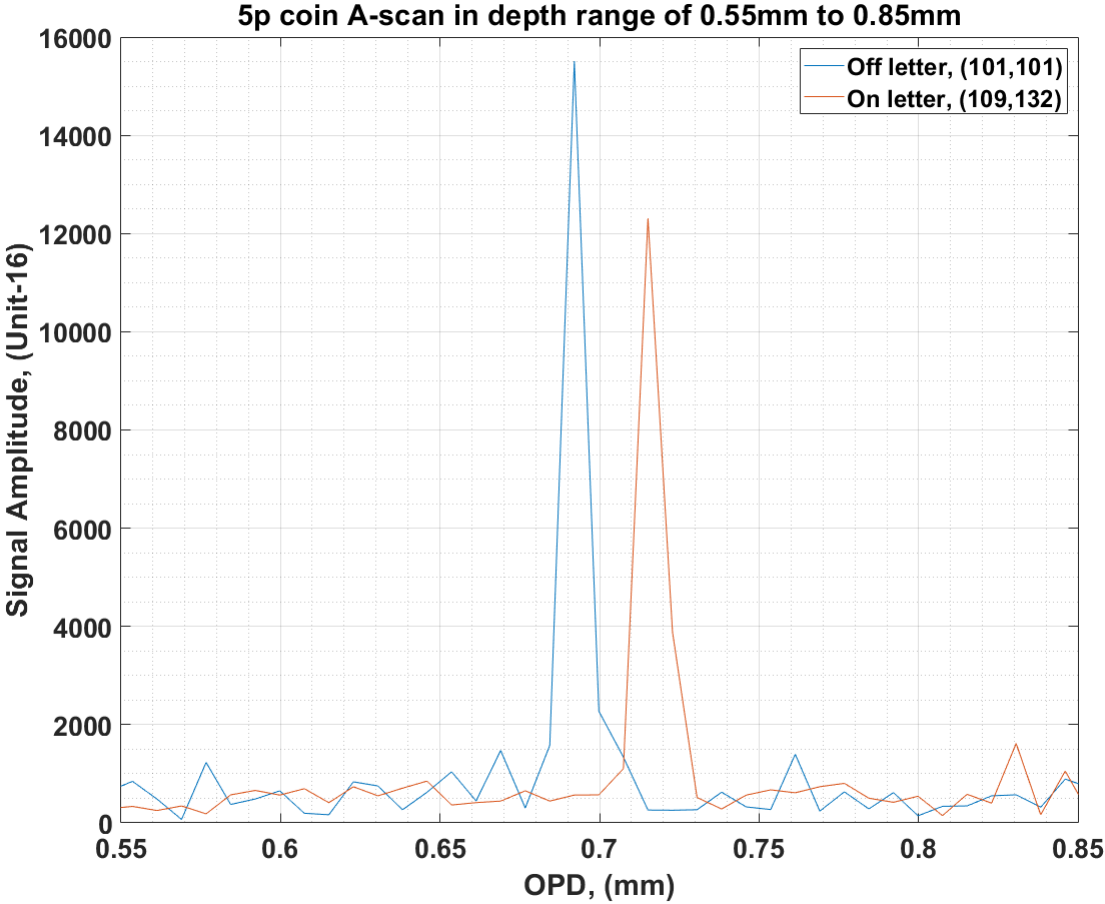


Figure 5.11: A-scans taken from the 5p coin at two different lateral co-ordinates; (100,101) and (109,132).

The axial resolution of the peaks from A-scans (101,101) and (109,132) were found to be  $16.02 \mu m$  and  $16.08 \mu m$  respectively. The axial positions of the two peaks were graphically obtained and their difference calculated to give the thickness of the lettering, which was found to have a thickness of  $z = \mathbf{0.0231 \text{ mm}}$ .



### 5.4.3 B-scan

An example B-scan has been taken from a 5p coin and is shown to demonstrate the acquisition process and image quality. A B-scan ROI is selected in real time by connecting two arbitrary pixels along the lateral plane of the FOV. This is illustrated in *Fig. 5.12*, where the ROI line is given by the green line and the yellow arrow head indicates the lateral orientation of the B-scan.

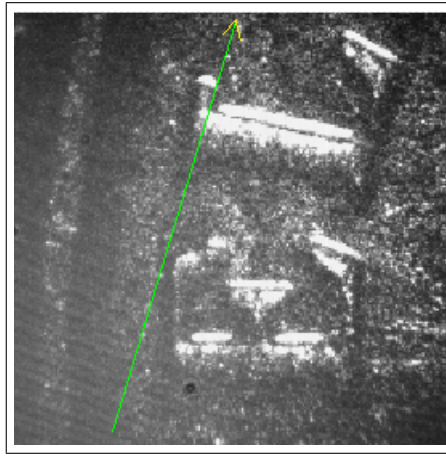


Figure 5.12: Demonstration of the ROI selection for a B-scan.

The B-scan corresponding to *Fig. 5.12* is given in *Fig. 5.13*. A scanning speed of  $\frac{1}{\Delta T} = 1 \text{ Hz}$  and  $f_{ps} = 1000 \text{ s}^{-1}$  were selected, generating  $M = 1000$ . The horizontal axis represents the lateral co-ordinate along the B-scan, and the vertical axis represents the depth in spectral components, where the distance between adjacent spectral points is  $7.69 \mu\text{m}$  and the maximum axial range is  $3.843 \text{ mm}$ . The amplitude of each spectral point is plotted using a scaled colour map, which is on a  $65.36 : 1$  ratio of amplitude to detected Unit-16 pixel intensity.

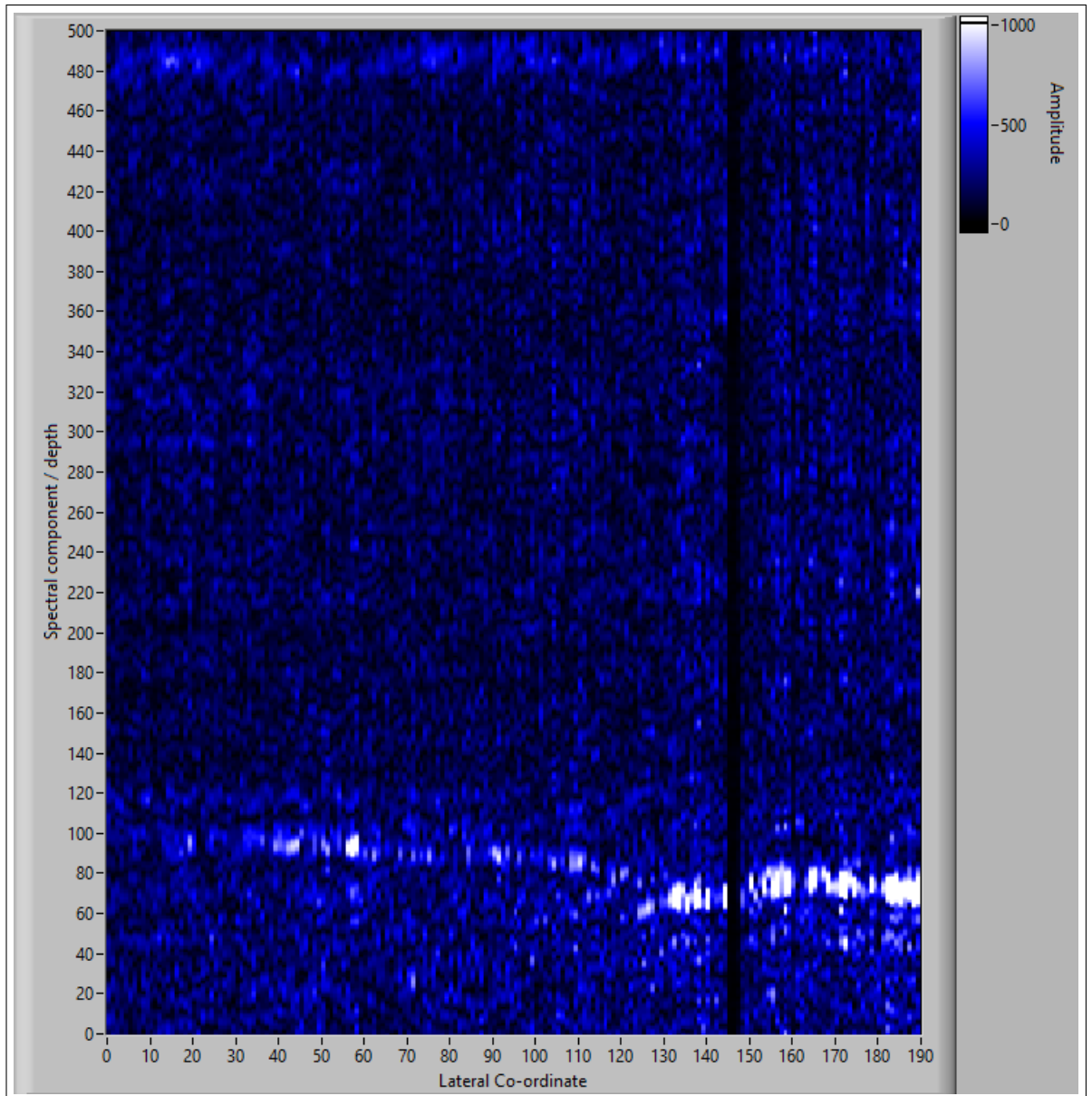


Figure 5.13: B-scan of the ROI from Fig 5.13. Amplitude of each pixel (White-Blue-Black) is plotted as a function of lateral co-ordinate (x-axis) and spectral component/depth (y axis)

The white band observed within the range of the 60th to 120th spectral points represents the embossed lettering of the 5p coin.

Notice that the white band is tilted, with the position in depth reducing as the lateral pixel number is increased. If we look at *Fig. 5.12*, we see that the lateral direction of the B-scan is vertically upwards. Hence, the tilting represents the tilting of the 5p coin, with the upper part of the coin closer to the probe. This was necessary in order for the back reflected light to be collected by the probe.

## CHAPTER 6

# Conclusion and Future Work

### 6.1 Summary

The achievement of the thesis has been the successful design and construction of a compact probe head, which has presented a new design for an off-axis interferometer, and which operates as part of a FF-SS-OCT system.

Working results from the probe were obtained within a bulk version of the system, however, attempts at producing a bundle version were unsuccessful. The particularly large focal length of  $f = 40mm$ , along with the oblique angle between object and reference beams, made it very difficult to inject the interference signal output from the probe head into the CFB. This is different to the bulk version, in which no careful alignment was needed, as the interference signal was simply projected onto the camera sensor, and not injected into fibre.

A sufficient intensity of backscattered light from a reflective object was collected by the probe head for imaging. However, when replaced with a diffuse scattering object, paper, there was no backscattered signal detected. As such it was only possible to acquire A-scans and B-scans from a semi specular 5p coin.

#### *Incorporating a CFB*

Attempts were made to incorporate a CFB into the system, with the intention of enabling the probe head to be made into a remote imaging system. The motivation was to produce a CPH that could potentially be used for applications in endoscopy and in optical biopsy. However, no attempts were successful. At the current lens specifications, the CFB was a distance of  $40\text{ mm}$  from the back of probe, and at such a distance it

was very difficult to inject the light output from the probe into the CFB. The concept of incorporating a CFB into the system has not been disproved, merely has it not been proved.

### *SNR*

The SNR of the system was found to be significantly lower than the potential of FF-SS-OCT, which we concluded to be the result of two causes. The first was probes large ratio of focal length to lens diameter, which meant that  $< 3\%$  of the object backscattered light was captured by the objective lens, resulting in a loss of signal intensity and hence a low SNR.

## 6.2 Future Research and Development

### 6.2.1 CFB Incorporation

The first step of any future research will be to reduce  $f$  whilst maintaining the same  $A_l$ . This will increase SNR, and is hence the most obvious and immediate step towards incorporating a CFB. The first achievement would be to achieve sufficient sensitivity such that a detectable signal could be obtained from a mirror. With improvements in sensitivity the mirror can be replaced with a scattering object. It would be favourable to employ a MS processing method for the improved axial resolution throughout the depth range.

The next development would be to explore FF-OCT aspects of the system, such as the lateral resolution of spectral frames. Methods of improvement could then be developed, such as removing pixelation effects using novel processing methods, [42, 43].

### 6.2.2 Miniaturization

The next development upon successfully obtaining volumes through the CFB would be to reduce  $A_l$ , hence miniaturizing the probe head. The eventual goal would be to reduce  $A_l$  until the diameter of the probe head would equal the diameter of the CFB. There are several consequences of miniaturization that must be considered, of which we consider the FOV.

## FOV

Miniaturization will reduce FOV, a consequence of smaller  $f$  reducing the area covered by the divergent object and reference beams. Hence, the divergence of the launching fibres must be increased. One approach would be to modify the end of the fibres into a ball shape, which would change the direction of the refracted beam, increasing its cross sectional area at a given distance from the fibre. The modified ball end could potentially be crafted using an advanced Fusion splicer. An illustration of the divergence of light from a conventional flat faced fibre end and a modified ball shaped end fibre are shown in *Fig. 6.1*.

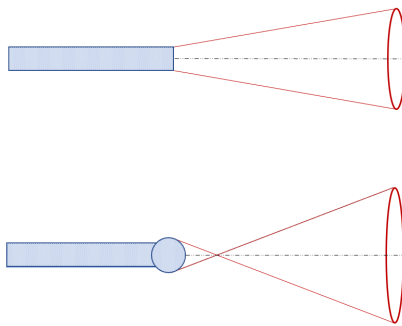


Figure 6.1: Illustration of the divergence from a conventional flat faced fibre (top) and ball end shaped fibre (bottom)

### 6.2.3 D.C. removal by off-axis incidence of reference arm

An exciting possibility for future work is to explore the possibility of using the interference pattern induced by the off-axis incidence of the reference and object arms as a means of artificially removing the D.C. signal.

#### *Analysis*

The affect of the induced interference pattern can be predicted by applying models from off-axis holography, in which two planar wavefronts, object and reference beams with electric fields  $E_O$  and  $E_R$  respectively, are taken from the same source and superimposed onto a detector at an oblique angle of incidence. This is achieved by tilting the reference beam relative to the on-axis object beam, i.e. tilting the reference beam relative to the axial direction. Similarly to OCT, the detected photo-current is dependent on the irradiance of the superimposed beam;

$$I = |E_O|^2 + |E_R|^2 + E_O^* E_R + E_O E_R^* \quad (6.1)$$

The reference beam is given by (6.2), where  $E_o$  is its electric field amplitude,  $\vec{k}$  is its wavevector, and  $\vec{r}$  is its position vector.

$$E_R = E_o e^{i(\vec{k} \cdot \vec{r})}, \quad (6.2)$$

which we can decompose into the directions parallel,  $\vec{k}_{\parallel}$ , and perpendicular,  $\vec{k}_{\perp}$ , to the area of the Full-field detector to obtain (6.3).

$$E_R = E_o [exp(i\vec{k}_{\parallel} \cdot \vec{r}) \cdot exp(i\vec{k}_{\perp} \cdot \vec{r})] \quad (6.3)$$

If we take the FT of the detected photocurrent, (6.1), along the lateral plane of the



detector in  $xy$  coordinates, we obtain, [44],

$$\mathcal{F}_{xy}^{-1}\left[E_O^*E_R + E_OE_R^*\right] = \mathcal{F}_{xy}^{-1}[E_R] \otimes \mathcal{F}_{xy}^{-1}[E_O^*] + \mathcal{F}_{xy}^{-1}[E_R^*] \otimes \mathcal{F}_{xy}^{-1}[E_O] \quad (6.4)$$

Where, [44],

$$\begin{aligned} \mathcal{F}_{xy}[E_R] &= E_o\delta(\vec{k}_{xy} - \vec{k}_{\parallel}) \\ \mathcal{F}_{xy}[E_R^*] &= E_o^*\delta(\vec{k}_{xy} + \vec{k}_{\parallel}) \end{aligned} \quad (6.5)$$

Is is seen then that the resulting Dirac delta function peaks in the real space are translated in position by a distance given by  $\vec{k}_{\parallel}$ , which from *Fig. 4.12* is given by  $\vec{k}_{\parallel} = |\vec{k}|\sin(\theta)$ .

The theory suggests that for larger enough  $\theta$ , the OCT cross-correlation signal could be shifted laterally clear from the D.C. signal. The off-axis incidence of the reference arm hence presents the possibility of effectively removing the D.C. component from the image, therefore potentially enabling components of the image from within the vicinity of the surface of the object to be obtained, which would otherwise be hidden behind the D.C. signal.

### 6.2.4 Mirror Terms

A final aspect that should be considered as part of future work is the phenomenon of mirror terms. Considering that the instantaneous coherence function is mirrored about  $OPD = 0$ , we obtain an OCT image both sides of  $OPD = 0$ , and hence, if  $OPD = 0$  is displaced into the object then we will obtain a superposition of images, from the two sides of  $OPD_0$ .

Throughout all of the experiments conducted in the thesis,  $OPD_0$  was always positioned at the surface of the object under investigation. However, if  $OPD_0$  were positioned inside the object then mirror terms would be produced, corrupting the image. One possible method of removing mirror terms is by using Talbot bands, [45]. An illustration of mirror terms is given in Fig. 6.2.

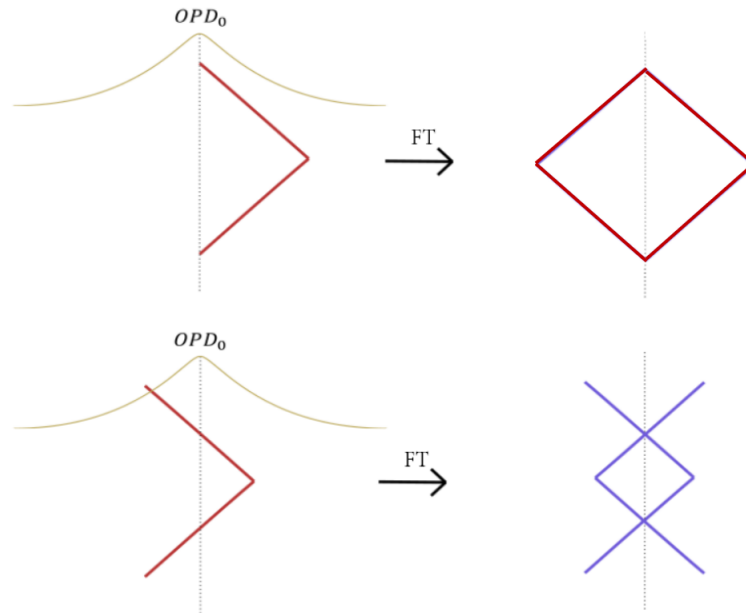


Figure 6.2: Illustration of mirror terms. Top: No overlap of object through  $OPD_0$ , therefore no mirror terms in FT. Bottom: Overlap of object through  $OPD_0$ , therefore mirror terms in FT

## References

- [1] L. F. L. D., “Novel perspectives on swept-source optical coherence tomography,” *International journal of retina and vitreous*, vol. 25, 2016.
- [2] H. D. Ford and R. P. Tatam, “Coherent fibre bundles in full-field swept-source oct,” *Proc. SPIE BIOS*, vol. 7168, 2009.
- [3] H. Ford and R. Tatam, “Passive oct probe head for 3d duct inspection,” *Measurement Science and Technology*, vol. 24, p. 094 001, Jul. 2013.
- [4] H. D. Ford and R. P. Tatam, “Full-field optical coherence tomography using a fibre imaging bundle,” *Proc. SPIE 6079*, vol. 6079, 2006.
- [5] F. Helen and T. Ralph, “Fibre imaging bundles for full-field optical coherence tomography,” *Measurement Science and Technology*, vol. 185730, pp. 2949–295 781, Sep. 2007.
- [6] H. D. Ford and R. P. Tatam, “Swept-source oct with coherent imaging fibre bundles,” *Proc. SPIE*, vol. 7503, 2009.
- [7] H. Liang, B. Peric, M. Hughes, A. Podoleanu, M. Spring, and D. Saunders, “Optical coherence tomography for art conservation and archaeology,” vol. 6618, 2007.
- [8] J. G. Fujimoto and W. Drexler, *Optical Coherence Tomography - Technology and Applications*. Springer International Publishing, 2015.
- [9] A. Agrawal, T. J. Pfefer, P. D. Woolliams, P. H. Tomlins, and G. Nehmetallah, “Methods to assess sensitivity of optical coherence tomography systems,” *Biomed. Opt. Express*, vol. 8, no. 2, pp. 902–917,
- [10] A. G. Podoleanu, “Optical coherence tomography,” *Journal of Microscopy*, June 2012.
- [11] B. Golubovic, B. E. Bouma, G. J. Tearney, and J. G. Fujimoto, “Optical frequency-domain reflectometry using rapid wavelength tuning of a cr<sup>4+</sup>:forsterite laser,” *Opt. Lett.*, vol. 22, no. 222, pp. 1704–1706, 1997.
- [12] S. R. Chinn, E. A. Swanson, and J. G. Fujimoto, “Optical coherence tomography using a frequency-tunable optical source,” *Opt. Lett.*, vol. 22, no. 5, pp. 340–342, 1997.

- [13] L. Bei, G. I. Dennis, H. M. Miller, T. W. Spaine, and J. Carnahan, “Acousto-optic tunable filters: Fundamentals and applications as applied to chemical analysis techniques,” *Progress in Quantum Electronics*, vol. 28, pp. 67–87, Dec. 2004.
- [14] T. J. Fellers and M. W. Davidson, “Acousto-optic tunable filters,” *Olympus*, Aug. 2004.
- [15] C. Sobrinho, J. Lima, E. de Almeida, and A. Sombra, “Acousto-optic tunable filter (aotf) with increasing non-linearity and loss,” *Optics Communications*, vol. 208, no. 4, pp. 415–426, 2002.
- [16] M. E. Brezinski, *Optical Coherence Tomography-Principles and Application*. Academic Press - Elsevier, 2006.
- [17] S. V. der Jeught, A. Bradu, and A. G. Podoleanu, “Real-time resampling in fourier domain optical coherence tomography using a graphics processing unit,” *Journal of Biomedical Optics*, vol. 15, no. 3, pp. 1–3, 2010.
- [18] A. G. Podoleanu and A. Bradu, “Master–slave interferometry for parallel spectral domain interferometry sensing and versatile 3d optical coherence tomography,” *Opt. Express*, vol. 21, no. 16, pp. 19 324–19 338, 2013.
- [19] J. Wang, A. Bradu, G. Dobre, and A. Podoleanu, “Full-field swept source master-slave optical coherence tomography,” vol. 7, no. 4,
- [20] T. Mitsui, “Dynamic range of optical reflectometry with spectral interferometry,” *Japanese Journal of Applied Physics*, vol. 38, pp. 6133–6137, Oct. 1999.
- [21] M. A. Choma, M. V. Sarunic, C. Yang, and J. A. Izatt, “Sensitivity advantage of swept source and fourier domain optical coherence tomography,” *Opt. Express*, vol. 11, no. 18, pp. 2183–2189, 2003.
- [22] Superlum, *BroadSweeper-840 (BS0002) - Instruction Manual*. 2007.
- [23] B. Buchroithner, G. Hanneschläger, E. Leiss-Holzinger, A. Prylepa, and B. Heise, “Full-field optical coherence tomography and applications,” vol. 10591, 2018.
- [24] P. Stremplewski, E. Auksorius, P. Wnuk, Ł. Kozoń, P. Garstecki, and M. Wojtkowski, “Speckle-free and cross-talk-free imaging in fourier domain full-field optical coherence tomography,” in *Biophotonics Congress: Optics in the Life Sciences Congress 2019*, Optical Society of America, 2019.
- [25] S. J. Medical, “Optis integrated system,”

- [26] X. Liu, M. J. Cobb, Y. Chen, M. B. Kimmey, and X. Li, "Rapid-scanning forward-imaging miniature endoscope for real-time optical coherence tomography," *Opt. Lett.*, vol. 29, no. 152, pp. 1763–1765, 2004.
- [27] G. J. Tearney, M. E. Brezinski, B. Bouma, S. Boppart, C. Pitris, J. F. Southern, and J. G. Fujimoto, "In vivo endoscopic optical biopsy with optical coherence tomography," *Science*, vol. 276, no. 5321, pp. 2037–9, 1997.
- [28] H. Park, C. Song, M. Kang, Y. Jeong, and K. Jeong, "Forward imaging oct endoscopic catheter based on mems lens scanning," *Opt. Lett.*, vol. 37, no. 13, pp. 2673–5, 2012.
- [29] T. Xie, D. Mukai, S. Guo, M. Brenner, and Z. Chen, "Fiber-optic-bundle-based optical coherence tomography," *Opt. Lett.*, vol. 30, no. 14, pp. 1803–5, 2005.
- [30] Schott, "Leached image bundles," [https://www.schott.com/d/lightingimaging/5351f8c1-0881-48ac-94a4-0e1a71dcdd0/1.3/lfb\\_datasheet\\_usa\\_pril2015.pdf](https://www.schott.com/d/lightingimaging/5351f8c1-0881-48ac-94a4-0e1a71dcdd0/1.3/lfb_datasheet_usa_pril2015.pdf),
- [31] G. F. Sarantavgas, H. D. Ford, and R. P. Tatam, "Imaging fibre bundles for fizeau-based optical coherence tomography," *Proc. of SPIE*, vol. 6847, 2008.
- [32] H. D. Ford and R. P. Tatam, "Fibre imaging bundles for full-field optical coherence tomography," *Measurement Science and Technology*, vol. 18, no. 9,
- [33] K. L. Reichenbach and C. Xu, "Numerical analysis of light propagation in image fibers or coherent fiber bundles," *Opt. Express.*, vol. 15, pp. 2151–2165, 2007.
- [34] H. D. Ford and R. P. Tatam, "Numerical analysis of light propagation in image fibers or coherent fiber bundles," *Applied Optics*, vol. 50, no. 5, pp. 627–640, 2011.
- [35] X Zhoua, J Wang, K Selvon, M Matela, G. Dobre, and A. G. Podoleanu, "Effects of fiber bundle on the performance of full-field swept source oct," *Proc. of SPIE*, vol. 8914, 2013.
- [36] H. D. Ford and R. P. Tatam, "Passive oct probe head for 3d duct inspection," *Meas. Sci. Technol.*, vol. 24, 2013.
- [37] M. S. Pochechuev, I. V. Fedotov, and A. M. Zheltikov, "An ultraslim all-fiber microendoscope for depth-resolved imaging," *Applied Physics Letters*, vol. 113, 2018.
- [38] L. M. Wurster, A. Kumar, D. J. Fechtig, L. Ginner, and R. A. Leitgeb, "Lensless holographic endoscopy with a fiber bundle," *Biomedical Optics*, 2016.

- [39] “Edmund optics. 6.25mm x 40mm vis-nir coated achromatic lens. stock 49-310,” <https://www.edmundoptics.com/p/625mm-dia-x-40mm-fl-vis-nir-coated-achromatic-lens/9665/>,
- [40] “Thorlabs. sm800,” [https://www.thorlabs.com/Images/PDF/Vol18\\_64.pdf](https://www.thorlabs.com/Images/PDF/Vol18_64.pdf),
- [41] Mikrotron, “Eosens cl camera manuel, model: Mc1360-63,” p 42, 2012.
- [42] J.-H. Han and S. M. Yoon, “Depixelation of coherent fiber bundle endoscopy based on learning patterns of image prior,” *Opt. Lett.*, vol. 36, no. 16, pp. 3212–3214, 2011.
- [43] J.-H. Han, J. Lee, and J. U. Kang, “Pixelation effect removal from fiber bundle probe based optical coherence tomography imaging,” *Opt. Express*, vol. 18, no. 7, pp. 7427–7439, 2010.
- [44] D. Hillmann, H. Spahr, H. Sudkamp, C. Hain, L. Hinkel, G. Franke, and G. Huttmann, “Off-axis reference beam for full-field swept-source oct and holoscopy,” *Opt. Express*, vol. 25, no. 22, pp. 2183–2189, 2017.
- [45] A. Bradu and A. G. Podoleanu, “Attenuation of mirror image and enhancement of the signal-to-noise ratio in a talbot bands optical coherence tomography system,” *Journal of Biomedical Optics*, vol. 16, no. 7, pp. 1 –11, 2011.